Multi-Instrument Magnetospheric Substorm Studies

A Thesis
Submitted for the Degree of
Doctor of Philosophy

In the
Department of Physics and Astronomy
The University of Leicester
Leicester, UK

By
Natalie Caroline Draper
October 2005

UMI Number: U206524

UMI

Dissertation Publishing

UMI U206524

ProQuest

Contents

Abstract

Multi-Instrument Magnetospheric Substorm Studies

Natalie Caroline Draper

The work presented in this thesis is intended to improve our understanding of the magnetospheric substorm process and in particular the substorm onset mechanism. Studying the timing of known substorm expansion phase onset signatures from a variety of instruments collecting data in key regions of the magnetosphere, ionosphere and on the ground allowed comparison of the events chosen to substorm onset models. Two substorm case studies are presented for intervals during which complementary data sets were available. The principal data sets came from the Fluxgate magnetometer (FGM), Plasma Electron and Current Experiment (PEACE), Cluster Ion Experiment (CIS) and Research with Adaptive Particle Imaging Detectors (RAPID) instruments on the Cluster spacecraft. It was only possible to determine the onset mechanism for one of the three substorms studied (the near-Earth neutral line model). Rapid thinning of the current sheet was detected prior to the third substorm studied. A tailward-moving travelling compression region was then detected in the magnetotail at substorm onset, and the near-Earth neutral line was located at 15 R_E downtail. At onset the Region 1 current system was skewed to the pre-midnight sector, later returning to a more central location about the midnight sector. A new feature has been identified in the magnetotail and termed a magnetic cavity. This was not a singular feature; ten magnetic cavities were identified and four studied in detail. They are features located in the plasma sheet boundary layer and plasma sheet which have close to zero magnetic field and plasma characteristics similar to that of the central plasma sheet. There is evidence that magnetic cavities may be associated with the recovery phase of magnetospheric substorms.

Declarations

During the course of work undertaken for this thesis, the following first author scientific papers have been published:

Draper, N.C., Lester, M., Wild, J.A., Milan, S.E., Provan, G., Grocott, A., Cowley, S.W.H., Bogdanova, Y., Dewhurst, J.P., Fazakerley, A.N., Davies, J.A., Bosqued, J.M., A joint Cluster and ground-based instruments study of two magnetospheric substorm events on 1st September 2002 *Ann. Geophys.*, 22, 4217 - 4228, 2004

Draper, N.C., M. Lester, J.A. Wild, S.E. Milan, G. Provan, A. Grocott, S.W.H. Cowley, A.N. Fazakerly, A. Lahiff, J.A. Davies, J.-M. Bosqued, J.P. Dewhurst, R. Nakamura, C.J. Owen, Simultaneous SuperDARN and Cluster observations of the growth and expansion phases of substorms, *Proc. Seventh Internat. Conf. on Substorms*, UDK-52-854, FMI, Helsinki, Finland, 103-106, 2004

Draper, N.C., Lester, M., Cowley, S.W.H., Bosqued, J.M., Grocott, A., Wild, J.A., Bogdanova, Y., Fazakerley, A.N., Davies J.A., Cluster observations of a magnetic field cavity in the plasma sheet, *Adv. Space Res.*, Accepted 15 September 2005

Draper, N.C., Lester, M., Cowley, S.W.H., Wild, J.A., Milan, S.E., Provan, G., Grocott, A., Fazakerley, A.N., Lahiff, A., Davies, J.A., Bosqued, J.M., Dewhurst, J.P., Nakamura, R., Owen, C.J., Watermann, J., Henderson, M.G., Singer, H.J., Donovan, E., Cluster magnetotail observations of a tailward-travelling plasmoid at substorm expansion phase

onset and field aligned currents in the plasma sheet boundary layer, *Ann. Geophys.*, Accepted 15 November 2005

The following scientific papers have also been published:

Milan, S.E., Wild, J.A. Grocott, A., and Draper, N.C., Space- and ground-based investigations of solar wind-magnetosphere-ionosphere coupling, *Adv. Space Res.*, Accepted September 2004

Nakamura, R., Amm, O., Laakso, H., Draper, N., Lester, M., Grocott, A., Klecker, B., Balogh, A., Rème, H., and André, M., Localized fast flow disturbance observed in the plasma sheet and in the ionosphere, *Ann. Geophys.*, 23, 553-566, 2005

Acknowledgements

Chapter 1

Introduction

1.1 Plasma

Plasma is the fourth state of matter, consisting of ionized gases. It is the most common state of matter in the universe. Cold plasmas are those in which only a small fraction of the gas is ionised; the electron temperature might be several thousand degrees but the ion temperature would be closer to that of the surroundings. Hot plasmas are nearly fully ionised and the ions and electrons are more likely to have equal temperatures, although due to the large mass of the ions relative to the electrons the temperature of the two can still differ significantly. The plasma in the Sun is hot plasma. Plasma beta is used to give a measure of the temperature of the plasma. It is the ratio of the plasma pressure ($nk\mathbf{T}_\perp$) to the magnetic pressure ($\mathbf{B}^2/2\mu_0$):

$$\beta = 2\mu_0 nk\mathbf{T}_\perp/\mathbf{B}^2 \qquad (1.1)$$

where μ_0 is the permeability of a vacuum ($4\pi \times 10^{-7}$ Vs/Am), n is the number of particles (cm^{-3}), k is Boltzmann's constant (1.38×10^{-23} J/K), $\mathbf{T}_\perp$ is the perpendicular component of the temperature (Kelvin), and $\mathbf{B}$ is the magnetic flux density (Tesla). When $\beta > 1$ the plasma pressure dominates over the magnetic pressure

The charged particles of plasma are affected by electric and magnetic fields. The interactions with magnetic fields, such as that of the Sun and Earth, can cause extremely

1

complex behaviour. This behaviour can be described using Maxwell's equations. In 1864 James Clerk Maxwell developed a set of equations expressing the basic laws of electricity and magnetism. The first of these expresses how electric charges produce electric fields (Gauss' law):

$$\nabla \cdot (\varepsilon \mathbf{E}) = \rho \qquad (1.2)$$

The second expresses the experimental absence of magnetic charges:

$$\nabla \cdot \mathbf{B} = 0 \qquad (1.3)$$

The third expresses how currents produce magnetic fields (Ampère's law):

$$\nabla \times (\mathbf{B}/\mu) = \mathbf{J} + \varepsilon \, \partial \mathbf{E}/\partial t \qquad (1.4)$$

The fourth expresses how changing magnetic fields produce electric fields (Faraday's law of induction):

$$\nabla \times \mathbf{E} = -\partial \mathbf{B}/\partial t \qquad (1.5)$$

where $\mathbf{B}$ is the magnetic flux density (Tesla), $\mathbf{J}$ is the current density (Amperes per square metre), $\mathbf{E}$ is the electric field (Volts per metre), t is time, ρ is the free electric charge density (Coulombs per cubic metre), μ is the permeability of the material (Henrys per metre) and ε is the permittivity of the material (Farads per metre).

Using Faraday's law, Ampère's law and Ohm's law in combination yield the following:

$$\partial \mathbf{B}/\partial t = -(\nabla \times E)$$

$$= -\nabla \times (\mathbf{J}/\sigma - \mathbf{v} \times \mathbf{B})$$

$$= \nabla \times (\mathbf{v} \times \mathbf{B}) + \nabla^2 \mathbf{B}/\mu_0 \sigma \qquad (1.6)$$

where σ is the conductivity and $\mathbf{v}$ is plasma velocity. The first term of equation 1.6 is the convective term and the second is the diffusive term. The ratio of the two terms yields the magnetic Reynolds number:

$$R_m = (\nabla \times (\mathbf{v} \times \mathbf{B}))/ (\nabla^2 \mathbf{B}/\mu_0\sigma) \sim \mu_0\sigma V_0 L_0 \qquad (1.7)$$

Where V_0 is the characteristic velocity of the plasma and L_0 is its characteristic scale length. When R_m is large, diffusion is negligible but when R_m is small (due to small values of V_0 or L_0), the plasma is diffusive. For the plasma of the solar wind R_m is large since collisions are negligible, so the solar wind can be approximated to an infinitely conducting plasma with no diffusive term in Equation 1.6. This leads to the equation:

$$\mathbf{E} = -\mathbf{v} \times \mathbf{B} \qquad (1.8)$$

This is the frozen-in approximation, which in the first instance implies that the magnetic fields of different plasma regimes cannot mix. However on small scales, when two non-parallel magnetic fields come together, the frozen in condition can break down.

Magnetic reconnection occurs when the plasmas associated with separate, non-parallel magnetic field lines come into close contact (Figure 1.1a: blue lines depicting one set of magnetic field lines and red magnetic field lines depicting another), forming a diffusion region in which the frozen in condition (Equation 1.8) does not hold. The two magnetic field lines closest to each other can be approximated to an 'x-line' (dashed black lines in Figure 1.1b); that is, they come together, join at the centre, then break perpendicular to their joining such that the two magnetic field lines formed are perpendicular to those from which they are formed (blue and red lines in Figure 1.1c). As they are highly bent, their magnetic tension is high and they are accelerated away from the reconnection point, allowing other magnetic field lines to take their place and the reconnection process to continue.
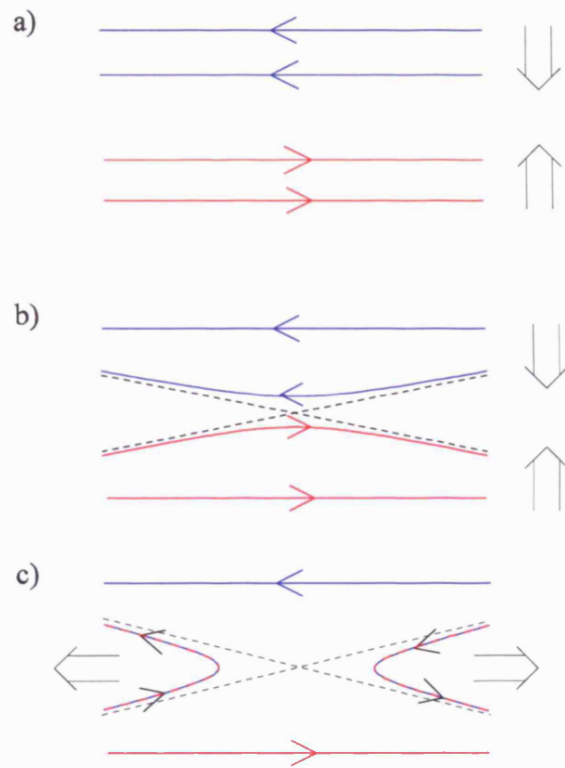
Figure 1.1: Basic, schematic representation of the magnetic reconnection process. a) Oppositely directed magnetic field lines of two different plasma regimes (red lines and blue lines) come together as shown by the arrows; b) the two magnetic field lines closest to each other join and break, approximating to an x-line (dashed black lines); c) newly formed magnetic field lines (red-and-blue lines) accelerated away from reconnection point as shown by the arrows to allow further reconnection.

1.2 Sun, solar wind and interplanetary magnetic field

Our Sun is a star consisting of several levels of structure (Figure 1.2). At its centre is the core, where nuclear fusion converts hydrogen to helium to keep the star active. The next levels are the radiative and convective zones, where the energy from the reaction in the core is transported to the outer layers of the Sun. The photosphere of the Sun is the visible layer, and overlying that are the chromosphere and the corona. The corona consists of hot plasma; in this case mostly hot protons and electrons, and a small quantity of He^{2+} and heavier ions.

The solar wind plasma is accelerated away from the Sun due to the huge difference in gas pressure between the solar corona and interstellar space and the high temperature ($\sim 5 \times 10^6$ K or more) of the plasma, allowing it to overcome the Sun's gravitational attraction. The frozen in condition (Equation 1.8) has the effect that the solar wind plasma is constrained to carry the Sun's magnetic field with it. Since the Sun rotates on average once every 27 days (slightly fewer at the equator, more at the poles) the magnetic field lines of the Sun are twisted into a spiral shape as they are carried by the plasma into interplanetary space (Figure 1.3). The resulting magnetic field is referred to as the interplanetary magnetic field (IMF).

1.3 Magnetosphere

The Earth's magnetic field is approximately dipolar to ~ 4 R_E (where 1 $R_E \sim 6400$km). The action of the solar wind pressure upon it compresses it to little more than 10 R_E on the dayside, and stretches it into a long tail on the nightside, many hundreds of R_E in length.

4
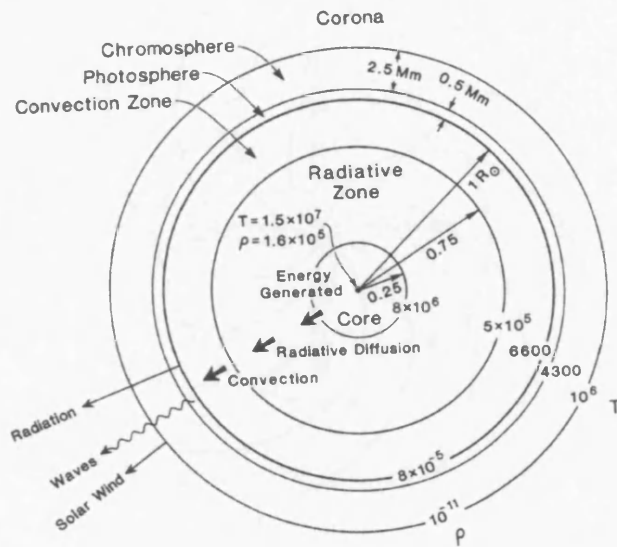
Figure 1.2: The structure of the Sun. At its centre is the core, after which are the radiative and convective zones. The photosphere and chromosphere follow, and finally the corona (from Kivelson and Russell, 1995).
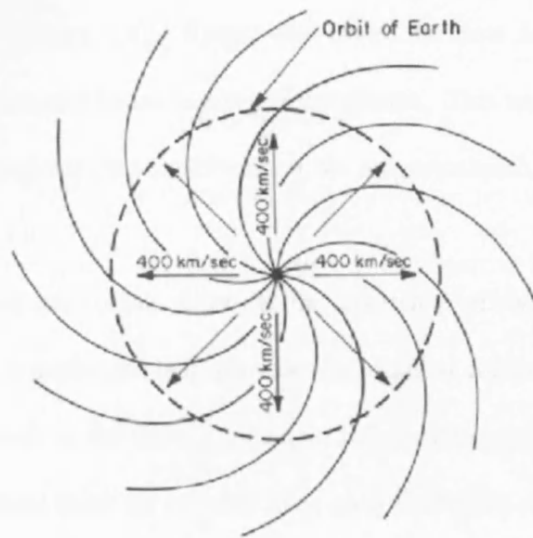
Figure 1.3: Spiral shape of magnetic field lines travelling away from the sun is shown, with the Earth's orbit superimposed (from Kivelson and Russell, 1995).

As the solar wind travels at supersonic speeds it creates a bow shock where it hits the Earth's magnetic field (Figure 1.4). Across this shock the flow is slowed down, which results in the compression and hence heating of the plasma. This turbulent layer of plasma where the two plasma regimes find equilibrium is the magnetosheath, shown in Figure 1.4.

The frozen-in condition can break down at the boundary of the magnetosheath - the magnetopause - where a southward IMF provides the optimal condition for reconnection at the dayside magnetopause as the Earth's magnetic field points north at that location. The resulting reconnected field lines are referred to as open field lines as they are connected to both the Sun and Earth's magnetic fields. The plasmas on these magnetic field lines are a mixture of both solar and terrestrial plasmas. Closed field lines are those connected to either the Earth's magnetic field or the Sun's, but not both. The newly-opened field lines are pulled over the Earth's poles, with their footprint on the Earth moving over the polar caps in an anti-sunward motion. The field lines are pulled further out in an anti-sunward direction into the magnetotail of the magnetosphere. At around 100 R_E the northern and southern hemisphere open field lines become sufficiently close for reconnection to occur; this is at the distant neutral line (DNL). The closed field lines tailward of the DNL are carried downtail to rejoin the IMF. The closed field lines Earthward of the DNL travel back around to the dayside to begin the process again; this is the Dungey cycle (Dungey, 1961), resulting in an open magnetosphere (Figure 1.4). The footprints of these magnetic field lines in the ionosphere form a two-cell convection pattern within the polar cap region, with opposing flows forming a flow reversal boundary (Figure 1.5, top row, middle panel).

The presence of a By component of the IMF complicates matters. A positive By results in a larger dusk convection cell, whilst negative By results in a larger dawn convection cell
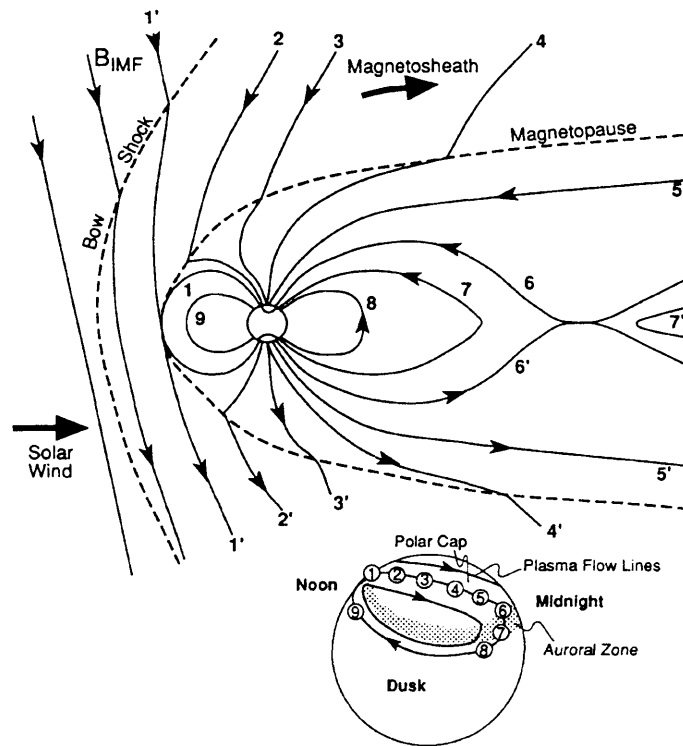
Figure 1.4: Magnetic field lines of the solar wind and magnetosphere driving plasma flow by magnetic reconnection at the front of the magnetosphere and in the magnetotail. The numbered field lines' footprints in the ionosphere are shown in the inset, the black lines depicting the antisunward flow over the polar cap and the return flow at lower latitudes (from Kivelson and Russell, 1995).

(Figure 1.5, top row, first and third panels). When the IMF is northward, reconnection can still occur but in this case the reconnection is between the IMF and open magnetic field lines of the Earth's magnetotail. In this case the footprint of the magnetic field lines in the ionosphere is very different; a four-cell convection pattern is produced (Figure 1.5, bottom row, middle panel). The By component is also important in this case, a positive By resulting in a larger polar dawn convection cell (Figure 1.5, bottom row, last panel) and a negative By resulting in a larger polar dusk convection cell (Figure 1.5, bottom row, first panel).

The volume within the magnetopause is shown in Figure 1.6. It is divided in two by the plasma sheet, a region of hot plasma with high plasma density. The plasma sheet is encased by a thin layer of hot, mostly field-aligned plasma called the plasma sheet boundary layer. Above and below the plasma sheet are the magnetotail lobes which are of low plasma density, within which are open field lines. Within geostationary orbit is the plasmasphere which corotates with the Earth. It is formed from ionospheric plasma that follows magnetic field lines until the gas pressure along the magnetic field lines between the ionosphere and magnetosphere is equalized. In the same region are the radiation belts, particles in orbits circling the earth on closed magnetic field lines.

Within the magnetosphere there exist a number of current systems. The magnetic field lines of the northern tail lobe and plasma sheet are Earthward-directed (into the northern polar cap) and those of the southern lobe and plasma sheet are tailward directed (out of the southern polar cap). This magnetic field geometry is supported by a duskward-directed cross-tail current sheet located in the equatorial plane, at the centre of the plasma sheet (Figure 1.6). This current closes on the magnetopause, where Chapman-Ferraro currents
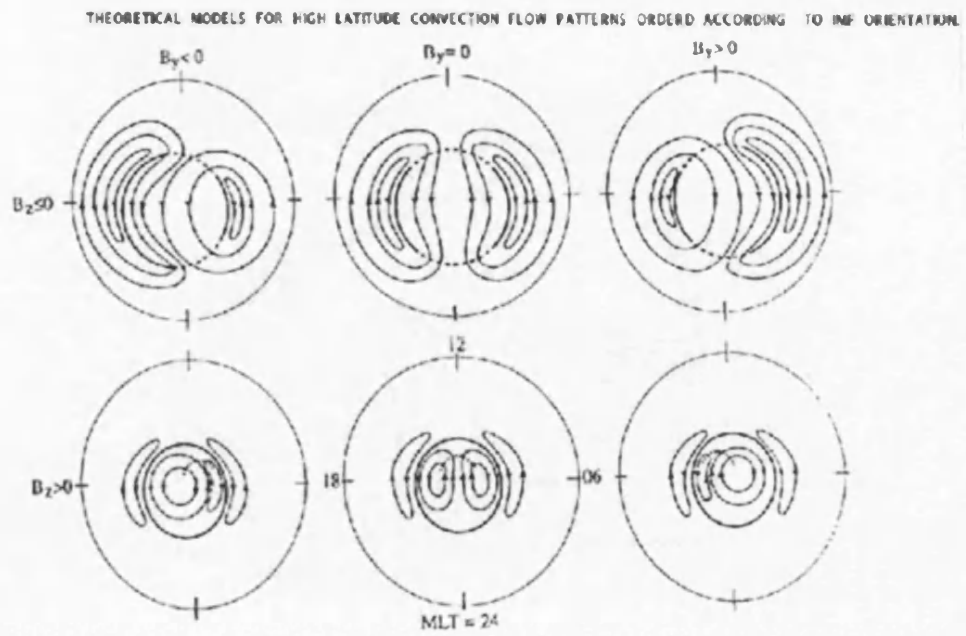
Figure 1.5: Depicts the footprint of magnetic field lines in the polar cap region for the cases where Bz<0 (top row) and Bz>0 (bottom row), and where By<0 (left column), By=0 (middle column), By>0 (right column) (after Cowley and Lockwood, 1992).
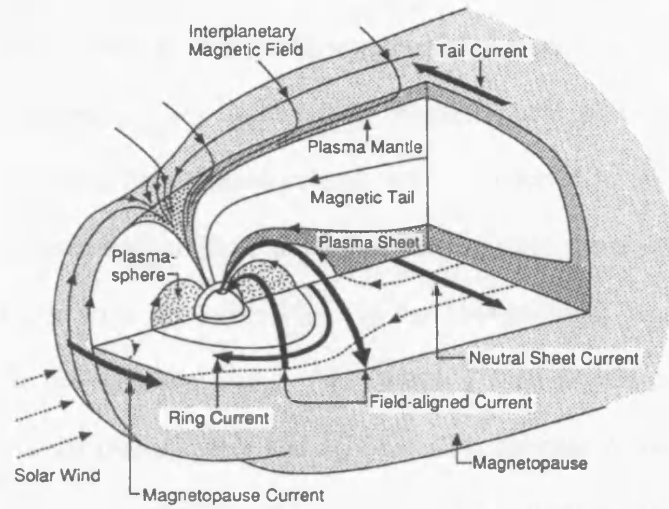
Figure 1.6: Cutaway of the magnetosphere depicting the plasma regimes, fields and currents of the magnetosphere (from Kivelson and Russell, 1995).

support the boundary between the hot, turbulent magnetosheath plasma and the cold plasma of the lobes. There is a westward flowing ring current in the inner magnetosphere formed from geomagnetically trapped particles flowing in circles around the Earth. There are also partial ring currents which flow in the middle magnetosphere, partway around the Earth. Region 1 and Region 2 field-aligned currents are also referred to as Birkeland currents; Region 1 field-aligned currents flow in the interface between the plasma sheet and lobes, into the ionosphere from the magnetotail in the post-midnight sector and out of the ionosphere in the pre-midnight sector. The Region 2 field-aligned currents flow on the outer boundary of the plasmasphere and are oppositely directed to the Region 1 currents. They are located at lower latitudes in the ionosphere and connect the ends of the partial ring currents to the ionosphere.

1.4 Ionosphere

The Earth's atmosphere is stratified due to Earth's gravity. The lowest atmospheric region is the troposphere, separated at ~10 km above ground level by the tropopause from the next layer, the stratosphere. At about 50 km above ground level is the stratopause, above which is found the mesosphere. The mesopause is located at ~100 km, above which is the thermosphere. The thermosphere is coupled to the ionosphere. The ionosphere is a region of partially ionised plasma located from ~70 to 1500 km above Earth. The ionosphere is made up of different levels of ionisation, called the D, E and F layers (see Figure 1.7).

The D layer is the region of the ionosphere closest to Earth, located below ~80 km altitude. The D layer absorbs HF radio waves, particularly in the daytime, as the ionization in this layer is relatively low. The E layer is found at around 110 km altitude. The ionization in
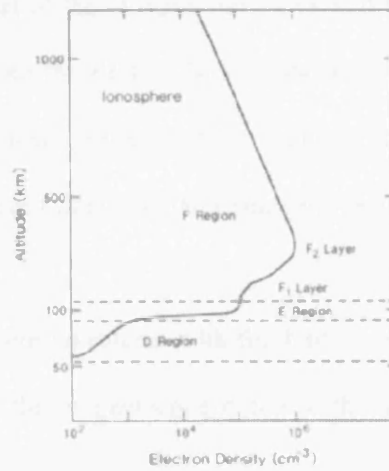
Figure 1.7: Depicting the different regions of the ionosphere (from Kivelson and Russell, 1995).

the E layer is higher than that of the D layer and as a result it can be used to reflect radio waves. Above the E layer are the F1 (~ 170 km) and F2 (~ 250 km) layers, which also reflect radio waves. These layers are particularly useful as radar instruments may be used to detect their location at a given time, and their changing features over a period of time.

At low latitudes the ionosphere co-rotates with the Earth. However, at higher latitudes it convects as it is coupled to the magnetosphere due to the interaction of ionospheric and magnetospheric electric fields.

1.5 Solar wind – Magnetosphere – Ionosphere system

Many observed phenomena are a result of interactions between the solar wind, the magnetosphere and the ionosphere, of which one of the more visually spectacular are aurora: displays of light in the night sky visible at high latitudes in both the northern and southern hemispheres. These are the result of dayside precipitation from the solar wind, geomagnetic storms, and magnetospheric substorms. Substorms have their origins in the magnetosphere and are due to the loading of magnetic field lines in the magnetotail by the solar wind, followed by high speed Earthward plasma flows which travel along magnetic field lines into the ionosphere. Here the high energy plasma interacts with the atmosphere, losing its energy in the form of a photon and thereby creating the aurora.

This thesis is concerned with the ground space observations of magnetospheric substorms. Substorms and substorm theory are the subject of the next chapter where both are discussed in greater detail. In particular, substorm onset mechanism models will be reviewed. The

8

third chapter will discuss the technical aspects of a variety of scientific instruments from which data have been used in the three studies. These studies are presented in full in the fourth, fifth and sixth chapters. Finally a conclusions section will summarize the work undertaken and also make suggestions for further work.

Chapter 2

Background Theory

This chapter will introduce in detail the background theory to substorms, the key signatures of substorms, the main substorm onset models, and substorm-related phenomena.

2.1 Introduction to substorms

The first working model to explain substorm phenomena was produced by Akasofu (1964) after he examined all-sky films of numerous substorms from Alaska, America and Canada in an attempt to piece together the relationship between the visual features seen at the different locations. He concluded that substorms consisted of two phases, the expansion phase and the recovery phase, and the essential features are shown in Figure 2.1. For each plot, the sun direction is to the top, with dawn to the right and dusk to the left.

The quiet state of the polar region is shown in panel A, occurring when there has been no auroral activity in the polar caps for a few hours. Homogeneous arcs, some very faint, are seen around midnight. These arcs lie approximately parallel to lines of geomagnetic latitude but are more curved.

The first phase, called the expansion phase, is characterised by the sudden brightening of a
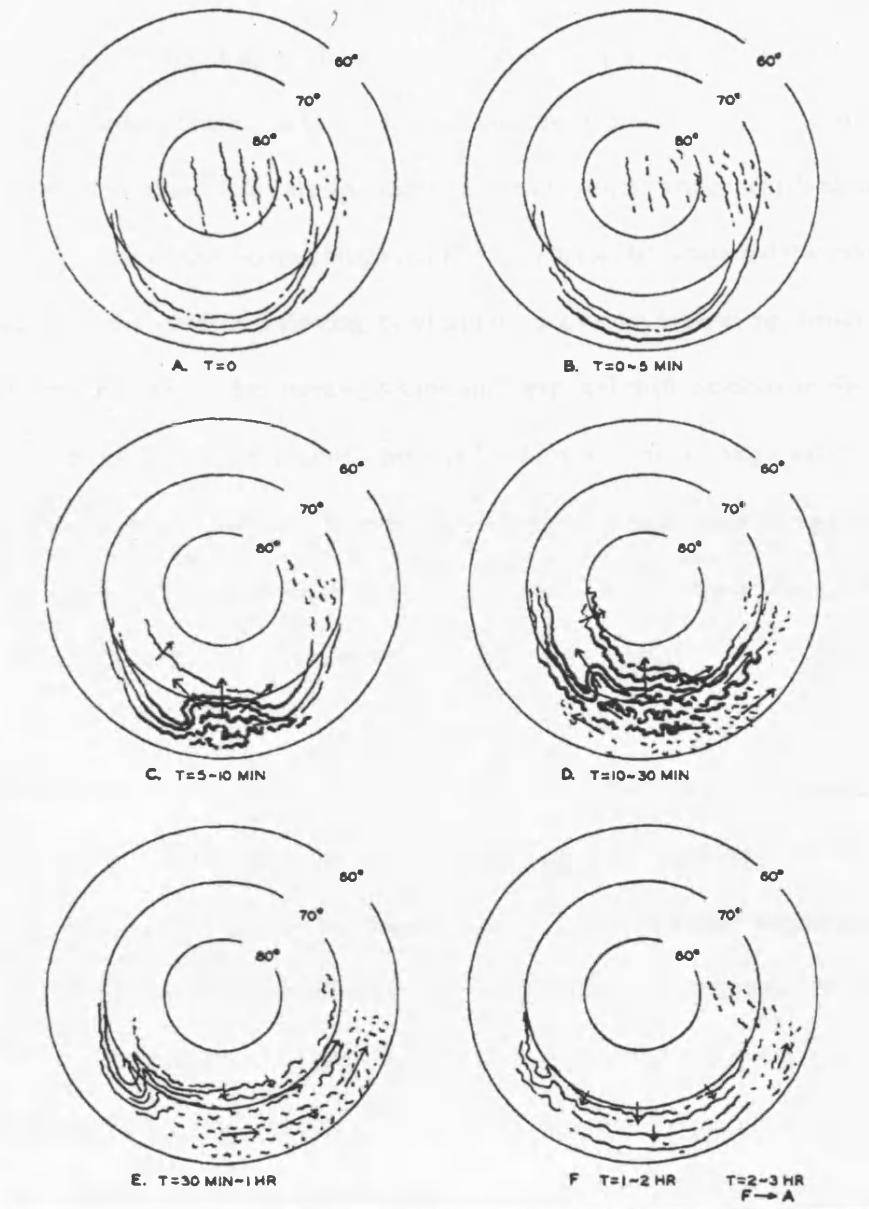
Figure 2.1: Depicting the stages of the two phases of substorms as described by Akasofu (1964).

section of the auroral arc located near to the midnight sector (thickened arc closest to equator, panel B) and the rapid poleward movement of that arc resulting in a bulge in the midnight sector (panel C). If the substorm is weak then the poleward motion does not last for more than a few minutes, resulting in a pseudobreakup (Akasofu, 1964). When the front of the expanding bulge reaches its highest latitude (typically ~75°, depending on the intensity of the substorm), folds are formed in the early evening sector which move rapidly westward as a result of the moving bulge (panel D). This is the westward travelling surge. Equatorward of the poleward-moving brightening, active or broken up bands produce westward drift motions in the evening sector and eastward drift motions in the morning sector. Well-defined bands drift rapidly eastward and are known as omega bands. Isolated, cloud-like patches in the dawn sector, equatorward of the omega bands and eastward drift motion, are a result of the break-up of arcs in this region. The expansion phase lasts around 10 - 30 minutes, in contrast to a typical substorm lasting 1 - 3 hours.

The recovery phase begins when the northern-most active band reaches its highest latitude. It frequently stays at this northernmost point for up to ~10 - 30 minutes then moves equatorward, reducing the size of the bulge (panel E). The westward surges decrease in speed, and either break up into small-scale folds if they are not very intense, or form well-defined loops. The brightness of arcs located in the evening sector is decreased. In the morning sector, the arc structure disappears, leaving eastward-drifting patches spread over a wide area. After 1 - 2 hours, the equatorward motion of arcs continues, the loops formed in the evening sector break up and some drifting patches may still be visible in the morning sector (panel F). The brightness of the arcs reduces, and the configuration returns to its quiet state.

McPherron (1970) developed the idea of a third phase, the growth phase, which precedes the expansion phase. The onset of the growth phase is the time at which the rate of erosion of the dayside magnetopause through magnetic reconnection increases as a result of a southward turning of the IMF, typically 30 - 60 minutes before substorm expansion phase onset. As magnetic flux is eroded from the dayside, the boundary of the magnetopause moves closer to Earth. The magnitude of the magnetic field in the lobes and their corresponding pressure both increase as a result of the increased magnetic flux transported to the magnetotail by the solar wind (e.g. Fairfield and Ness, 1970). To balance this, the tail currents are strengthened and move closer to Earth, thereby increasing the flaring of the magnetopause and causing the plasma sheet to thin in the near tail (e.g. Nagai et al., 1997). Weak magnetic bays and westward electric fields develop in the auroral zone, and weak electron precipitation also begins.

A phenomenological model for substorms incorporating all three phases was then developed. The paper by McPherron et al (1973) was the culmination of eight papers based on two substorm events, using data from many sources. The following phenomenological model was complied from these. Satellite observations of these two substorms showed two clearly defined phases, the growth and expansion phases, whilst the recovery phase was most apparent in the ground observations. The ground and satellite data were therefore split into four parts: growth phase, expansion phase onset, expansion phase and recovery phase. This allowed direct comparison of the substorm events and the substorm model followed from this.

Firstly the growth phase, corresponding to the accumulation of magnetic flux in the magnetotail following a southward turning of the IMF (Figure 2.2, panel a). The
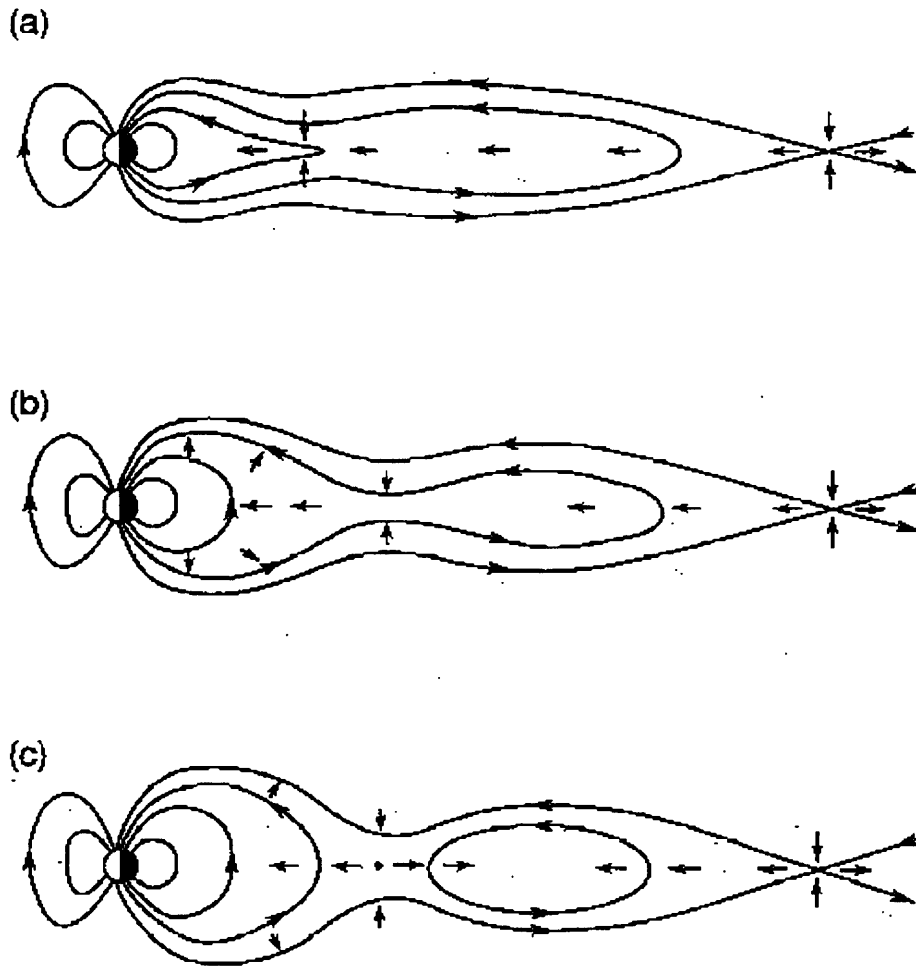
Figure 2.2: Depicting the configuration of the magnetotail during a) the growth phase, b) at substorm expansion phase onset and c) after onset, with plasmoid propagating downtail (from Cowley, 1996)

magnetotail is stretched and the plasma sheet flattened as the magnetic field strength in the lobes increases. The substorm expansion phase onset begins at the time when the near tail plasma sheet thins almost completely (Figure 2.2, panel b). At this time a strongly negative H (north-south) component magnetic bay is detected in the midnight sector of the auroral zone simultaneously with an intense southward electric field. Large amplitude magnetic fluctuations and energetic particles are detected in the plasma sheet as it expands once more. Inside the plasma sheet the field magnitude increases. In the lobes of the magnetotail the magnetic field magnitude decreases, and after some delay the lobe field becomes more dipolar. In the auroral zone, the westward electrojet developed during the growth phase now expands northward and westward, simultaneous to more intense electron precipitation. The plasmoid, formed as a result of near-tail reconnection cutting through the entire thickness of the plasma sheet, propagates downtail (Figure 2.2, panel c). Approximately 30 min after onset the auroral electrojet currents begin to decay indicating that the substorm has progressed to the recovery phase, during which the magnetotail returns to its quiet time configuration.

From this phenomenological model developed a number of substorm onset models which attempted to explain the triggering of the substorm in terms of signatures detected. These will be discussed further in Section 2.3.

2.2 The structure of the magnetotail

2.2.1 Regions of interest

The northern and southern lobes are where magnetic flux accumulates as a result of an increased reconnection rate at the dayside magnetopause but with no corresponding increase in reconnection rate at the distant neutral line to remove the added flux. The lobes are of very low plasma density, typically ~ 0.01 ions cm^{-3}. The plasma sheet is much more densely populated with ~ 0.5 ions cm^{-3}. This region is bisected by the cross-tail current sheet which flows from dawn to dusk and supports the magnetic field geometry in this region where oppositely-directed magnetic fields are in close proximity. During the growth phase the plasma sheet is thinned by the greatly increased magnetic pressure of the northern and southern lobes; there is a corresponding increase in the density of the cross-field current. At substorm expansion phase onset the near-Earth plasma sheet expands suddenly, corresponding to the dipolarisation of the magnetic field following near-Earth reconnection (Hones, 1979). A spacecraft located Earthward of the near-Earth neutral line reconnection will detect a dipolarisation in the magnetic field. Dependent upon its location and the extent of the reconfiguration of the magnetotail, a spacecraft may also detect the plasma sheet expanding over the spacecraft.

2.2.2 The field-aligned current (FAC) system

The characteristics of large-scale field-aligned currents (FACs) were first investigated by Iijima and Potemra (1978). Statistical analysis of magnetic field data from the TRIAD

14

satellite revealed two rings of current encircling the magnetic pole and located at different latitudes. The poleward currents, which flowed into the ionosphere on the dawn side and away from the ionosphere on the dusk side, were named the Region 1 (R1) currents. The equatorward currents were of opposite polarity; these were named the Region 2 (R2) currents.

The system of field aligned current systems in the Earth's magnetosphere transmit energy and stress between the different regions of the magnetosphere, allowing coupling between the magnetosheath and magnetosphere, the magnetosphere and the ionosphere, and the ionosphere and thermosphere (Cowley, 2000). They are also coupled to each other allowing transfer of energy and information between all regions of the magnetosphere.

The ionospheric footprints of magnetic field lines that are reconnected at the dayside magnetopause are pulled over the polar cap and then return to the dayside at lower latitudes after further reconnection in the magnetotail. This is referred to as ionospheric convection and their patterns are well established (Cowley and Lockwood, 1992). The ionospheric plasma particles collide with particles in the neutral atmosphere at lower altitudes resulting in drag on the flow and heating of the neutral particles. The drift magnitude and direction are dependent on the ratio of the collision frequency to the gyrofrequency. For electrons the gyrofrequency is larger than that of ions. Electrons **ExB** drift at all altitudes. The magnetic field strength is approximately constant over the altitudes considered, while the collision frequency is dependent on the neutral density, which increases with decreasing altitude for ions. Therefore in the region below ~125 km, the **ExB** drift becomes negligible and ions drift mostly in the **E** direction. Above ~125 km ion drift is in both the **ExB** and **E** directions. At around 125 km altitude ion drift is between the **ExB** and **E** directions.

15

The result of this is that a field-perpendicular electric current flows at low altitudes in the lower ionosphere, composed of the Pedersen current in the direction of **E** and the Hall current in the -**ExB** direction (Cowley, 2000). The Pedersen current dominates above 125 km, the Hall current below. The **jxB** force produced by these currents is sufficient to balance the neutral drag force, with **j**$_P$**xB** opposing the drag force in the **ExB** direction and the **j**$_H$**xB** force opposing it in the E direction.

The Hall current travels opposite to the direction of flow and is closed in the ionosphere whereas the Pedersen current cannot close in the ionosphere. This is the origin of the Region 1 and Region 2 field aligned currents (Figure 2.3). The high latitude dawn to dusk Pedersen current drives the Region 1 system, flowing in the open-closed field line boundary and closing on the magnetopause. The lower latitude Pedersen currents drive the Region 2 current system, which flows in the inner plasma sheet and ring current region, closing on a partial ring current.

2.2.3 The substorm current wedge

The substorm current wedge (SCW; McPherron et al., 1973) is presented in Figure 2.4. It consists of field-aligned currents directed both into and out of the ionosphere, which are closed in the ionosphere by a westward auroral electrojet and in the tail by a duskward directed current. This model developed as a consequence of the observations made both at geosynchronous orbit and at mid-latitudes on the ground.

The mechanism proposed by Shiokawa et al (1998) for substorm current wedge formation

16
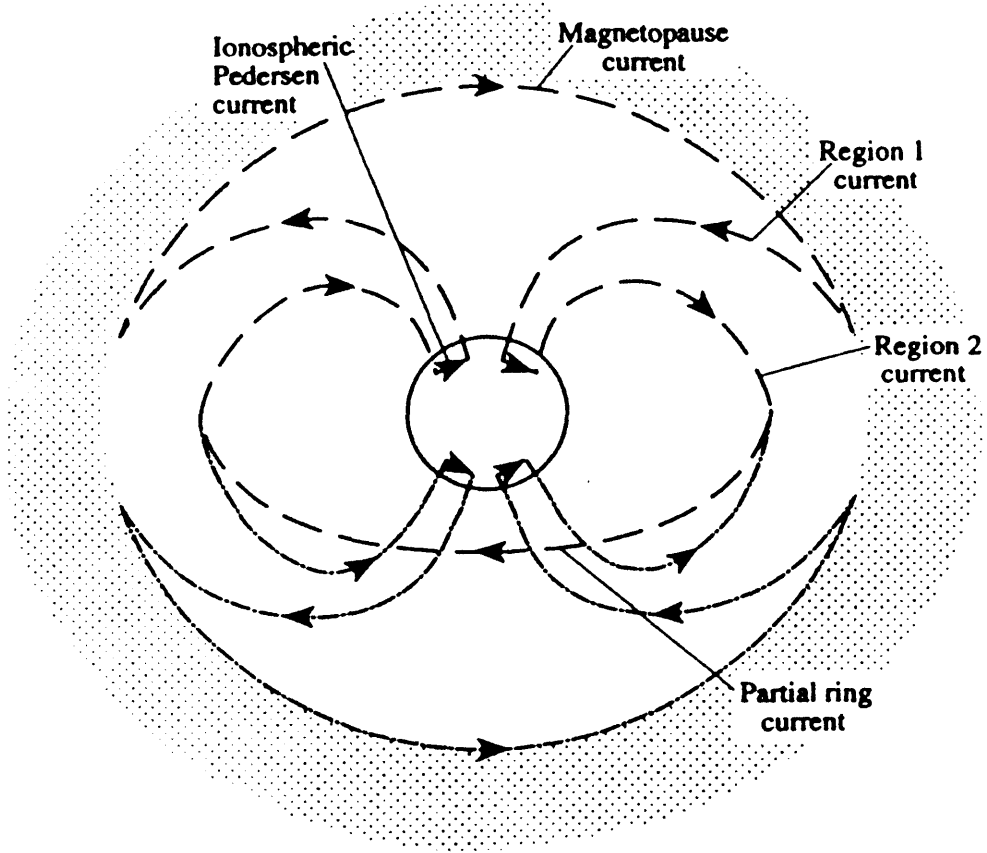
Figure 2.3: Diagram depicting the Region 1 and Region 2 current systems as viewed from the magnetotail, from Cowley (2000).
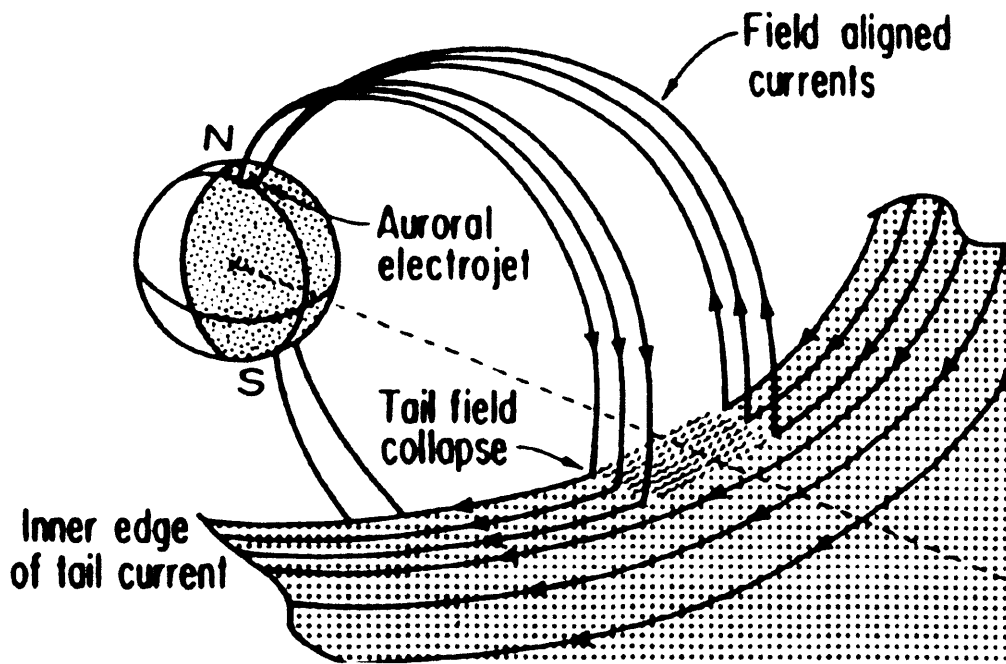
Figure 2.4: Diagram of the substorm current wedge from McPherron et al., 1973

is as follows (see Figure 2.5). During the growth phase of a substorm magnetic field lines are accumulated in the magnetotail lobes and this causes the near Earth magnetic field to distort from its dipolar shape to a more tail-like configuration. At substorm expansion phase onset the distorted tail field dipolarizes and x-type reconnection in the near-tail (1) leads to high-speed Earthward ion flow in the neutral sheet (2). Stretched field lines collapse Earthwards at equatorial latitudes and flow braking creates a pileup of magnetic flux, leading to a dawnward inertia current at the boundary between stretched and dipolarized field lines (3) and setting off a compressional pulse towards Earth (4). The region over which dipolarization takes place is of limited azimuthal extent. Within this region in the near tail the cross-tail current is reduced and diverted along the field lines, Earthward on the dawn side and tailward on the dusk side (4). The current flows in the boundary between the dipolarized and tail-like field lines and supports the shear between magnetic field lines at this boundary. These newly formed field aligned currents close in the ionosphere on the westward substorm electrojet, forming the substorm current wedge. The Earthward-travelling tail-like field is braked at the boundary between the dipolar and tail-like fields creating a dawnward directed current that contributes to the formation of the substorm current wedge. The corresponding plasma in this region forms a partial ring current that closes on the existing Region 2 currents.

2.3 Substorm signatures

2.3.1 Ionospheric signatures

The clearest signature of a substorm is the visual display created by the auroral emissions

17
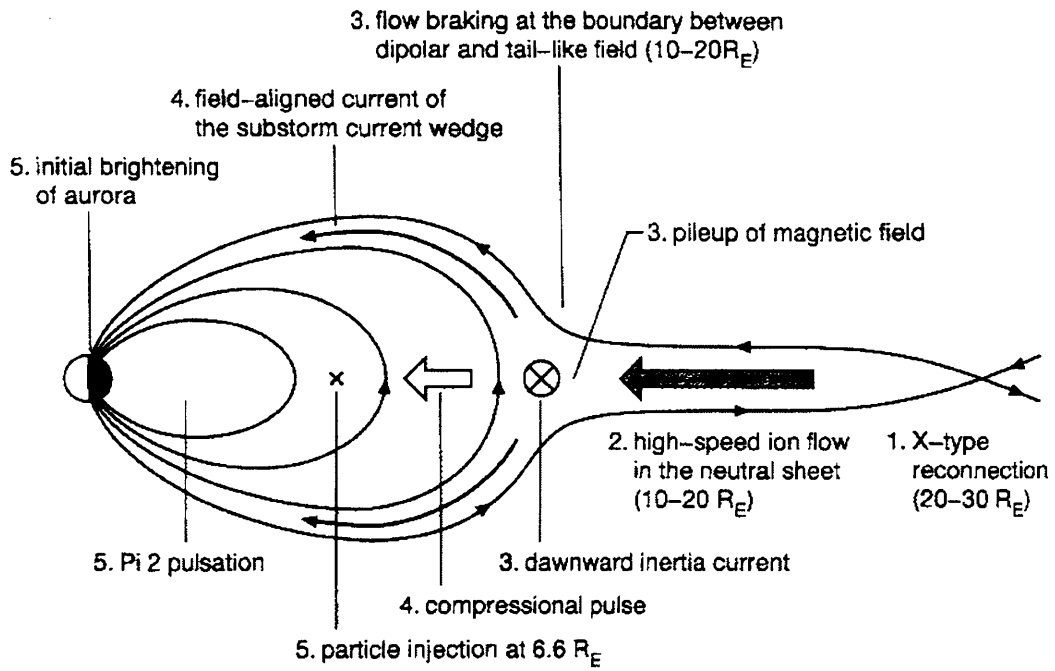
Figure 2.5: Depicting the proposed model for substorm current wedge formation (from Shiokawa et al., 1998)

as originally described by Akasofu (1964). The aurora is a result of collisions between precipitating particles and neutral atoms. The neutral atoms are ionised and subsequently return to their lower energy state, releasing a photon in the process. The precipitating particles have energies typically between a few tens of eV and a few hundred keV, resulting in maximum ionisation rates occurring at ~ 80 – 140 km altitude. The different colours seen in the aurora are due to the atom which is emitting the photon, its electrical state and the energy of the precipitating particle with which it collided. Atomic oxygen is responsible for the most commonly produced colour, green (557.7 nm), and also red (630.0 nm), whilst nitrogen is responsible for the rarer appearance of blue (427.8 nm). All-sky cameras and satellite images can be very effective in detecting this visual display. A very clear auroral arc brightening is usually evident, and over time the development of the auroral bulge and its poleward motion can be followed (e.g. Frank et al., 1998). Other signatures detected by these images include omega bands and the westward travelling surge.

Ground-based magnetometers can detect the strongly negative bay in the H (north-south) component at substorm onset as a result of the formation of the westward electrojet. The location of the electrojet can be inferred from the H component signatures at several stations, and also from the Z (down into the Earth in the northern hemisphere) component. Pi2 pulsations are irregular, damped ULF waves with a period of approximately 40 to 150 seconds (Saito, 1969) and are used as an indicator for substorm expansion phase onset time. They are detected by numerous magnetometers near-simultaneously over a large range of latitudes and local times.

Ionospheric flows are mapped very effectively by ionospheric radars, in particular the

SuperDARN array of radars (Section 3.2). The two-cell convection pattern can be clearly mapped using the map potential technique (Section 3.2), allowing estimates of the size of the polar cap. Anti-sunward flows over the polar cap can be identified, as can the convection reversal boundary (CRB, the boundary between eastward flow at lower latitudes and westward flow at higher latitudes). Highly variable velocity intensifications which move equatorward from the poleward boundary of the auroral zone (Yeoman and Lühr, 1997) are known as poleward boundary intensifications (Lyons et al., 1999) and are signatures of bursty bulk flows in the tail (e.g. Grocott et al., 2004, Nakamura et al., 2005)

Bursty bulk flows (BBFs; Baumjohann et al., 1990) are Earthward-travelling, high speed plasma flows of short duration, typically lasting ~10 minute with variations occurring over ~1 minute or less. They travel at velocities greater than 400 km s^{-1} and are found in the plasma sheet boundary layer, the outer central plasma sheet and the neutral sheet. They are an important mechanism for the Earthward transportation of plasma and magnetic flux.

2.3.2 Geosynchronous signatures

At geosynchronous orbit the substorm onset is characterised by the detection of dipolarization of the magnetic field, whereby there is an increase in the z component and a decrease in the x component of the magnetic field due to the large scale reconfiguration of the magnetotail (Slavin et al., 1997). Plasma injections are also detected at geosynchronous orbit (e.g. Belian et al., 1978). For a spacecraft located in the same local time as onset the plasma injection is dispersionless: the injection occurs at the same time for ions and electrons of all energies. For spacecraft which are distributed in local time, the injection

becomes distributed, with higher energy electrons and ions detected before their slower counterparts; electrons drift eastwards and ions westwards (Birn et al., 1997).

2.3.3 Travelling compression regions (TCRs)

A consequence of the formation of a NENL together with the distant neutral line is the formation of a region of entirely closed magnetic flux, or plasmoid (Hones et al., 1984). At distances greater than ~30 R_E downtail plasmoid-type flux ropes from 10 R_E long have been detected travelling mostly tailward as found in ISEE and Geotail studies (Ieda et al., 1998). Between 20 and 30 R_E downtail smaller flux ropes of 1 to 5 R_E in diameter have been detected travelling both Earthward and tailward in equal numbers by Geotail (Slavin et al., 2003).

Travelling compression regions (TCRs) are intensifications of the lobe magnetic field caused by the movement of plasmoids within the magnetotail (Figure 2.6). The presence of the plasmoid forces the lobe magnetic field lines to compress around it, and these compressions appear to move as the plasmoid moves through the tail. TCRs can be detected as perturbations in the north-south component of the magnetic field and by simultaneous enhancements in the intensity of the tail field magnitude. When the TCR passes a spacecraft these perturbations are bipolar in nature, reflecting the motion of the plasmoid. A north-then-south bipolar signature indicates a tailward travelling TCR, and a south-then-north signature indicates and Earthward travelling TCR. The peak in intensity of the field magnitude corresponds to the centre of the bulge created by the passing of the TCR, at the same time that the bipolar signature changes sign.

20
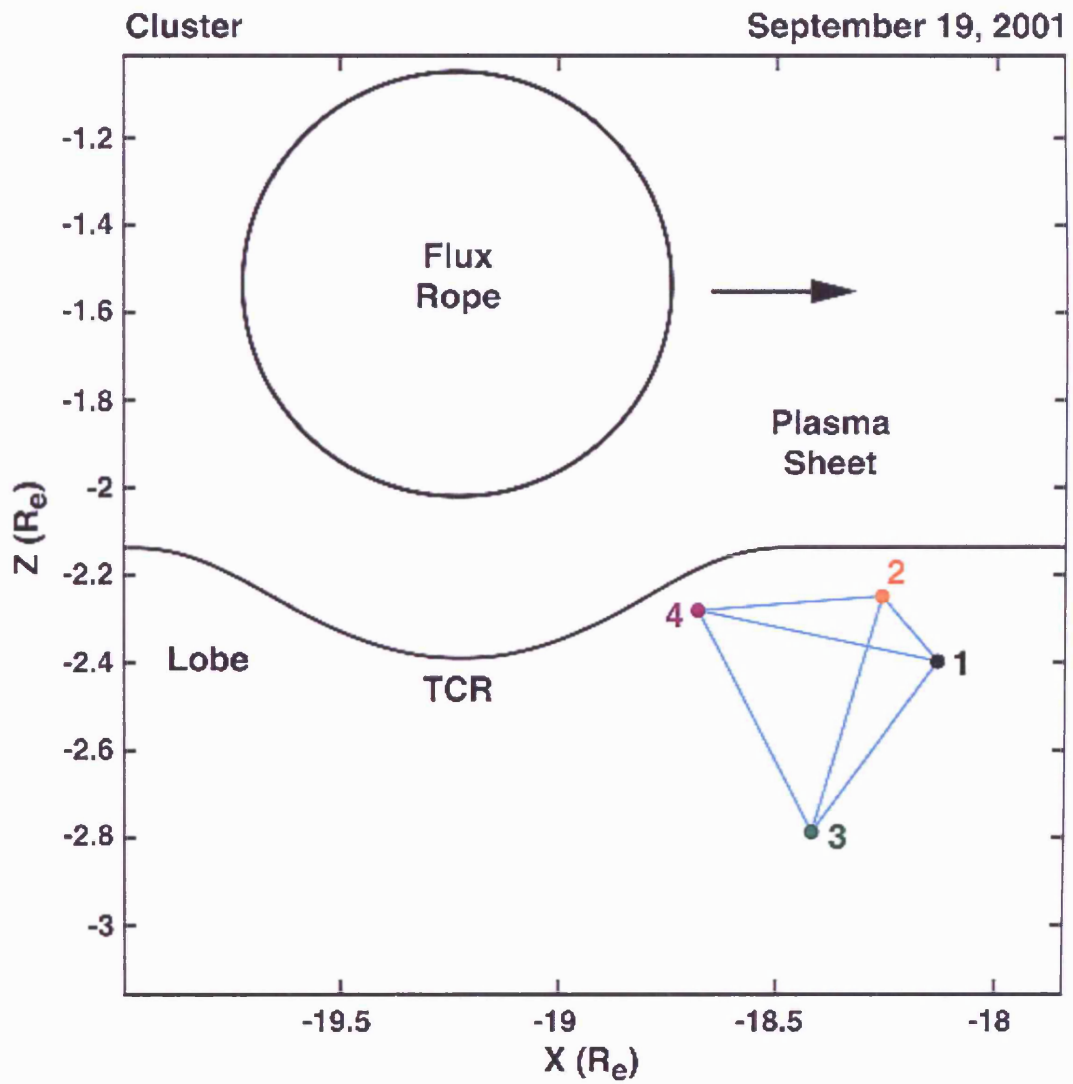
Figure 2.6: Depicting the bulge in magnetic field cause by passing of plasmoid from Slavin et al., 2003.

TCRs are typically detected for a few minutes at a time, and both Earthward and tailward-moving TCRs have been observed; Slavin et al. (2005) showed that 20% of TCRs detected by Cluster within 20 R_E of Earth were tailward directed whilst the rest were Earthward directed. The direction in which the TCR travels is important as it provides information about the location of formation of the plasmoid. If a tailward travelling TCR passes a spacecraft then the near-Earth neutral line (reconnection line) creating the plasmoid formed tailward of the neutral line, and that neutral line must be Earthward of the spacecraft. From the information above, this implies that some 20% of near-Earth neutral lines are definitely formed within 20 R_E.

2.4 Substorm tail dynamics: Substorm onset models

The precise trigger for substorm expansion phase onset is a subject which is still open to debate. Substorm onset models have been developed to fit the known dynamics and data observations, and have broadly developed into two categories, the near-Earth neutral line (NENL; Baker et al., 1996, and references therein) model and the cross-field current instability (CCI; Lui, 1996) model. There are also less widely considered models, including the fast flow braking/modified NENL model proposed by Shiokawa et al. (1998), and a magnetosphere-ionosphere coupling (MIC) model by Kan (1993), and the possibility of external triggering (Lyons, 1995).

2.4.1 Near-Earth Neutral Line (NENL) model

Both observational and theoretical approaches to the near-Earth neutral line (NENL; Baker et al., 1996, and references therein) model of magnetospheric substorms base substorm activity on the phenomenon of magnetic reconnection in the tail. Substorms are controlled by the IMF and generally, although not exclusively, occur after prolonged periods of southward IMF. Southward IMF allows dayside reconnection between the IMF and the Earth's magnetic field, this erosion resulting in a smaller cross section of the magnetosphere. The open field lines are pulled over the polar cap by the solar wind, increasing the magnetic flux in the magnetotail lobes and the cross section of the magnetosphere. This results in increased flaring of the magnetopause and the solar wind pressure on it is therefore increased, balanced by the increasing pressure in the tail lobes from magnetic flux loading. This increase in pressure in the lobes results in increased pressure on the plasma sheet, resulting in a thinned plasma sheet. This thinning of the plasma sheet cannot continue indefinitely; either the plasma sheet would thin until its scale was that of an ion gyroradius, or the dayside magnetopause would be completely eroded through reconnection. Instead, the NENL model predicts that the onset of reconnection is the mechanism by which the closed field lines of the magnetotail are able to return to the dayside.

The spontaneous onset of reconnection at the centre of the current sheet is a result of thinning of the plasma and current sheets during the growth phase, and the subsequent decrease in the vertical magnetic field of the current sheet. Closed magnetic field lines threading the plasma sheet are reconnected first, followed by the open field lines which form the lobes of the tail. The increasing number of reconnected field lines results in the

tailward motion of the x-line. An o-line forms tailward of the x-line which is also carried downtail; this is sometimes referred to as plasmoid. When the last closed field line is reconnected, the plasmoid is 'cut off' from the Earth's magnetic field and moves downtail. Newly-closed field lines are returned to the dayside. The reconnection of field lines in this region decreases the current in the central plasma sheet, disturbing the current flow. Excess current is therefore diverted away from the inner current sheet region and redirected into the substorm current wedge.

Nagai et al. (1998) studied Geotail magnetic field and ion and electron data from November 1994 through July 1996. This covered two different apogees in the magnetotail: $\sim 50\ R_E$ to February 1995 and 10 - 30 R_E after March 1995, and allowed comparison of the data sampled both Earthward and tailward of the expected near-Earth neutral line location. Substorm onsets were identified using ground magnetometer data to time the Pi2 onset. They found that earthward flows associated with onsets were observed only within 30 R_E and that tailward flows associated with southward B_z were observed mostly beyond 20 R_E. These findings constrain the near-Earth neutral line to the region 20 to 30 R_E downtail.

Data from Baker et al. (2002) are presented in Figure 2.7. This is from a study conducted on a substorm which occurred on 27 August 2001. Auroral data (not shown) indicated that substorm expansion phase began between 0406 UT and 0408 UT. The Cluster magnetic field data (B_z component in Figure 2.7, panel a) showed "a positive excursion in B_z at ~0401:30 UT" coinciding with tailward plasma flow (plasma flow moments in Figure 2.7, panel b). Panel c of Figure 2.7 depicts the magnetic field at GOES-8 which detected the main dipolarization later, at 0409 UT. It was concluded that, for this substorm, the observations were in good agreement with the NENL model.

23
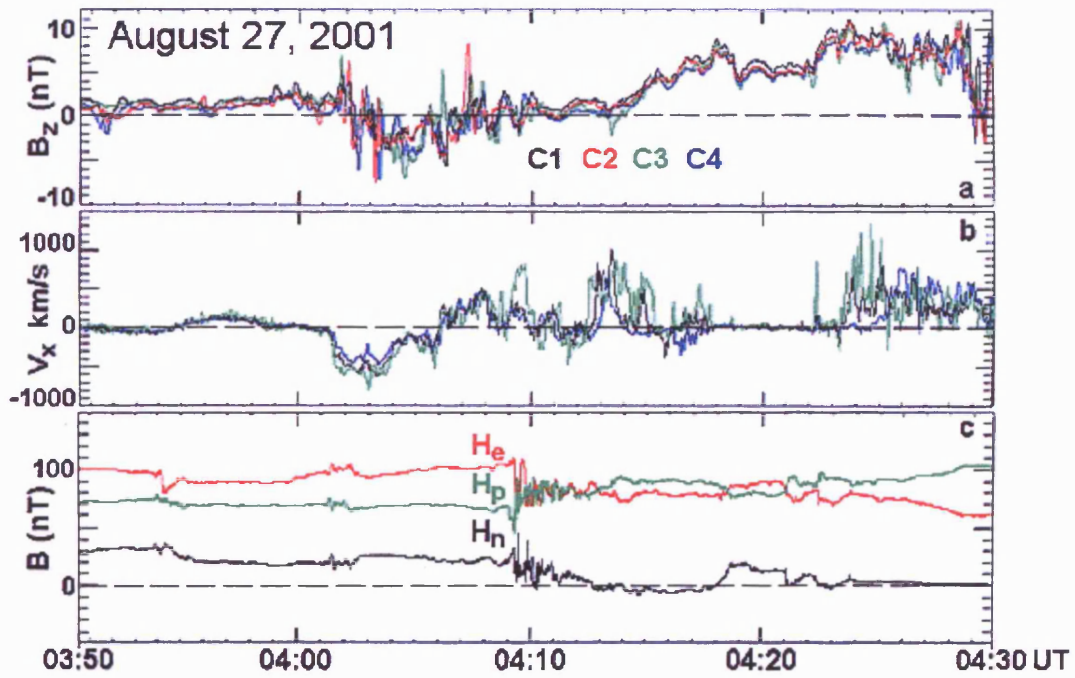
Figure 2.7: (a) Magnetic field Z_{GSM}–component data for the four CLUSTER spacecraft for the period 0352 to 0425 UT on August 27, 2001. Data for each spacecraft are color-coded as shown; (b) Plasma flow moments in the X_{GSM} direction for C1, C3, and C4; (c) GOES-8 magnetic field data (from Baker et al., 2002).

2.4.2 Cross-field Current Instability (CCI) model

The CCI model (Lui, 1996) suggests that current disruption (CD) in the near-Earth current sheet at the start of the expansion phase of the substorm is not caused by spontaneous reconnection of magnetic field lines further down tail. Instead it is a local interaction that is the initiator of the CD and hence the substorm onset and, later, magnetic reconnection.

Shortly before CD the current density is enhanced, the plasma pressure is increased, plasma beta becomes very high and the current sheet reduces in thickness. The cross-tail current becomes very intense. At CD large fluctuations in the magnetic field are detected, magnetic field-aligned counter-streaming beams are detected and a reduction in the cross-tail current. It is postulated that CCI allows plasma to be injected Earthward from the CD site at geosynchronous orbit, usually detected by geosynchronous satellites. Field-aligned currents are generated in this region forming the substorm current wedge and subsequently reconnection at the near-Earth neutral line, downtail from this region, begins.

Miyashita et al. (2001) undertook a superposed epoch analysis of parameters for substorm onsets where the maximum tailward flow speed exceeded 300 km s^{-1}. Figure 2.8 shows 2-minute averages of ΔB_z and V_x changes for such onsets. The time t=0 is the time at which low latitude Pi2 pulsations were detected. The changes in ΔB_z and V_x imply that the NENL formation occurs from 0 – 2 min after this (Figure 2.8). Miyashita et al. concluded that this was strong evidence that the NENL did not form in the minutes prior to onset at the inner plasma sheet.
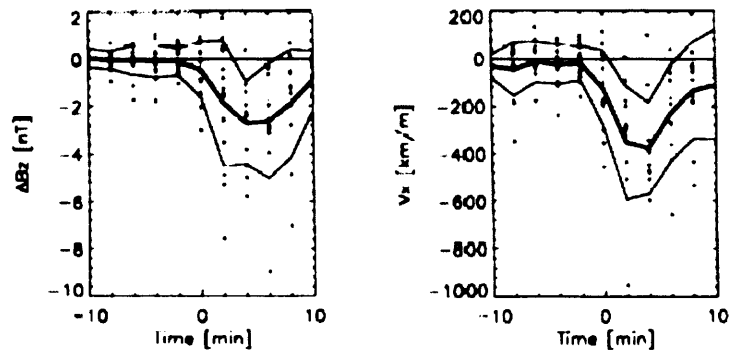
Figure 2.8: Superposed epoch analysis for ΔB_z and V_x for onsets where maximum tailward

flow speed exceeded 300 km s^{-1}. Thick line depicts averages, thin lines the +/-1 standard

deviation (from Miyashita et al., 2001).

2.4.3 Modified NENL model

The fast flow braking/modified NENL model (Shiokawa et al., 1998) is a development of the NENL model. After reconnection in the near-Earth tail, the Earthward ion flow is braked in the region where the tail changes from tail-like to dipolar. This also results in the pileup of magnetic flux. The ion flow is diverted, producing a dawnward inertia current at the boundary between dipolar and tail-like fields and subsequently the formation of the SCW, and auroral brightening is initiated. As flux pile-up continues, this boundary moves tailwards.

2.4.4 Magnetosphere-Ionosphere Coupling (MIC) model

The magnetosphere-ionosphere coupling (MIC) model (Kan, 1993) is based on the CCI model since it does not require x-line formation in the near-Earth tail for substorms to occur. In the MIC model, enhanced reconnection on the dayside loads the open field lines of the lobe and the closed field lines of the plasma sheet. The plasma sheet responds by dipolarizing and forming the substorm current wedge. This occurs when the field-aligned current $J_{||}$, enhanced by magnetosphere-ionosphere coupling, exceeds ~1 $\mu A/m^2$ and the field-aligned potential drop exceeds ~1 kV.

2.4.5 External triggering

The external triggering model (Lyons, 1995) suggests that external triggering by a

northward turning of the IMF is the cause of substorm onset. The northward turning would result in a reduction of the large-scale electric field which would propagate anti-sunward, disrupting particles in the plasma sheet. This would lead to the formation of the substorm current wedge in the near tail, and active aurora.

2.5 Plasma bubbles

Plasma bubbles are predicted to be underpopulated flux tubes which are in pressure equilibrium with their surroundings. The plasma pressure and density within a bubble is reduced and its magnetic field increased, resulting in a decreased cross-tail magnetic drift current. This electrically polarizes the bubble, enhancing the Earthward plasma flow within the bubble and forcing the plasma around the bubble to convect around it (Figure 2.9).

Sergeev et al. (1996) have shown that data from ISEE 1 and ISEE 2 suggest that when the plasma sheet becomes thick, as it does during the recovery phase of a substorm, the plasma and magnetic field signature of BBFs demonstrate the presence of plasma depleted flux tubes, also called "bubbles" (Pontius and Wolf, 1990; Chen and Wolf, 1993). Sergeev et al (1996) also demonstrated that the cross-tail size of plasma bubbles is ~1 - 3 R_E.

2.6 Summary

The magnetospheric substorm is an extremely complicated phenomenon which involves a great number of intricately linked tail dynamics on many scales. Its main signatures, and
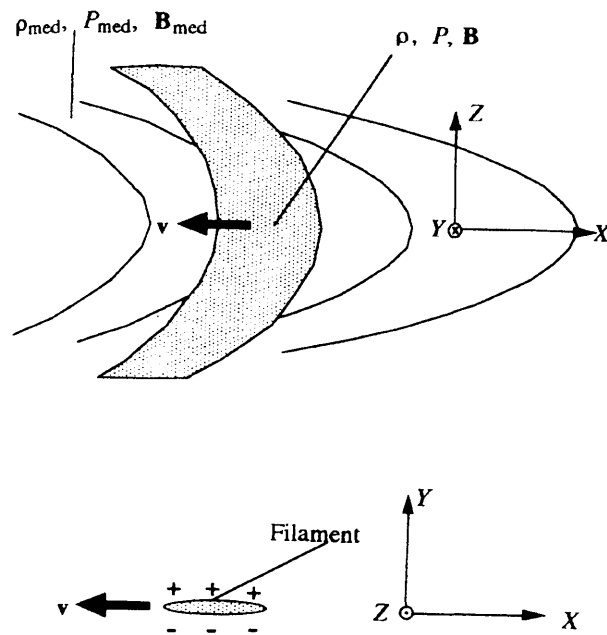
Figure 2.9: Plasma bubble (shaded region) whose shape becomes different from that of neighboring flux tubes (from Chen and Wolf, 1999)

methods by which these may be recorded, are by now well known; however the finer detail, in particular the timing of the events around substorm expansion phase onset, are still a matter of great controversy. Chapters 4 and 5 present two substorm case studies, for each of which a sufficient quantity of data from many sources were available to complete as full a picture as possible of each of the events. The suitability of the substorm onset models discussed above are considered and conclusions drawn for each substorm event. Chapter 6 presents a study of four magnetic cavity events. These are a new feature, the first of which is identified during the interval studied in Chapter 4. They appear similar to, but not the same as, the plasma bubbles described in Section 2.5.

Chapter 3

Instrumentation

Data from a variety of instruments have been utilized in the following chapters in order to build a comprehensive picture of each event studied. Cluster data on the magnetotail magnetic field and plasma populations provide information about the state of the near tail before, at, and after substorm onset, and geosynchronous satellite data can determine the corresponding state of the near-Earth tail. Ionospheric convection flows and ground-based magnetometers provide information about ionospheric convection and current flow, respectively, in the Earth's ionosphere around the time of a substorm, whilst solar wind conditions are important for determining the characteristics of the IMF during this interval. These data combine to provide a global view of each substorm event studied. Instruments located in the magnetotail, on Earth, in the solar wind, and at geosynchronous orbit, from which data will be presented, are described in this chapter.

3.1 The Cluster spacecraft and their instruments

Following the failure at launch of the original four spacecraft of the Cluster mission, a fifth spacecraft named Phoenix was built using the flight spares of the original experiments. As the development work for the Cluster spacecraft had already been undertaken, the cost of rebuilding another three spacecraft was less and so the second set of Cluster spacecraft was

built. These four Cluster spacecraft, now named Rumba, Salsa, Samba and Tango, were launched in two phases, the first pair on 16 July 2000 and the second pair on 9 August 2000. The spacecraft orbit the Earth in an elliptical polar orbit of 3 R_E at perigee up to 19 R_E at apogee with a 57 hour period (Figure 3.1). The orbital precession allows sampling of the entire magnetosphere over time. The novelty of the Cluster spacecraft is that their orbits are designed to bring the four spacecraft into a tetrahedral configuration when the spacecraft are located in key regions of interest, namely the solar wind and bow shock, the magnetopause, the polar cusps, and the magnetotail. This tetrahedral structure provides simultaneous four-point measurements of the region sampled, allowing spatial and temporal variations to be distinguished. The spacecraft separation has varied from 100 km to 5000 km during the lifetime of the mission to date, and will change to larger separations in future. The spin period of each spacecraft is 4 s. Cluster is the first four-spacecraft mission having the ability to study regions of the Earth's magnetosphere and to some extent the solar wind both spatially and temporally. Its operational phase was initially funded from 2001 for two years, an extended mission phase taking it to the end of 2005 and now a new extension of up to four years has been granted to allow further study.

Each spacecraft carries an identical set of 11 instruments to investigate the electric and magnetic fields and charged particles. The instruments from which data are presented in later chapters are the Fluxgate magnetometer (FGM; Balogh et al., 1997); the Plasma Electron and Current Experiment (PEACE; Johnstone et al., 1997); the Cluster Ion Spectrometry (CIS; Rème et al., 1997) experiment; the Research with Adaptive Particle Imaging Detectors (RAPID; Wilken et al., 1997). These instruments are described in more detail below.
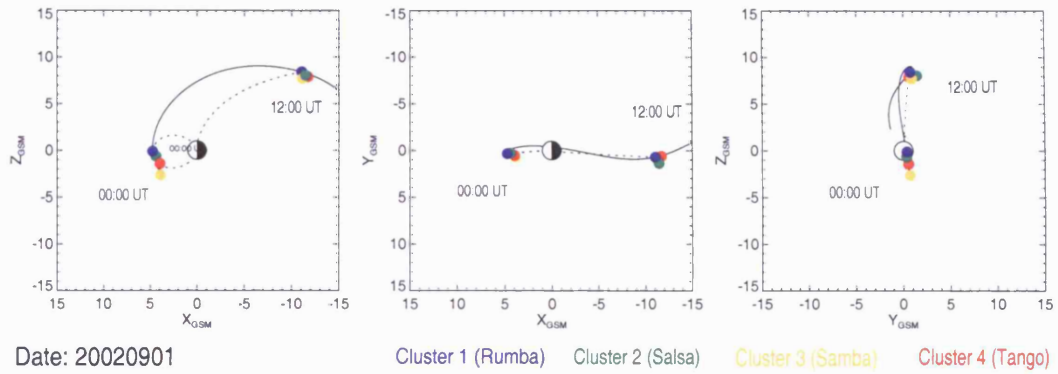
Figure 3.1: Cluster 24 hour orbit for 1 September 2002. Note that at this time of year the tetrahedron is optimized in the magnetotail, but not when the spacecraft are at the magnetopause.

3.1.1 Fluxgate magnetometer (FGM) instrument

Each Cluster spacecraft carries two triaxial fluxgate magnetometers and a Data-Processing Unit (DPU) which comprise the FGM instrument. One fluxgate magnetometer is located at the end of a radial boom 5.2 m in length, and the second 1.5 m inboard from the end of the boom. This avoids interference with the spacecraft. These fluxgate magnetometers are coils of wire, wrapped around toroidal cores of magnetic material. There are two sensors to allow for redundancy in the case of instrument failure. This instrument can take up to 67 samples per second. The data rate used in the studies is 4 s, one sample per spin.

3.1.2 Plasma Electron and Current Experiment (PEACE) instrument

There is one PEACE instrument on each spacecraft which detects the velocity distribution of low to mid energy electrons in the energy range of ~0.7 eV to ~30 keV. The low energy electrons are detected by the Low Energy Electron Analyser (LEEA) while the higher energy electrons are detected by the High Energy Electron Analyser (HEEA). The LEEA and HEEA sensors are on opposite sides of each spacecraft and each samples fully 4π steradians per spin (4 s). The sensors consist of a top hat electrostatic analyser which selects electrons of a narrow range of energies to pass through it to the detector, which registers the arrival of electrons and their approximate directions. Full coverage of the energy range is achieved by overlapping the energy ranges detected by the two sensors and correcting for the geometric factor between the two sensors.

3.1.3 Cluster Ion Experiment (CIS) instrument

The CIS instrument analyses the composition, mass and distribution functions of ions in the 0.02 eV to 30 keV energy range. Its time resolution is that of one spacecraft spin (4 s). Each CIS instrument comprises two parts: the Hot Ion Analyser (HIA) and the time-of-

flight ion Composition and Distribution Function Analyser (CODIF). The CODIF instrument measures three-dimensional distribution functions of H+, He+, He++, and O+ ions, selecting them by their energy per charge ratio using electrostatic deflection followed by time-of-flight analysis. The HIA instrument is similar but does not use the time-of-flight analysis, so that it cannot provide the ion composition data but is suitable for measuring the solar wind's high particle flux. Neither CODIF nor HIA is operational on the Cluster 2 spacecraft and HIA is not operational on Cluster 4.

3.1.4 Research with Adaptive Particle Imaging Detectors (RAPID) instrument

The rapid particle detector detects the highest energy electrons and ions with time resolution of one spacecraft spin (4 s). The Imaging Electron Spectrometer (IES) sensor detects electrons in the 20 to 40 keV range while the Imaging Ion Mass Spectrometer (IIMS) sensor detects ions in the 40 to 4000 keV range. The detectors use time-of-flight and energy detection via a pin-hole system, with 9 sections on the IES and 12 on the IIMS covering 180 degrees in one plane, the remaining azimuthal coverage being provided by the spacecraft spin. The ion detector identifies particles using the particle's velocity (V, calculated from the time-of-flight measurement) and its energy E. These are measured as independent quantities and uniquely determine the ion, since its mass is approximately equal to E/V^2.

3.2 Super Dual Auroral Radar Network (SuperDARN)

The Super Dual Auroral Radar Network (SuperDARN; Greenwald et al., 1995) is a network of virtually identically constructed high frequency (HF) radars located in both the

northern and southern hemispheres. There are currently ten SuperDARN radars in the northern hemisphere (Figure 3.2), the first of which was built in Goose Bay in 1983. The others are King Salmon, Kodiak, Prince George, Saskatoon, Kapuskasing, Stokkseyri, Þykkvibær, Hankasalmi and Wallops Island. The first in the Southern hemisphere was the Halley Station in 1998; the others are Sanae, Syowa South, Syowa East, Kerguelen and TIGER (Tasman International Geospace Environment Radar), which now consists of two radars at Bruny Island and in New Zealand. Some radars function in overlapping pairs; for example the Þykkvibær and Hankasalmi radars together comprise CUTLASS (Co-operative UK Twin Located Auroral Sounding System). Many of the radars in the northern hemisphere have fields of view which are magnetically conjugate to a radar field of view in the southern hemisphere, allowing dual hemisphere studies to be undertaken.

Most of the SuperDARN radars have two arrays of antenna towers, the primary (16 towers) and the secondary (four towers). With this configuration 16 different beam directions can be achieved, the beams being formed by a phasing matrix. The radar transmits a 7-bit pulse sequence in the HF radio band and samples the returned echoes. The resulting data output gives the back-scatter power, the spectral width and the Doppler velocity.

The radars each provide high time-resolution (up to one minute) measurements of ionospheric flow vectors over an area of approximately three million square kilometres. The data are collected from 16 'beams' and over a wide variety of frequencies, allowing a spatial resolution of ~50 km. Data from all radars in one hemisphere can be combined to form a global ionospheric convection map, giving more information than from the individual radar data sets alone. This is done using the map potential technique of Ruohoniemi and Baker (1998). The velocity in any given cell can be resolved in two

32

Figure 3.2: Fields-of-view of the nine northern hemisphere SuperDARN radars (from http://superdarn.jhuapl.edu/index.html)

dimensions if two radars made simultaneous line-of-sight measurements for that cell. However, on the large scale not all areas are covered by two radars and so not all of the convection can be calculated in this way, and a lot of data are wasted if they cannot be merged with other data. However, the map potential model uses all available line-of-sight data in order to constrain the large-scale convection pattern, and the pattern most consistent with the real data is determined by minimizing the sum of the line-of-sight components of the fitted vectors.

The entire SuperDARN network is run on 'Common Time' for at least 50 % of the time, whereby all radars simultaneously run well-defined data acquisition programs: sampling on all 16 beams at the same rate, with the same range separation and with the same integration times. The remaining time is shared between 'Special Programs' and 'Discretionary Time'. Special Programs acquire data from several radars, some of which are running special sounding modes, to take advantage of the global nature of the SuperDARN data set. Discretionary Time modes are operated on individual radars to allow more specific research by individual Principal Investigators (PIs). Data from the northern hemisphere SuperDARN radars are presented in Chapters 4 and 5.

3.3 Ground-based magnetometers

Ground-based magnetometers provide measurements of the Earth's magnetic field simultaneously in numerous locations. Data from the International Monitor for Auroral Geomagnetic Effects (IMAGE), 210° Magnetic Meridian (210 MM), Greenland, and Canadian Auroral Network for the Open Program Unified Study (CANOPUS) magnetometers are presented in later chapters.

The IMAGE (Viljanen and Häkkinen, 1997) magnetometer comprises 29 magnetometer stations covering 58° to 79° latitude (Figure 3.3). The instruments are triaxial fluxgate magnetometers with a sampling interval of 10 s. Data from the IMAGE magnetometer are presented in Chapter 4.

The 210 MM magnetometer network (Yumoto et al., 1996) has magnetometers located from -33° in the southern hemisphere to 71° in the northern hemisphere (Figure 3.4). This multi-nationally run magnetometer chain is run in conjunction with two other magnetometer chains at 190° and 250°. The sensors are fluxgate magnetometers with a sampling rate of 1 s. Data from the Tixie station are presented in Chapter 4.

The Greenland magnetometer network (Friis-Christensen et al., 1985) consists of 23 magnetometer stations located from 61° to 81° latitude on Greenland (Figure 3.5). The sensors are three-axes linear-core fluxgate magnetometers oriented along local magnetic north, local magnetic east and vertical down. All stations currently run at a 1 s sampling rate. Data from the Greenland magnetometer network are presented in Chapter 5.

The CANOPUS (Rostoker et al., 1995) magnetometer consists of a network of stations in west-central Canada (Figure 3.6), the Magnetometer and Riometer Array (MARIA) being a part of this. MARIA consists of thirteen stations distributed from 50° to 69° latitude, each of which has a three-component ring-core magnetometer. Data are sampled at the rate of 8 samples per second, the data presented being calculated as one sample every 5 s. Data from the Greenland magnetometer network are presented in Chapter 5.
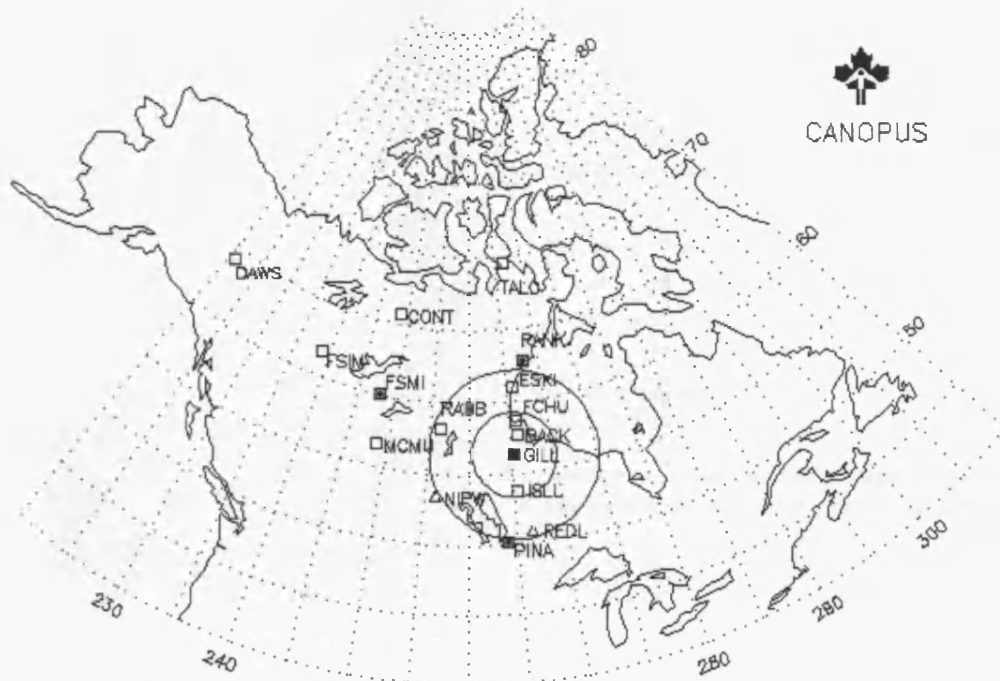
Figure 3.6: Location of the CANOPUS magnetometers (from http://www.dan.sp-agency.ca/www/welcome.htm).
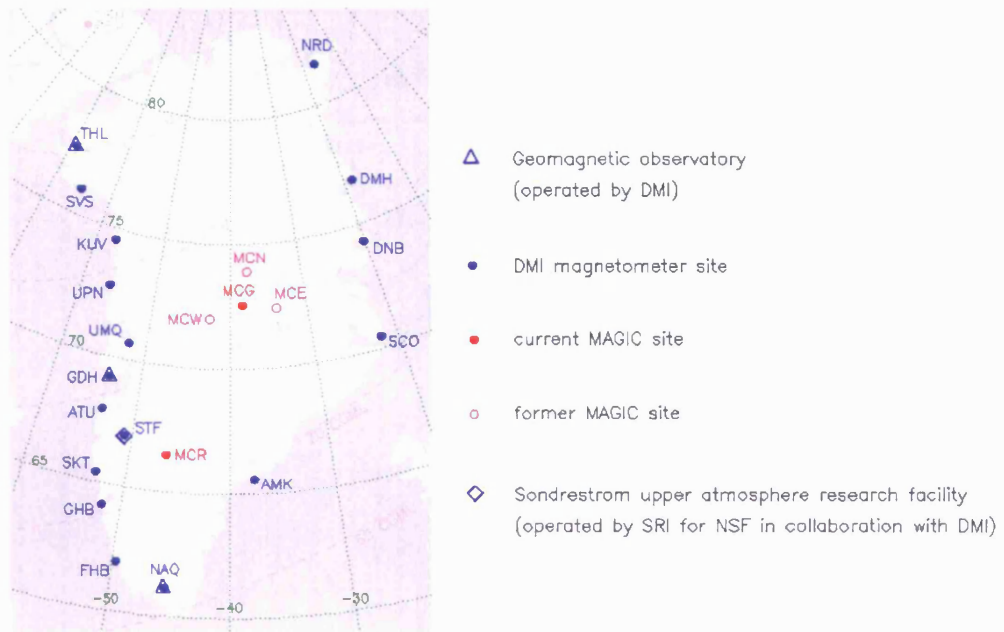
Figure 3.5: Location of the Greenland magnetometers (from http://web.dmi.dk/projects/chain/greenland.html).
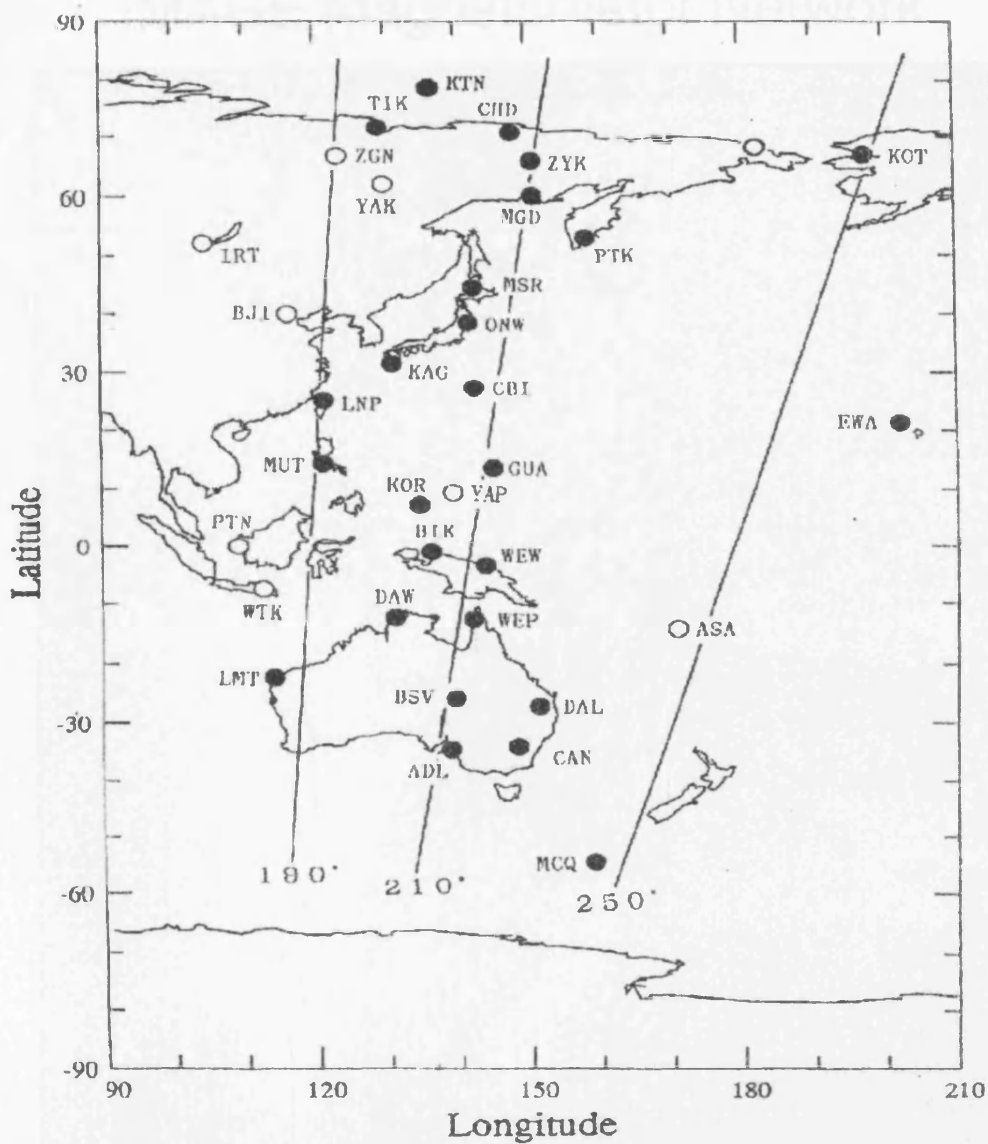
Fig. 1. Map showing the locations of the 190°, 210° and 250° MM chain stations in geographic coordinates (see Table 1).

Figure 3.4: Location of the 210 MM magnetometers (central line) (from http://stdb2.stelab.nagoya-u.ac.jp/mm210/index.html).

IMAGE Magnetometer Network
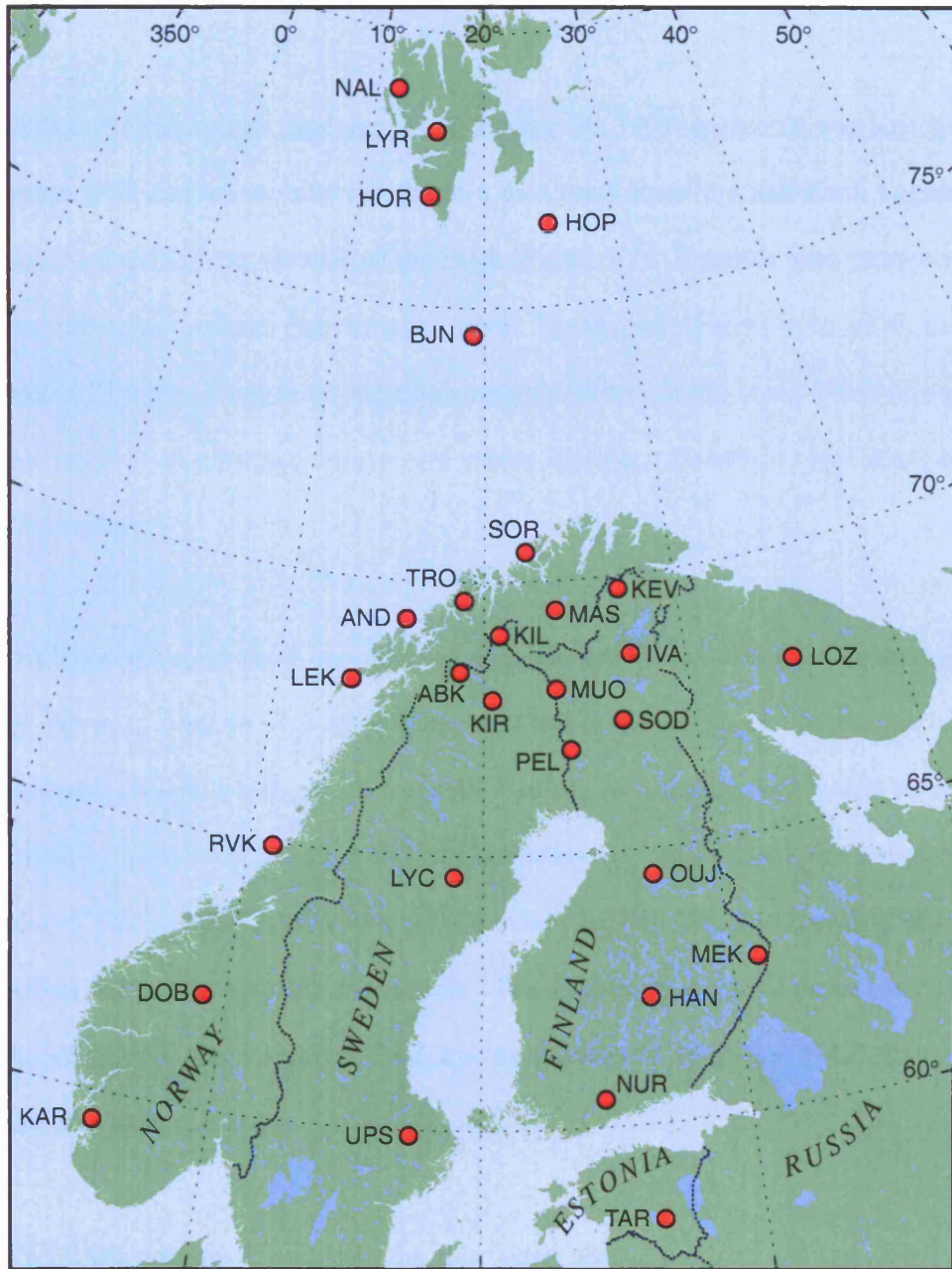
October 2004

Figure 3.3: Location of the IMAGE magnetometers (from http://www.ava.fmi.fi/image/index.html).

3.4 The Advanced Composition Explorer (ACE) spacecraft and instruments

The Advanced Composition Explorer (ACE; Stone et al., 1998) spacecraft was launched on 25 August 1997 and is currently located in a halo orbit about the Sun-Earth Lagrangian point L1, ~1.5 million km sunward of the Earth (Figure 3.7). It carries nine instruments in order to collect data samples from the solar wind. The two instruments from which data are presented in Chapters 4 and 5 are the magnetometer (MAG; Smith et al., 1998) instrument and the Solar Wind Electron, Proton and Alpha Monitor (SWEPAM; McComas et al., 1998) instrument.

The MAG instrument on ACE measures the direction and magnitude of the local magnetic field of the solar wind at ~1.5 million km upstream from the Earth. It consists of two magnetometer sensors which are twin triaxial fluxgate magnetometers situated on booms diametrically opposite to each other and an electronics box. This redundancy increases the reliability of the instrument and allows for instrument failure. The data sampling rate is up to 6 vectors per second from the two sensors. The three components of the magnetic field and the calculated total magnetic field are the parameters from the MAG instrument presented in Chapters 4 and 5.

The SWEPAM instrument measures the solar wind plasma electron and ion distribution functions as functions of direction and energy using one instrument for each. The SWEPAM ion instrument is a spherical section electrostatic analyzer aligned such that its fan-shaped field of view rotates about the spacecraft spin axis. The analyzer biases the energy-per-charge range of the incoming ions such that only a small fraction passes through
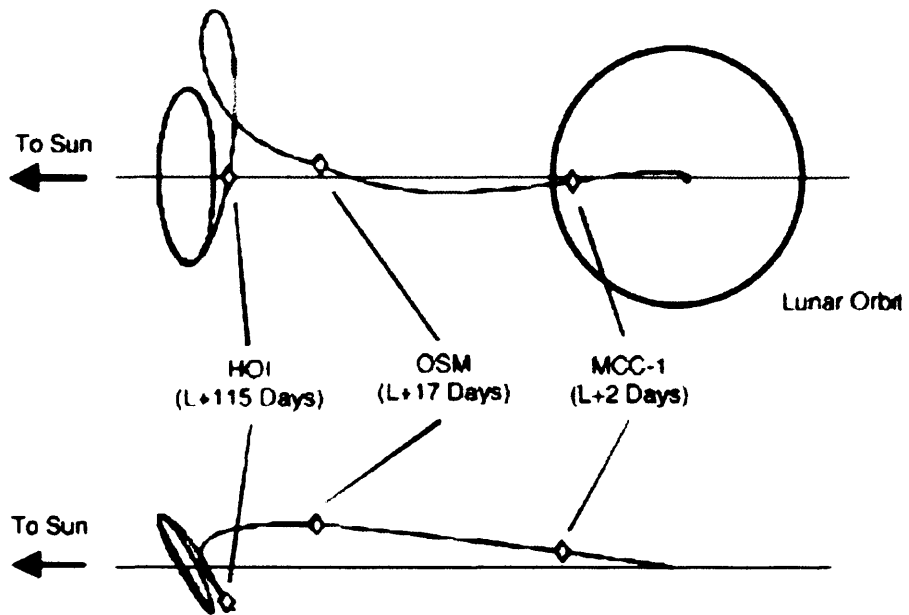
Figure 3.7: Schematic of ACE transfer trajectory out to L1 and subsequent halo orbit about

L1 (from Stone et al., 1998)

the analyzer to be detected by the sensor. A 65 ° field of view from the sun-pointing axis is achieved, with azimuthal field of views provided by the spacecraft spin. Its measurement resolution is every 64 s. The SWEPAM electron instrument is also based on a spherical section analyser. The analyzer biases the incoming electrons to select only those within a small range of energies, to be detected by the sensor. As ACE spins the fields of view of the instrument sweeps out over 95% of the whole sky, with data measured every 64 s. The dynamic pressure of the solar wind and its 3-component velocity are the parameters from the SWEPAM instrument presented in Chapter 5.

3.5 Near-Earth Spacecraft

Data from near-Earth spacecraft provide information about the magnetic field and plasma conditions around geosynchronous orbit. Those from which data are presented in later chapters are the Los Alamos National Laboratory (LANL) spacecraft, the Geostationary Operational Environmental Satellites' GOES-8 spacecraft and the Polar satellite.

The LANL (Belian et al., 1978) satellites are each located in geostationary orbit 6.6 R_E from Earth at 0 degrees latitude and at an arbitrarily chosen fixed longitude. The electron and ion sensors on the satellites were the Charged Particle Analyzers (CPA) until 1987 after which the Synchronous Orbit Particle Analyzers (SOPA; Belian et al., 1992) instruments took over, although both instruments are still providing data. The data presented in Chapters 4 and 5 are from the SOPA instrument, which collects 64 samples per spin period (~10 s) from three solid state detector telescopes which point in different directions. These have front and back detectors allowing detection of the incoming ions and electrons.

The GOES spacecraft orbit the Earth at geosynchronous orbit, Magnetic field data from the GOES 8 spacecraft (Nagai, 1982) are presented in Chapter 5. This spacecraft was launched on 13 April 1994 and is now decommissioned.

The Polar satellite was launched on 24 February 1996 into a highly elliptical orbit with a period of ~17 hours. Its orbit is at 86 ° inclination allowing it to view the Earth's poles. Data from the Comprehensive Energetic Particle and Pitch Angle Distribution (CEPPAD; Blake et al., 1995) instrument, which measures electrons over the energy range from ~ 25 to 400 keV, are presented in Chapter 4.

Chapter 4

A joint Cluster and ground-based instruments study of two magnetospheric substorm events on 1st September 2002

In this chapter we present observations in the tail and ionosphere from an interval in which two substorm expansion phases occur. From these observations we discuss the relative merits of the two main substorm onset models described in Chapter 2.

4.1. Instruments

Figure 4.1 presents the position of the footprints of the Cluster 1 (Rumba, solid orange line) and Polar spacecraft (dashed green line) in a geographic coordinate system on 1st September 2002 between 1800 and 2400 UT. Also indicated are the fields of view of some of the northern hemisphere SuperDARN radars (Greenwald et al., 1995) with beams 2, 8 and 14 marked for the Hankasalmi (Finland) radar. The locations of IMAGE ground magnetometer network stations (Viljanen and Häkkinen, 1997) are also indicated in Figure 4.1 as small black crosses. The fields of view of two of the SuperDARN radars, located at Hankasalmi in Finland and Þykkvibær in Iceland, partly overlap this magnetometer network. The location of the Tixie station of the 210 MM (210 degrees magnetic meridian) magnetometer network, whose data are also employed, is out of the view of the plot, at 65.67 ° geomagnetic latitude and 196.88 ° geomagnetic longitude. The times labelled with
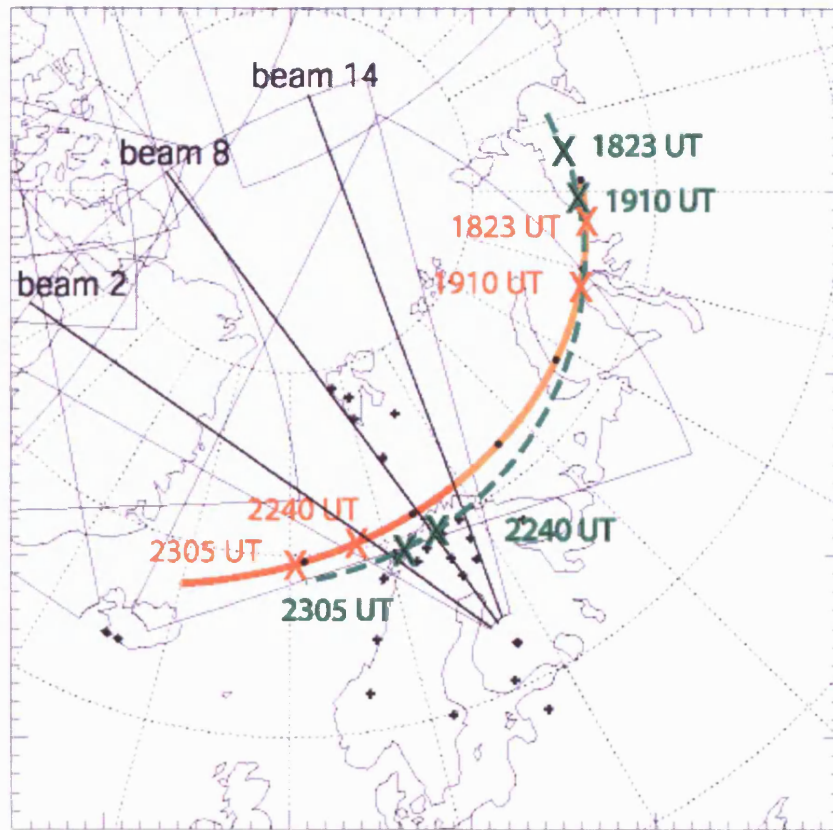
Figure 4.1: Cluster 1 (Rumba) footprint (solid orange line) and Polar footprint (dashed green line) mapped on to SuperDARN fields-of-view, with IMAGE magnetometer stations (black crosses). Times of interest are marked with orange crosses for the Cluster footprint and green crosses for the Polar footprint.

orange crosses on the Cluster footprint and green crosses on the Polar footprint correspond to events discussed in this paper. The Cluster footprint comes into conjunction with the fields of view of the radars from around 1900 UT, starting with the Þykkvibær (Iceland East) radar, while the Polar footprint comes into conjunction from 2000 UT. Figure 4.2 shows the position of the four Cluster spacecraft (true separations) and the Polar spacecraft during this interval in the GSM xz, xy and yz planes. The dotted lines show the model magnetic field lines using the Tsyganenko 1996 model (Tsyganenko and Stern, 1996) while the solid lines show the Cluster spacecraft paths, and the dashed lines show the Polar spacecraft's path. The Cluster spacecraft are all above the centre of the plasma sheet and in the post-midnight sector, and at -16 R_E downtail at 1800 UT (having later moved to -18 R_E at 2400 UT). Cluster 3 (Samba, shown in yellow) is closest to the current sheet, Cluster 4 (Tango, red) is furthest down the magnetotail, and Cluster 2 (Salsa, green) is closest to midnight (the y=0 axis). The instruments used from the Cluster spacecraft in this study include the Fluxgate Magnetometer (FGM; Balogh et al., 1997), the Plasma Electron and Current Experiment (PEACE; Johnstone et al., 1997), the Cluster Ion Experiment (CIS; Rème et al., 1997), and the Research with Adaptive Particle Imaging Detectors instrument (RAPID; Wilken et al., 1997). The Polar spacecraft (denoted by a black cross) was in the magnetotail close to the equatorial plane, in the post-midnight sector at a distance of -8 R_E downtail at 1800 UT (and later -9 R_E at 2400 UT). Particle data from the Comprehensive Energetic Particle and Pitch Angle Distribution (CEPPAD; Blake et al., 1995) instrument on Polar are used here.
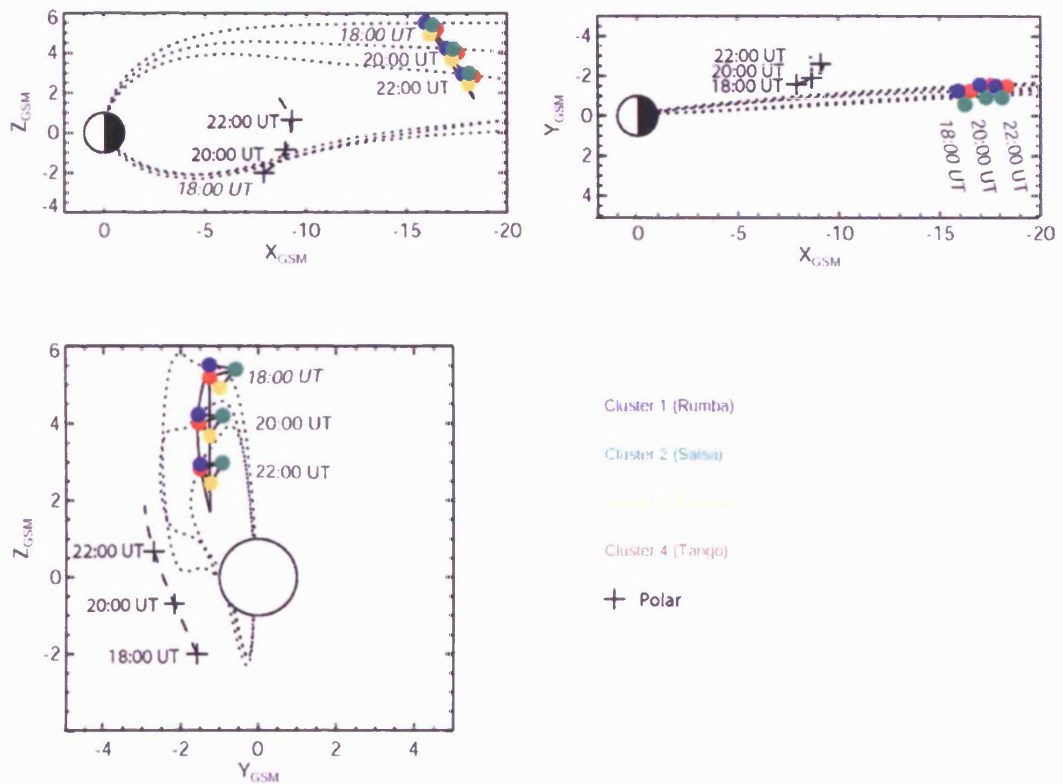
Figure 4.2: Orientation of the four Cluster spacecraft and the Polar spacecraft during the 1st September 2002 interval (1800 to 2400 UT) in geocentric solar magnetospheric (GSM) coordinates in the xz, xy and yz planes. Blue represents Cluster 1 (Rumba), green Cluster 2 (Salsa), yellow Cluster 3 (Samba) red Cluster 4 (Tango) and a black cross represents the Polar spacecraft. Solid lines show the Cluster spacecraft paths and dashed lines show the Polar spacecraft's path. Dotted lines depict the model magnetic field.

4.2. Data description

4.2.1 IMAGE and 210 MM magnetometer arrays

In order to provide a context for the Cluster observations and determine timings for the relevant events occurring during the interval, IMAGE ground magnetometer data are shown in Figure 4.3. Plots of the x (north-south) component of the magnetic field at selected IMAGE stations and the corresponding filtered data (20 to 200 s) at one station, Tartu (tar), are shown for the 1800 to 2400 UT interval. The latter provides information on the presence of Pi2 wave activity. Substorm expansion phase onset is accompanied by Pi2 pulsations in the ground magnetometer data, which are irregular, damped ULF waves with a period of approximately 40 to 150 seconds. The Pi2 pulsations are related to the SCW that forms during a magnetospheric substorm (e.g Lester et al, 1983), and thus the onset of Pi2 pulsations may be taken as a proxy for substorm onset (e.g. Rostoker at al., 1980).

The first time of note is 1823 UT, when Pi2 pulsation onset occurs at all stations, although only one station, tar, is shown. This is accompanied by a slight increase in the x component of up to a few tens of nanotesla (nT) at higher latitudes. This indicates either a pseudobreakup or a full substorm occurring to the east of the stations. At 2240 UT and 2256 UT there are pseudobreakups at the lower latitude stations, as evidenced by Pi2 pulsations in all components but no major electrojet signature at the higher latitudes. At 2305 UT a full substorm expansion phase onset occurs at the Sodankylä (sod) and Pello (pel) stations, shortly followed by the Kilpisjärvi (kil) and Ivalo (iva) stations which are at a slightly higher latitude (and co-incident with the Polar spacecraft's path). Pi2 pulsations are detected at all latitudes in all components. Magnetograms at higher latitudes show a

40
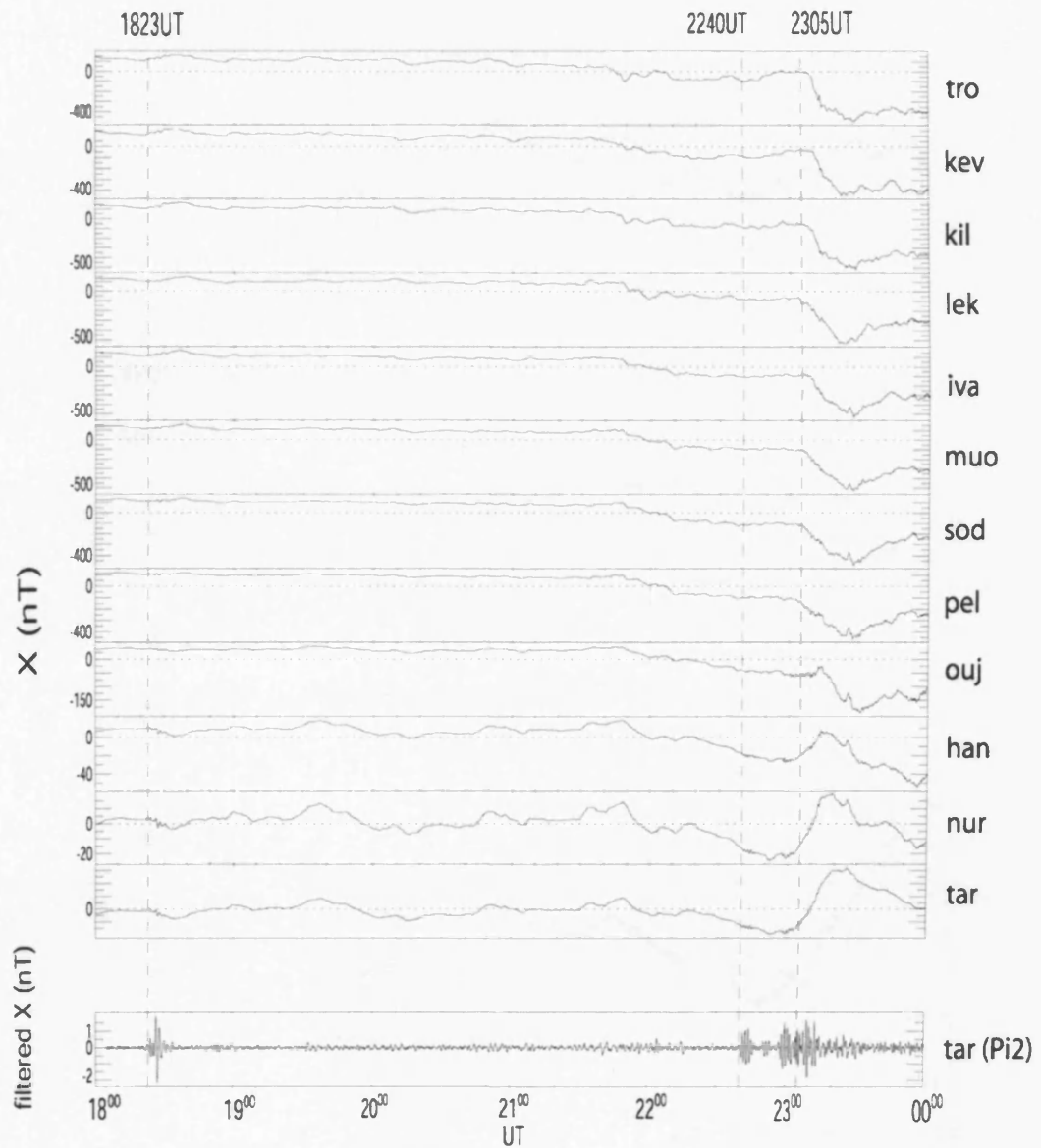
Figure 4.3: Top panels: x component of magnetic fields at selected IMAGE magnetometer stations; bottom panel: x component filtered magnetometer data from one example station in the period band 20-200 s.

210 MM Magnetic Field Data: Tixie station
1st September 2002
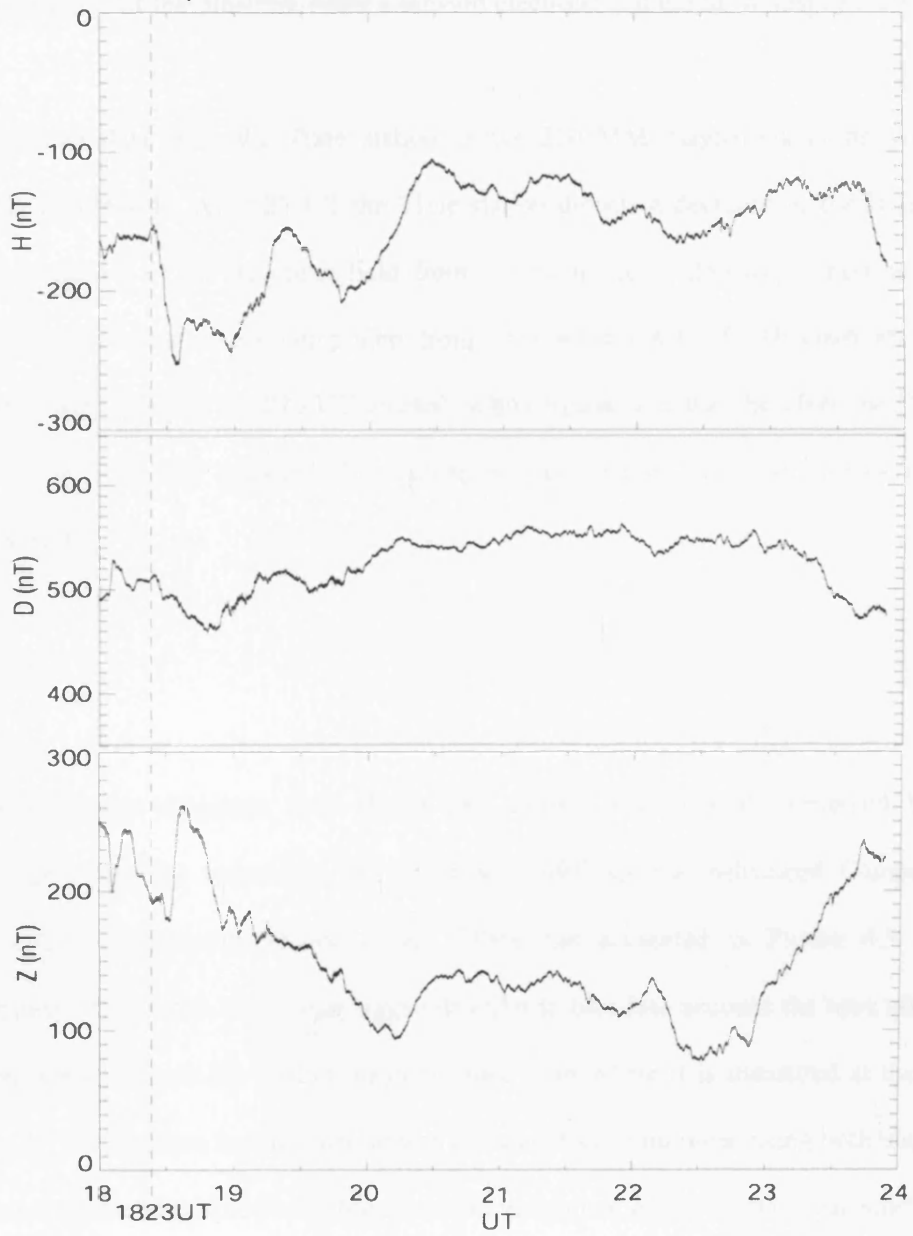
Figure 4.4: 210 MM magnetometer data from the Tixie station in H, D and Z components, from 1800 to 2400 UT. Substorm onset at 1823 UT indicated by a vertical dashed line.

decrease in the x component while the lower latitude stations show an increase at substorm onset, signatures of the substorm onset westward electrojet and the SCW respectively.

Magnetometer data from the Tixie station of the 210 MM magnetometer network are shown in Figure 4.4. At 1823 UT the Tixie station detects a decrease in the H (north - south) component of the magnetic field from ~ -150 nT to ~ -250 nT. There is also a decrease in the D (east - west) component from ~ 510 nT to ~ 460 nT. This indicates that a substorm onset occurred at 1823 UT located in this region, and that therefore the IMAGE magnetometer network detected this substorm onset rather than the signature of a pseudobreakup.

4.2.2 ACE

The interplanetary magnetic field (IMF) data during this interval, measured by the magnetometer (MAG) instrument (Smith et al., 1998) on the Advanced Composition Explorer (ACE) spacecraft (Stone et al., 1998), are presented in Figure 4.5 (GSM coordinates). These data have been lagged in order to take into account the time taken by the solar wind to reach the Earth's magnetopause from where it is measured at the ACE spacecraft. The lag time for this interval was calculated as 75 minutes, using both magnetic field data from the Magnetic Fields Measurement instrument on the Geotail spacecraft (data not shown) and the technique of Khan and Cowley (1999), from solar wind velocity and density data from the Solar Wind Electron, Proton and Alpha Monitor (SWEPAM) instrument (McComas et al., 1998) on ACE. In the discussions of the ACE data we quote all times in terms of the lagged time.

Advanced Composition Explorer (ACE)
MAG DATA
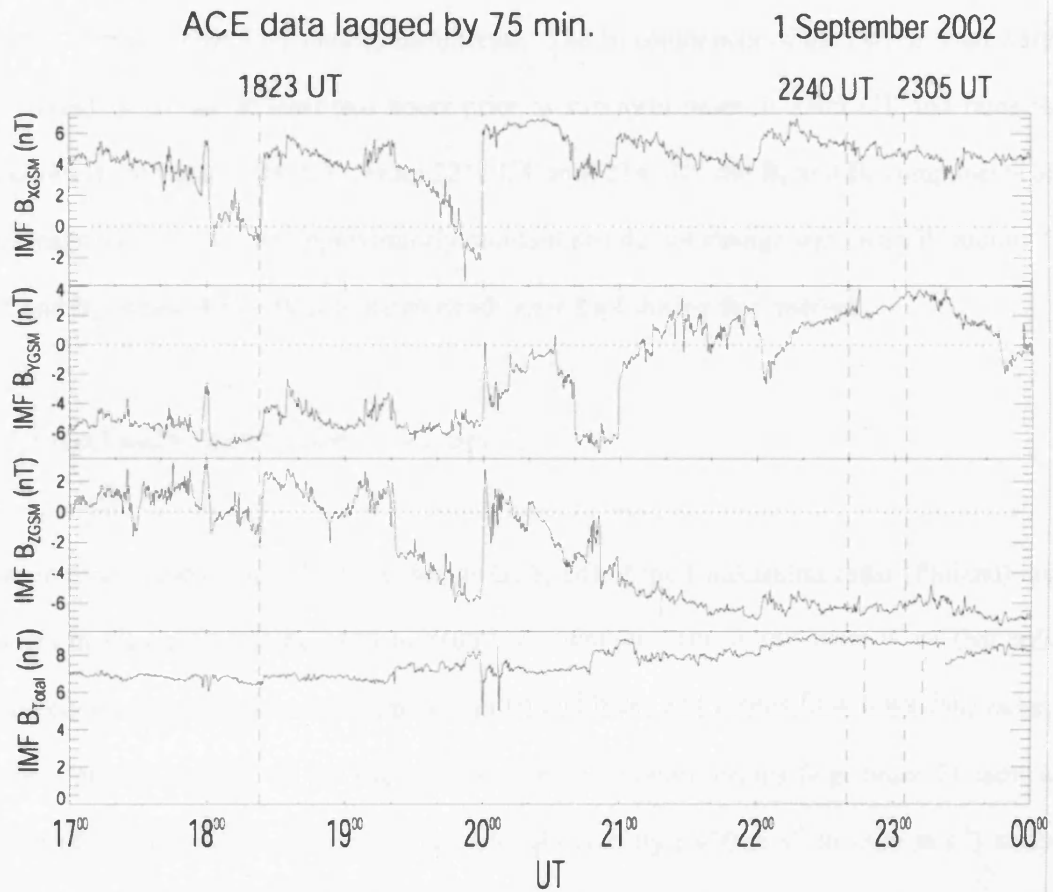
Figure 4.5: ACE MAG data lagged by 75 minutes (in GSM coordinates). Expansion phase onsets at 1823 UT and 2305 UT and a pseudobreakup at 2240 UT are indicated by vertical dashed lines.

Around the first interval at 1823 UT the (lagged) B_x component of the IMF turns positive. B_y is negative and approximately constant at -6 nT, and B_z turns northwards. B_{total} remained steady near 7 nT during this interval. The B_z component of the IMF is southward at around -6 nT for at least two hours prior to substorm onset at 2305 UT and remains southward until after 2400 UT. From 2215 UT until 2345 UT the B_x and B_y components of the magnetic field remain approximately constant and do not change sign, with B_x around 5 nT and B_y around 4 nT. B_{total} remains steady near 8 nT during this interval.

4.2.3 Hankasalmi and Þykkvibær radars

Range-time-velocity plots for three beams (2, 8, 14) of the Hankasalmi radar (Finland) are shown in Figure 4.6 for the 1800 to 2400 UT interval. The colour scale is such that reds and yellows denote flow away from the radar and blues and greens flow towards the radar; grey is ground scatter. In the Hankasalmi data, the western beams (e.g. beam 2) show a series of intensifications of Doppler line-of-sight velocity (-400 m s^{-1} to -800 m s^{-1}) away from the radar soon after 1823 UT, beginning at 1833 UT, while eastern beams (e.g. beam 14) show intensification of velocity towards the radar from 1830 UT (velocities 400 m s^{-1} to 600 m s^{-1}). These are seen in all beams and are similar to the signatures seen by Sandholt et al. (2002) who related them to poleward boundary intensifications (Lyons et al., 1999). The directions of these line-of-sight velocities are consistent with westward ion flow. The direction of flow observed by the radar is subsequently reversed at later times; the change of direction occurs at 1930 UT in the central beams and from 2010 UT in the western and eastern beams, indicating that the flows here now become eastward. This is due to the rotation of the Earth, and hence the radars, under the ionospheric flows rather than an actual change in the flow pattern. The outer beams also show velocity

42
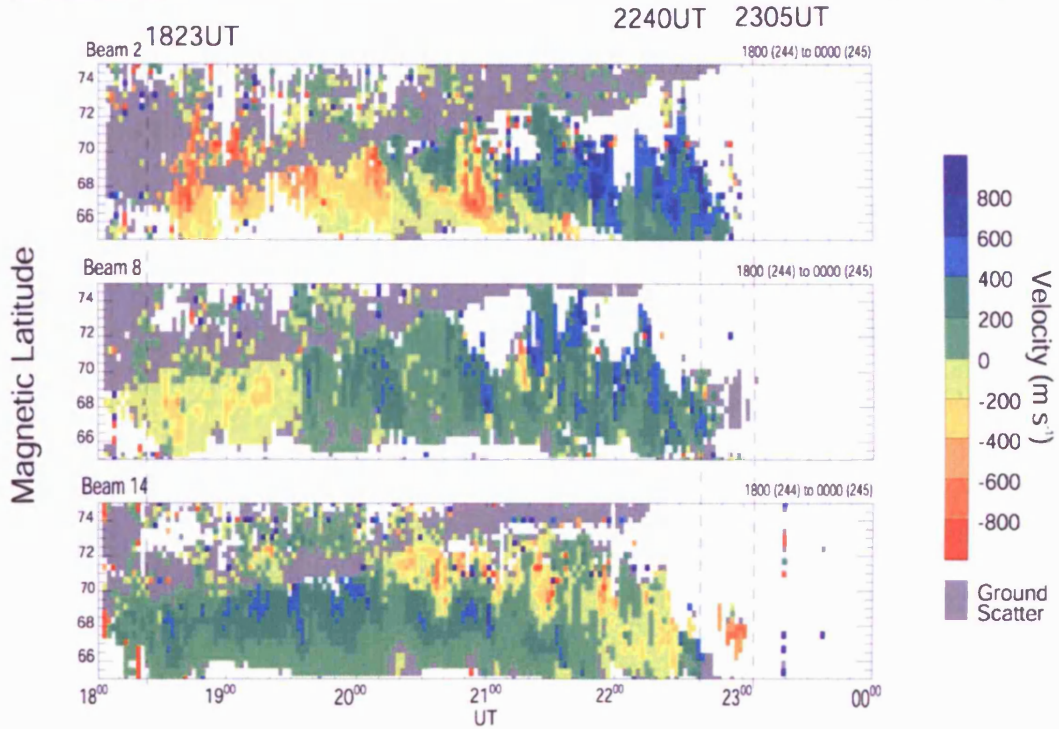
Figure 4.6: Range, time and intensity plots for the velocity at three different beams (2, 8 and 14) of the Hankasalmi (Finland) radar during the 1800 to 2400 UT interval. Vertical dashed lines represent times of pseudobreakup at 2240 UT and expansion phase onsets at 1823 UT and 2305 UT.

intensifications after 2010 UT that move equatorward over time; they are highly variable and maintained until 2240 UT. These are signatures of bursty bulk flows (BBFs) in the ionosphere, and are the subject of further work (see Nakamura et al., 2005). After 2240 UT there is a significant reduction in scatter, and from 2250 UT scatter is lost completely, first from the eastern beams from 2240 UT and then from the western beams.

The Þykkvibær radar (Iceland east) data (not shown) have intensifications towards the central beams of the radar from 1845 UT onwards. Exceptionally strong flows toward the radar (600 m s^{-1} to 800 m s^{-1}) are seen in beams 6 to 12 from 1930 UT onwards. At 2240 UT there is some intensification of flow toward the radar on the northern beams 0 to 7 (velocities 400 m s^{-1} to 600 m s^{-1}). This intensification persists until 2314 UT when it is abruptly lost. After this time much of the scatter is lost such that only ground scatter and some low-velocity scatter remains.

4.2.4 SuperDARN

The map potential analysis technique (Ruohoniemi and Baker, 1998) for the SuperDARN data was used to map line-of-sight velocity measurements from the northern hemisphere radars (Kodiak, Prince George, King Salmon, Þykkvibær, Hankasalmi, Goose Bay, Saskatoon, Kapuskasing and Stokkseyri) onto a global grid to provide large-scale global convection maps for the interval of interest. SuperDARN map potential plots presented here (Figures 4.7, 4.8, 4.9 and 4.10) show pre-midnight and post-midnight sector sections of large-scale convection maps and so-called true vectors (see Ruohoniemi and Baker, 1998), derived from line-of-sight data from the SuperDARN radars for times of interest near the first (Figures 4.7 and 4.8) and second (Figures 4.9 and 4.10) of the substorm

SUPERDARN PARAMETER PLOT   1 Sep 2002 [244]
1822UT, 1824UT, 1826UT (pre-midnight sector)
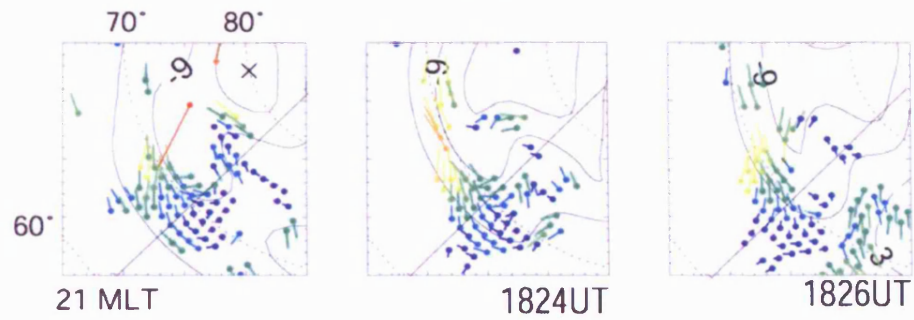
Figure 4.7: SuperDARN map potential plots at two-minute intervals with the true vectors superposed at 1822, 1824 and 1826UT on 1st September 2002.
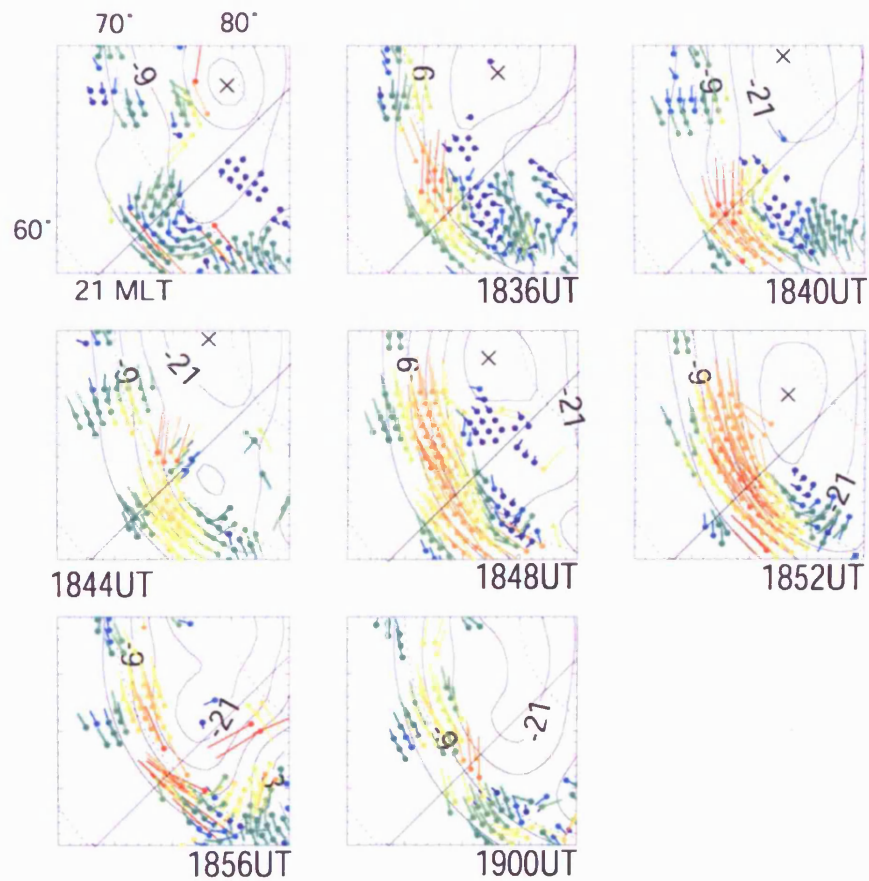
Figure 4.8: SuperDARN map potential plots at four-minute intervals with the true vectors superposed from 1832 until 1900UT on 1st September 2002.
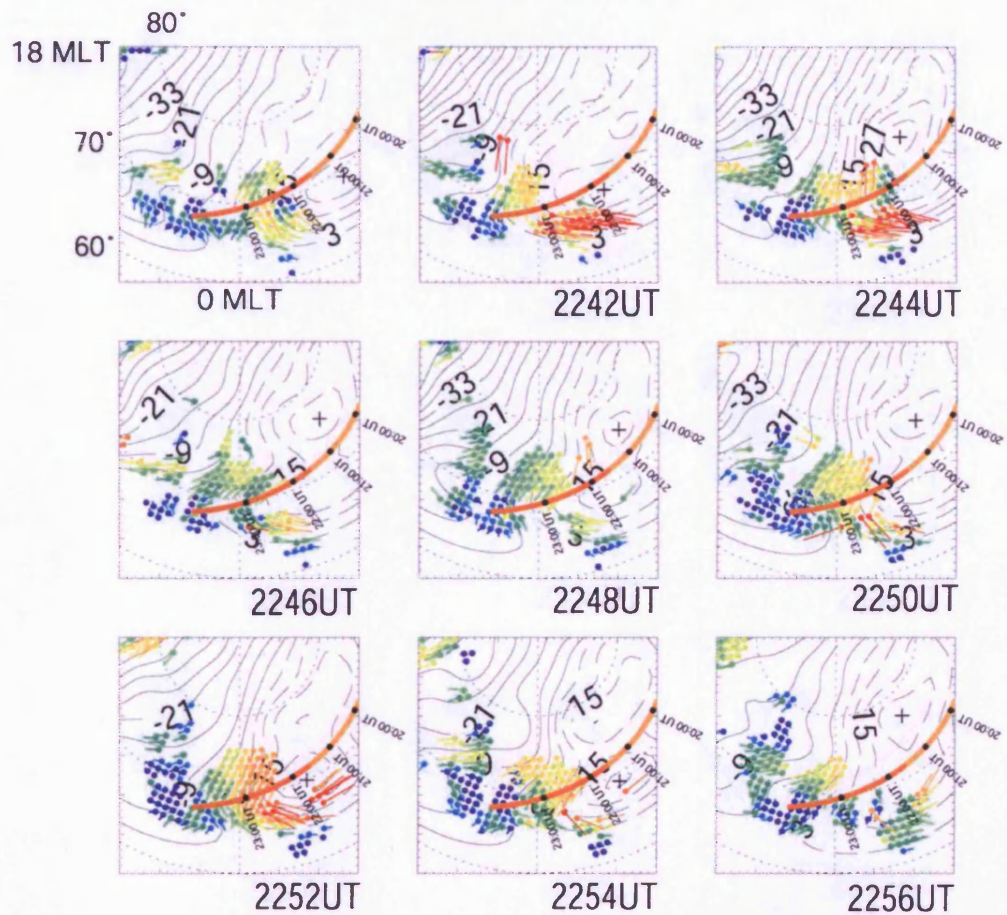
Figure 4.9: SuperDARN map potential plots at two-minute intervals with the true vectors superposed from 2240 until 2256UT on 1st September 2002 and with Cluster 1 footprint also superposed.

Figure 4.10: SuperDARN map potential plots at two-minute intervals with the true vectors superposed from 2258 until 2314UT on 1st September 2002 and with Cluster 1 footprint also superposed.

expansion phase onsets. The Cluster footprint is shown where it is within the map limits (Figure 4.9 and Figure 4.10 only). Dotted black lines depict constant latitude and MLT, while dashed and solid black lines depict contours of potential. The true vectors shown are colour-coded by magnitude such that slower velocities are blue and faster velocities are red.

The map potential plots in Figure 4.7 show that at 1824 UT (21 MLT, 60° to 80° section of plot shown) there is an intensification of the velocity in the 20 MLT, 65° to 70° latitude region, to a velocity of 800 m s^{-1}. From 1832 UT until 1900 UT (Figure 4.8) there are strong westward flows in the pre-midnight sector (21 MLT, 60° to 80° section of plot shown). Figure 4.9 (00 MLT, 60° to 80° section of plot shown) shows enhancements in flows from 2240 UT until 2256 UT in the midnight sector (00 MLT), just equatorward of the estimated footprint of the Cluster spacecraft at that same time. In particular there are intensifications of the velocity at 2242 and 2252 UT. These intensifications occur at 65° to 75° latitude, and reach values of 1000 m s^{-1}. From 2258 UT strong, antisunward flows continue in the 00 MLT region as can be seen in Figure 4.10, centred around 65° to 75° latitude, to a velocity of around 1000 m s^{-1} (00 MLT, 60° to 80° section of plot shown). This is maintained until 2312 UT to a velocity of 800 m s^{-1}, after which the scatter is lost. Particularly strong flows occur at 2304 UT.

4.2.5 Cluster FGM

Figure 4.11 presents the Cluster FGM data for the 1800 to 2400 UT interval for the GSM B_x, B_y, B_z components and B_{total} at Cluster 1 (Rumba). In the ~20 minutes prior to the first substorm expansion phase at 1823 UT, the field is dominated by the x component, with

44

CLUSTER
Fluxgate Magnetometer (FGM)

CLUSTER 1 (Rumba)
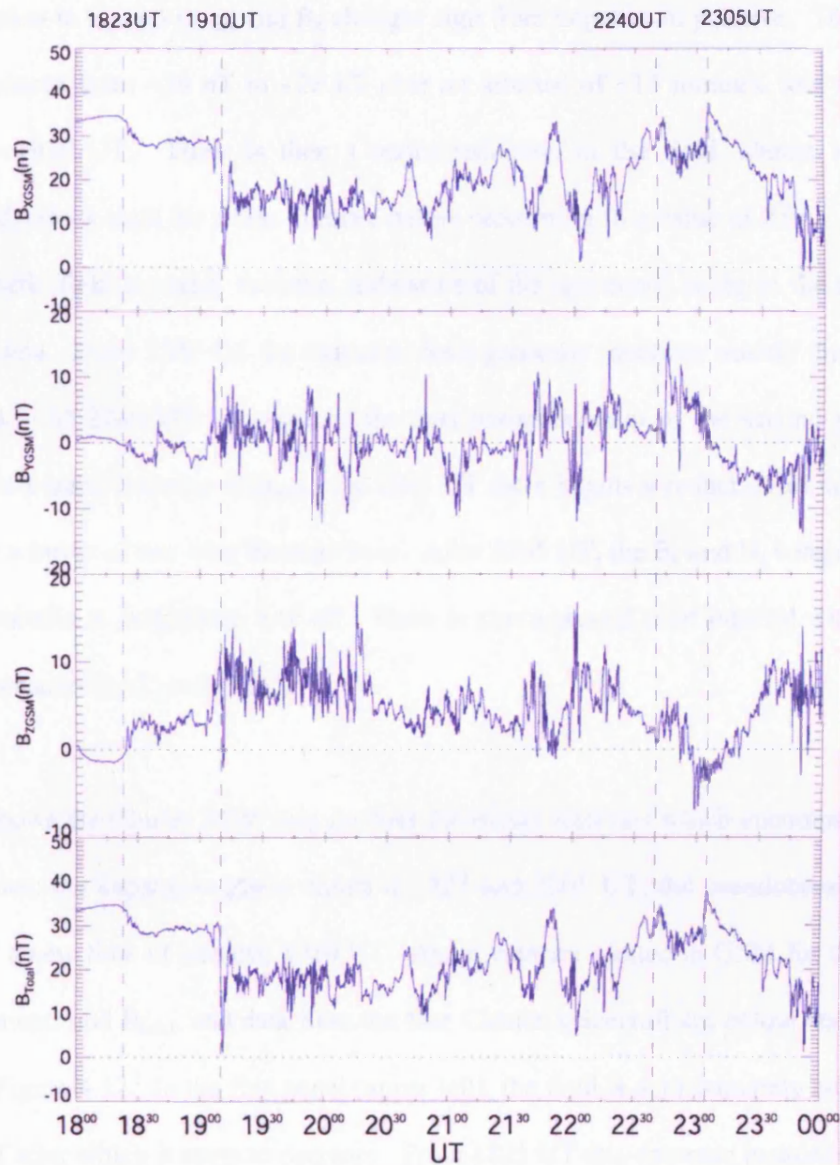
Figure 4.11: Cluster FGM data for 1st September 2002 (1800 to 2400 UT interval). The Bx, By, Bz components and Btotal in GSM coordinates are shown for the Cluster 1 spacecraft (Rumba).

both y and z components small, with values ~1 nT, although we note that the z component is negative. The x component and hence total field both increase up to the time of expansion phase onset. Following the substorm expansion phase onset at 1823 UT, there is a small reduction in B_x and B_{total}, and B_z changes sign from negative to positive. The field magnitude reduces from ~34 nT to ~28 nT over an interval of ~15 minutes, and is then steady until ~1910 UT. There is then a major reduction in the field, almost to zero magnetic field, which lasts for a few minutes before recovering to a value of 25 nT. After this the magnetic field is highly variable, indicative of the spacecraft being in the plasma sheet at this time. From 2200 UT the magnetic field generally increases mainly due to an increase in B_x. At 2240 UT, the time of the first pseudobreakup in the second growth phase, there is a small increase in B_{total}. At 2305 UT there begins a reduction in the field magnitude by a factor of two over the next hour. After 2345 UT, the B_x and B_z components become comparable in magnitude, ~10 nT. There is also a second brief interval when the total field approaches 0 nT, at 2353 UT.

Figure 4.12 shows the Cluster FGM data for four 20 minute intervals which encompass the times of interest: the expansion phase onsets at 1823 and 2305 UT, the pseudobreakup at 2240 UT and a new time of interest, 1910 UT. Again data are plotted in GSM for the B_x, B_y, B_z components and B_{total}, and data from the four Cluster spacecraft are colour coded as indicated on Figure 4.12. In the first panel (upper left), the field is approximately constant until 1821 UT after which it starts to decrease. From 1825 UT this decrease is quicker and occurs at all spacecraft simultaneously, indicating a temporal, rather than a spatial, change in the magnetic field at the Cluster spacecraft at that time. There is also evidence of wave activity initiated at the onset, as Pi2 waves are present from this time.
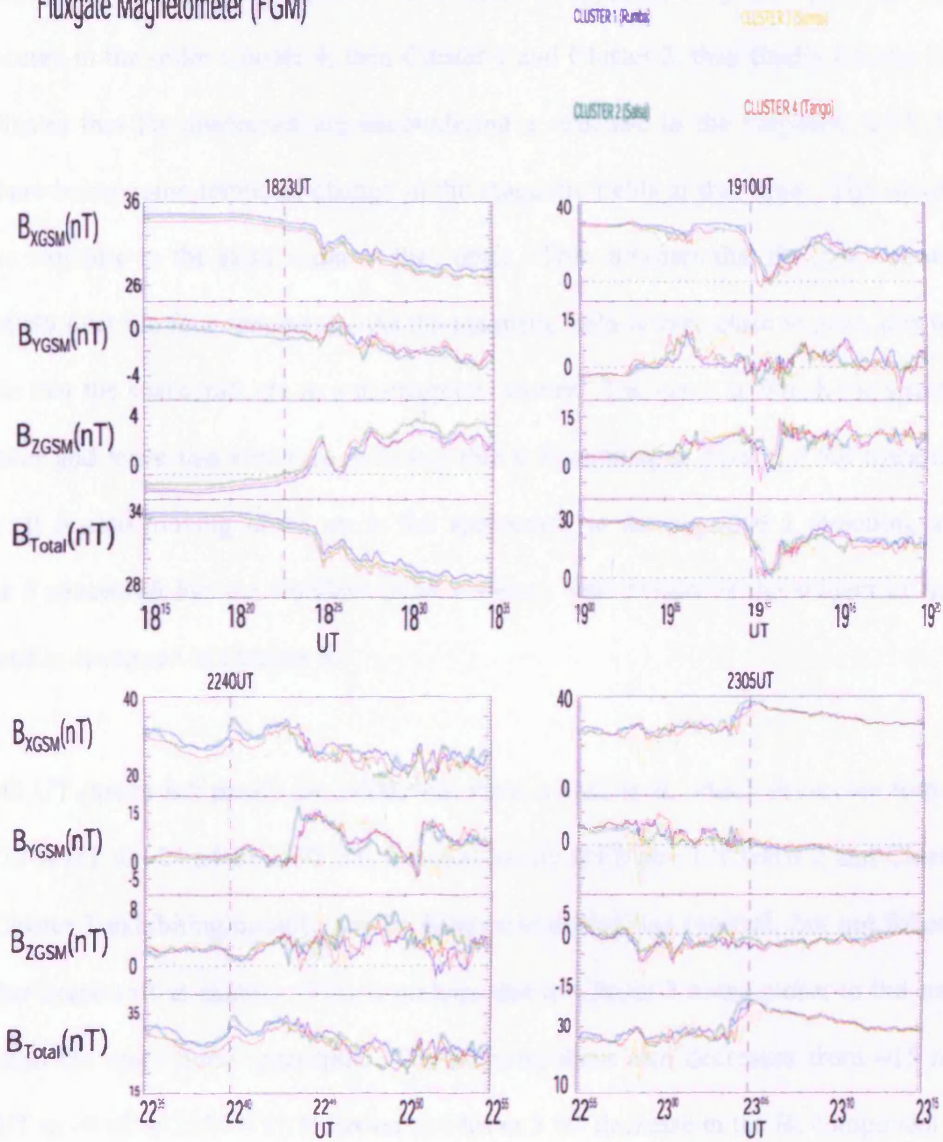
Figure 4.12: Cluster FGM data for 1st September 2002 in the Bx, By, Bz and Btotal GSM coordinates for intervals centred on 1823, 1910, 2240 and 2305UT. Cluster 1 (Rumba) is shown in blue, Cluster 2 (Salsa) in green, Cluster 3 (Samba) in yellow and Cluster 4 (Tango) in red.

At 1910 UT (upper right panel) the FGM data show a sudden and brief excursion whereby all components briefly approach 0 nT, then return to approximately their previous values. This occurs in the order Cluster 4, then Cluster 1 and Cluster 2, then finally Cluster 3, and so indicates that the spacecraft are encountering a structure in the magnetic field, rather than there being some temporal change in the magnetic fields at that time. The spacecraft exit the structure in the same order as they enter. This indicates that the structure moves completely over the four spacecraft. As the magnetic field is very close to zero, this would indicate that the spacecraft are in a diamagnetic cavity. The order in which the spacecraft encounter and leave this structure indicates that it is coming in from the tail towards the Earth. It is also moving down on to the spacecraft, in the negative z direction, as the Cluster 3 spacecraft has the smallest GSM z value. This feature is the subject of further work and is discussed in Chapter 6.

At 2240 UT (lower left panel) the FGM data show a peak in B_x which decreases from ~34 nT at 2244 UT to ~24 nT at 2250 UT, simultaneously at Cluster 1, Cluster 2 and Cluster 4, with Cluster 3 exhibiting broadly similar behaviour during this interval, but not following the other spacecraft as exactly. This is perhaps due to Cluster 3 being closer to the current sheet than the other three spacecraft. The B_y component also decreases from ~15 nT at 2244 UT to ~0 nT at 2250 UT. However at Cluster 3 the decrease in the B_y component lags that at the other spacecraft by a few minutes.

At 2305 UT (lower right panel) the B_x component of the magnetic field reaches a peak at around 38 nT then decreases at all spacecraft simultaneously. Again, Cluster 3 shows slightly different variations but in general the agreement between the other spacecraft is very close. The B_y component begins a gradual decrease from ~0 nT at this time, while the

46

B_z component begins a gradual increase from ~ –4 nT. B_{total} begins to decrease from ~38 nT, following the dominant B_x component, and decreases by a factor of two over the next hour. This reduction is seen at all spacecraft and so is a feature that occurs over a scale size larger than the spacecraft separation. In all components there are fewer high-frequency oscillations during this time, indicating that the spacecraft may have exited the plasma sheet and re-entered the lobe. This is now corroborated in the Cluster plasma data from CIS, PEACE and RAPID.

4.2.6 Cluster plasma data

The top six panels of Figure 4.13 show the CIS ion density and velocity data from three spacecraft, Cluster 1, Cluster 3 and Cluster 4 for this interval. Note that the CIS instrument on Cluster 2 was not operational at the time. Prior to 1903 UT (indicated by the second vertical dashed black line on plot) all three spacecraft measure low ion densities of ~0.01 cm^{-3}. At 1903 UT there is an increase in the low-energy ion densities at all spacecraft to ~0.1 cm^{-3} at Cluster 1 and Cluster 3, and to ~1.0 cm^{-3} at Cluster 4. This is accompanied by a sharp increase in the v_x component of the velocity from ~0 km s^{-1} to ~1000 km s^{-1}, with some fluctuations. This indicates bursty flow towards Earth which continues until 1915 UT. At 2305 UT there is a sharp decrease in the density at all spacecraft, returning to ~0.01 cm^{-3}. These data indicate that the spacecraft are in the plasma sheet from 1903 UT until the second substorm onset at 2305 UT, consistent with the FGM data, and in the lobe before 1903 UT and after 2305 UT.

The bottom panel of Figure 4.13 shows the PEACE electron density data from Cluster 4 for this interval. Data from this spacecraft are shown as the ASPOC (Riedler et al., 1997)

47
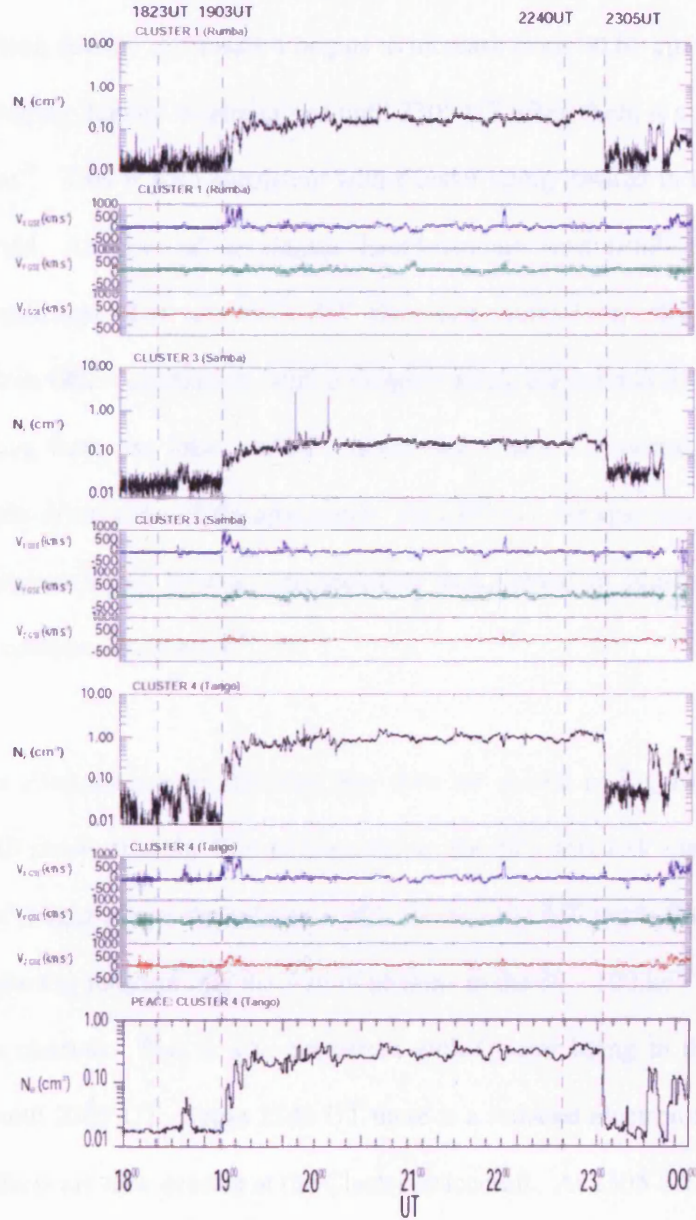
Figure 4.13: Top six panels: Cluster CIS density and velocity data from the three spacecraft for 1st September 2002 (1800 to 2400 UT interval). Bottom panel: Cluster PEACE density data from Cluster 4 for the same interval.

spacecraft potential control device is switched on in order to avoid interference by photoelectrons, thereby making the density data more reliable. At around 1903 UT the low-energy electron density at Cluster 4 begins to increase from ~0.01 cm^{-3} to ~0.1 cm^{-3} at 1910 UT. This higher density is maintained until 2305 UT when there is a sudden decrease back to ~0.01 cm^{-3}. This is also consistent with Cluster being located in the plasma sheet during this interval. Analysis of the plasma sheet boundary layer (PSBL) crossings using PEACE data indicates that at 1903 UT the unit normal of the boundary was (0.01,-0.56,0.83) in GSE coordinates, with a velocity along the normal of 30 km s^{-1}. This was for a crossing from the lobe into the plasma sheet which occurred in the direction expected given the orientation of the spacecraft. At 2305 UT the spacecraft re-entered the lobe from the plasma sheet, with a corresponding unit normal of (0.02,-0.34,-0.94) and normal velocity component 38 km s^{-1}.

The RAPID-IES omni-directional electron flux data are shown in Figure 4.14 (first four panels). The IES shows that the flux of electrons in the 40 - 400 keV range increases by several orders of magnitude in the interval 1903 UT to 2305 UT (with fluctuations). The IIMS data (not shown) indicate that the flux of protons in the 30 - 100 keV range increases during the same interval. This is also consistent with Cluster being in the plasma sheet from 1903 UT until 2305 UT. From 2240 UT there is a reduced electron flux, suggesting growth phase effects are now present at the Cluster spacecraft. At 2305 UT there is a sharp decrease at all energy levels at all four spacecraft as they exit the plasma sheet into the lobe.

Plasma beta is the ratio of the plasma pressure to the magnetic pressure, $2\mu_0 nkT_\perp/B^2$. It was calculated using Cluster CIS and FGM data and is presented in Figure 4.15. Low values of plasma beta indicate that the spacecraft are located in the lobe whilst values above
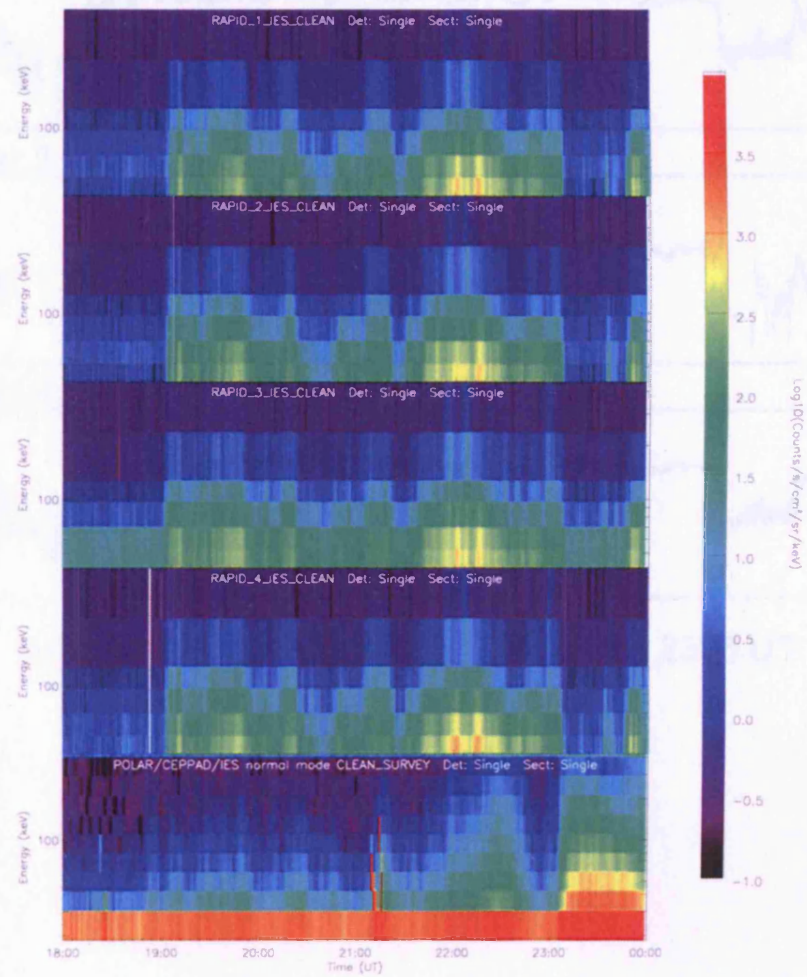
Figure 4.14: First four panels: Cluster RAPID IES data for 1st September 2002 (1800 to 2400 UT interval). Bottom panel: Polar CEPPAD IES data for the same interval.
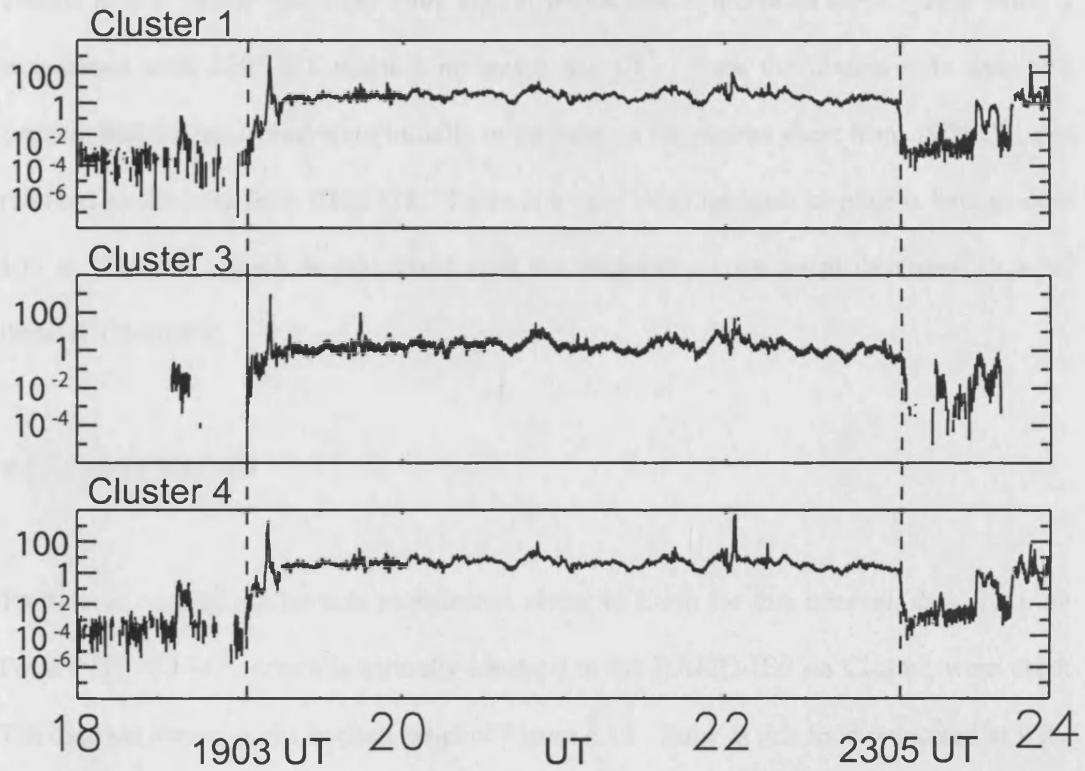
Figure 4.15: Plasma beta data from Cluster 1, 3 and 4 for 1st September 2002 (1800 to 2400 UT interval).

~0.1 indicate that the spacecraft are located in the plasma sheet. For the interval presented, plasma beta is below ~0.1 until 1903 UT, at which time it increases to ~1. This value is maintained until 2305 UT when it decreases to ~10^{-3}. Thus the plasma beta data also confirm that the spacecraft were initially in the lobe, in the plasma sheet from 1903 UT, and returned to the lobe from 2305 UT. There is a very large increase in plasma beta to over 100 at 1911 UT, which is associated with the magnetic cavity event described in more detail in Chapter 6.

4.2.7 Polar CEPPAD

To have an idea of the particle populations closer to Earth for this interval, data from the Polar CEPPAD-IES, which is virtually identical to the RAPID-IES on Cluster, were used. The data are shown in the bottom panel of Figure 4.15. Polar at this time is located at 9 R_E downtail, in the post-midnight sector. The CEPPAD-IES data show a decrease in the electron count rate in the same energy range as the RAPID data from 2240 UT. This drop-out is indicative of the plasma sheet thinning and growth phase. This is followed by a sudden plasma injection at 2305 UT, indicating expansion phase onset.

4.2.8 LANL geosynchronous energetic particle data

The low energy electron data from the LANL geosynchronous spacecraft (Figure 4.16) indicate that a dispersionless injection of plasma occurs at geosynchronous orbit (~6.6 R_E) at ~1827 UT. This is detected by two of the LANL spacecraft, which at this time are located in the post-midnight sector, close to the geographic equator. This plasma injection into the magnetotail is consistent with a substorm expansion phase onset occurring at 1823

49
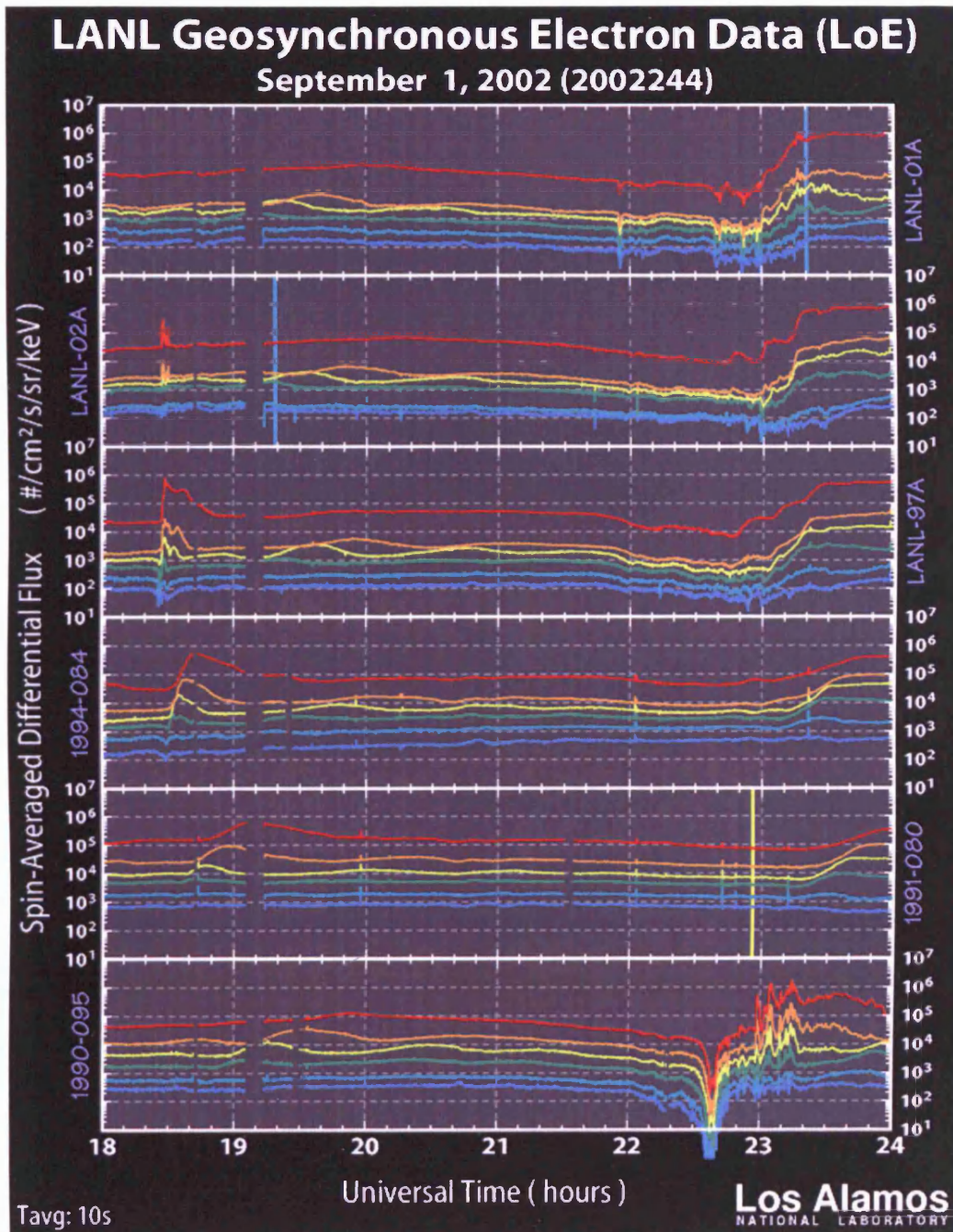
Figure 4.16: LANL low energy electron data from the SOPA instrument are shown for 1st
September 2002 (1800 to 2400 UT interval).

UT. There is also a plasma injection in the midnight sector at geosynchronous orbit around the time of the second substorm at 2305 UT, also detected by the LANL spacecraft.

4.3 Discussion

A number of events were observed during this interval which are seen by many different instruments, both ground-based and space-based, which helps to build an accurate picture of what is happening in both the magnetosphere and ionosphere simultaneously during the two substorm expansion phases described above.

The first substorm expansion onset occurred at 1823 UT, at which time the Cluster plasma instruments demonstrate that the spacecraft are in the tail lobe. There is a dispersionless plasma injection at 1827 UT in the post-midnight sector of the magnetotail at geosynchronous orbit, detected by two of the LANL spacecraft, consistent with substorm onset. The magnitude of the onset signature on the ground is weak due to the displacement of the stations from the onset location. This is consistent with the few minutes' delay between the ground magnetometer signature and the plasma injection at geosynchronous orbit. Also, a substorm signature is seen at Cluster in the FGM data at 1825 UT, with a simultaneous reduction in both the total magnetic field and in B_x at all spacecraft, indicating a temporal change in the magnetic field. The onset region is located to the east of the IMAGE ground magnetometer stations, at the location of the Tixie magnetometer station, where a clear substorm onset signature is detected. We thus define this as a substorm expansion phase rather than pseudobreakup. The Cluster spacecraft at this time are located at (-16, -1, 5) R_E in GSM coordinates, in the 01 MLT sector. FGM B_z also

50

changes sign from negative to positive at expansion phase onset and since no plasma sheet signature is seen in the plasma data, this is interpreted as a major re-orientation of the lobe field, a dipolarization. Although the Cluster spacecraft are not in the optimum position for the measurement of a substorm onset, the detection of these signatures at onset indicates that this event is a large scale feature. The IMF B_x, B_y and B_z components fluctuate during this time; in particular, both B_z and B_x turn positive at 1823 UT. The northward turning of IMF Bz will decrease the rate of dayside reconnection, but wider implications cannot be drawn from this single data set. Due to the substorm expansion phase onset, the magnetic field in the tail decreases from 1823 UT. Hence the reconnection at the dayside is less than in the magnetotail.

A brief enhancement of the ionospheric sunward flow near 70° magnetic latitude and 20 MLT accompanies expansion phase onset at ~1823 UT but a more significant enhancement of the sunward flow is seen some 5 to 10 minutes after expansion phase onset. A series of enhancements at the poleward edge of the scatter at the Hankasalmi radar are seen over the next 60 minutes or so. Such enhancements have been discussed by Sandholt et al. (2002), who observed 6 discrete poleward boundary intensifications (PBIs) of the auroral oval during a substorm event occurring on the 12 December 1999. These were identified by equatorward expansion of equatorward flow in the late expansion phase using the Hankasalmi (Finland) SuperDARN radar, much as is seen in the late expansion phase of the first substorm after 1823 UT. Sandholt and co-workers concluded that bursty bulk flows (BBFs) from the magnetic reconnection site may be a phenomena of late substorm expansion phase, resulting in the auroral and convection events seen at that time, and which may perhaps account for the flow enhancements seen in this particular event. We see no evidence for BBFs in the Cluster data at this time, which is due to the Cluster spacecraft

51

being in the northern tail lobe. Therefore we are unable to confirm Sandholt et al.'s interpretation of the radar signatures from this event.

At 1903 UT the CIS data show that the low-energy ions increase their x component of velocity (flow towards Earth), which is maintained until 1915 UT. This is a signature of ion beams in the PSBL (Eastman et al., 1984), indicating that the Cluster spacecraft cross the PSBL. The low-energy ion density also increases at 1903 UT, and is maintained until 2305 UT. The PEACE data similarly show an increase in the density of low-energy electrons from 1903 UT. The density reaches its maximum value at 1910 UT, and remains there until 2305 UT when there is a sudden decrease in density. Moreover the RAPID data show an increase in the number of high-energy electrons and ions from 1903 UT until a sudden decrease at 2305 UT. RAPID, PEACE and plasma beta data are all consistent with the Cluster spacecraft entering the plasma sheet after crossing the PSBL and remaining there until 2305 UT when they suddenly re-enter the lobe. The unit normal at which the spacecraft cross the PSBL into the plasma sheet at 1903 UT indicates that it is inclined mainly in the y-z plane, with negative y component. The boundary is travelling at 30 km s^{-1} which is slower than typical values which are 60 ± 37 km s^{-1} (Dewhurst et al., 2003). The changing orientation of the y-direction of the boundary normal may indicate flapping of the plasma sheet (e.g. Nakamura et al., 2002) between entry to the plasma sheet at 1903 UT and exit at 2305 UT.

Pseudobreakups are seen by the IMAGE ground magnetometers at 2240 and 2256 UT prior to the second expansion phase onset. The IMF as seen at ACE (lagged by 75 minutes) has been southward from around 2055 UT (and remains southwards until after 2400 UT), and all components have been approximately constant from 2215 UT (and remain so until

around 2345 UT). Scatter from the Hankasalmi radar begins to be lost following the first pseudobreakup, first from the eastern beams and finally from the western beams by 2300 UT, after which no further scatter is seen in the Hankasalmi radar data. The Þykkvibær radar shows an intensification of westward flow (toward the radar) at 2240 UT, maintained until 2314 UT after which scatter is also lost. At 2242 UT and 2252 UT the SuperDARN data show intensifications in the flow in the midnight sector at 65° to 75° latitude and these enhanced flows are associated with the pseudobreakups. The Cluster FGM data show a peak in the B_x component of the magnetic field at Cluster 1, 2 and 4 at 2240 UT, which decreases simultaneously at all spacecraft from 2244 UT until 2250 UT. The B_y component also decreases from 2244 UT, until 2250 UT. This feature shows some variability in its velocity as it moves towards the 01 MLT region. Furthermore Polar CEPPAD data shows a dropout in the near-Earth particle populations at ~2240 UT, the time of the first pseudobreakup.

A full substorm onset occurs at 2305 UT as seen at the IMAGE magnetometer stations. At this time, Pi2 pulsations commence at all latitudes, in all components of the magnetic field. The higher latitude stations show a decrease in the B_x component as expected at substorm onset, while the lower latitude stations show an increase in the B_x component, indicative of the SCW. Onset is detected at stations equatorward of the ionospheric projection of the Polar spacecraft's path first, followed by stations in its path. This implies that the onset location in the tail was Earthward of the Polar spacecraft. The Hankasalmi radar has lost much of the ionospheric scatter at this time, but the SuperDARN map potential data indicate that there are intensified flows from 2258 UT in the 00 MLT, 65° to 75° latitude region. This is maintained, with some further intensification, until 2312 UT after which the ionospheric scatter is completely lost in the midnight sector. The strongest flows during

this time are now poleward of the location of the flows during pseudobreakups. The x component of the magnetic field at all Cluster spacecraft reaches a peak at 2305 UT, then decreases at all spacecraft simultaneously such that over the next hour it decreases by a factor of two. The B_y component also begins to decrease at this time, while the B_z component increases. Also, there are fewer fluctuations in the magnetic field from 2305 UT. This is indicative of the dipolarization of the magnetotail and reduction in field magnitude at the expansion phase onset, consistent with the indication from the Cluster particle data and plasma beta that the spacecraft re-enter the lobe at 2305 UT. However, the plasma data show no signature for the PSBL at 2305 UT, indicating that either the exit to the lobe occurs more rapidly than the entry or there were no flows in the PSBL at this time. The near-Earth Polar CEPPAD data also show a plasma injection at 2305 UT, consistent with substorm onset. The LANL geosynchronous spacecraft also show a plasma injection at this time. The unit normal at which the Cluster spacecraft cross the PSBL to return to the lobe indicates that it is inclined mainly in the y-z plane, with both y and z components negative. The boundary is travelling at 38 km s^{-1} which is faster than the previous entry but again slower than typical values previously found (Dewhurst et al., 2004).

It is interesting to note that the magnetic field in the magnetotail lobe decreases from 2305 UT despite the IMF as seen at ACE remaining steady and southward. This implies that magnetic flux is being lost from the magnetotail due to tail reconnection faster than it is being replaced by reconnection at the dayside magnetopause, as in the earlier substorm.

4.4 Summary and conclusions

The first substorm event at 1823 UT on the ground indicates that the ground-based magnetometers see the substorm event first, followed by the Cluster spacecraft, two of the geosynchronous LANL spacecraft and ionospheric radars respectively. The Cluster spacecraft at this time are not ideally placed to observe substorm signatures in the tail, being in the lobe and well away from the plasma sheet. Nevertheless, the Cluster spacecraft detect a substorm signature in the lobe as demonstrated by the FGM data presented above. The loss of flux in the lobe occurs at substorm expansion phase onset, indicating reconnection either began at expansion phase onset or had begun somewhat earlier. Reconnection at the dayside is reduced following the northward turning at 1823 UT. Furthermore, we estimate reconnection lasted only for the first 15 minutes or so of the expansion phase, corresponding to the time during which magnetic flux in the magnetotail was decreasing. This indicates that the effects of the substorm expansion phase at the location of the Cluster spacecraft, in the post-midnight sector of the lobe region of the magnetotail, were of relatively short duration.

The second substorm onset at 2305 UT is seen simultaneously on the ground, in the magnetotail and at the Polar spacecraft's nearer-Earth position. The response in the ionosphere takes one minute longer to develop than at the spacecraft. The evidence that reconnection takes place within the Polar orbit at 9 R_E downtail needs further study as this value is much closer to Earth than the accepted location of the NENL at 20 to 30 R_E downtail. The Cluster spacecraft cross the PSBL very rapidly, such that the signature in the particle data shows only their exit to the lobe. While in the lobe, magnetic flux is again lost which implies that reconnection is taking place but over a much longer timescale.

55

Dipolarization takes place at 2305 UT which indicates that reconnection must be taking place at the NENL at this time. This means that information propagation must be from the NENL towards Earth, as there would not be sufficient time for information to be propagated from the inner current sheet to the NENL and back again, given the timings presented here. Thus, this event would appear to better fit the NENL model for substorm onset than the CCI model.

In both events enhanced ionospheric flows occur following the expansion phase and in the case of the second event in association with the pseudobreakup. There is a major difference between the location of the flows stimulated by the pseudobreakup and expansion phase in terms of their location, the former located equatorward of the latter. This requires further study to see if this is repeatable.

Chapter 5

Cluster magnetotail observations of a tailward-travelling plasmoid at substorm expansion phase onset and field aligned currents in the plasma sheet boundary layer

In this chapter we examine observations from a large number of instruments collecting data in the solar wind, magnetosphere and ionosphere in order to determine the development of a substorm on a large scale. Interesting features of the magnetic field and current systems are presented and explained in the context of the instruments' locations.

5.1 Instruments

Data from the FGM, CIS, PEACE and RAPID instruments on the four Cluster spacecraft were used in this study. At the time of interest the Cluster spacecraft were located at around 15 R_E downtail, 8 R_E from midnight in the pre-midnight sector and around 2 R_E above the equatorial plane at a separation of ~1 R_E; Cluster 1 was located closest to midnight, Cluster 2 furthest from midnight, Cluster 3 closest to the equatorial plane, and Cluster 4 was located farthest downtail. Figure 5.1 presents the position of the magnetic footprint of the Cluster 1 spacecraft on 5 October 2002 between 0000 and 0600 UT (orange line) mapped using the Tsyganenko 1996 model (Tsyganenko and Stern, 1996).
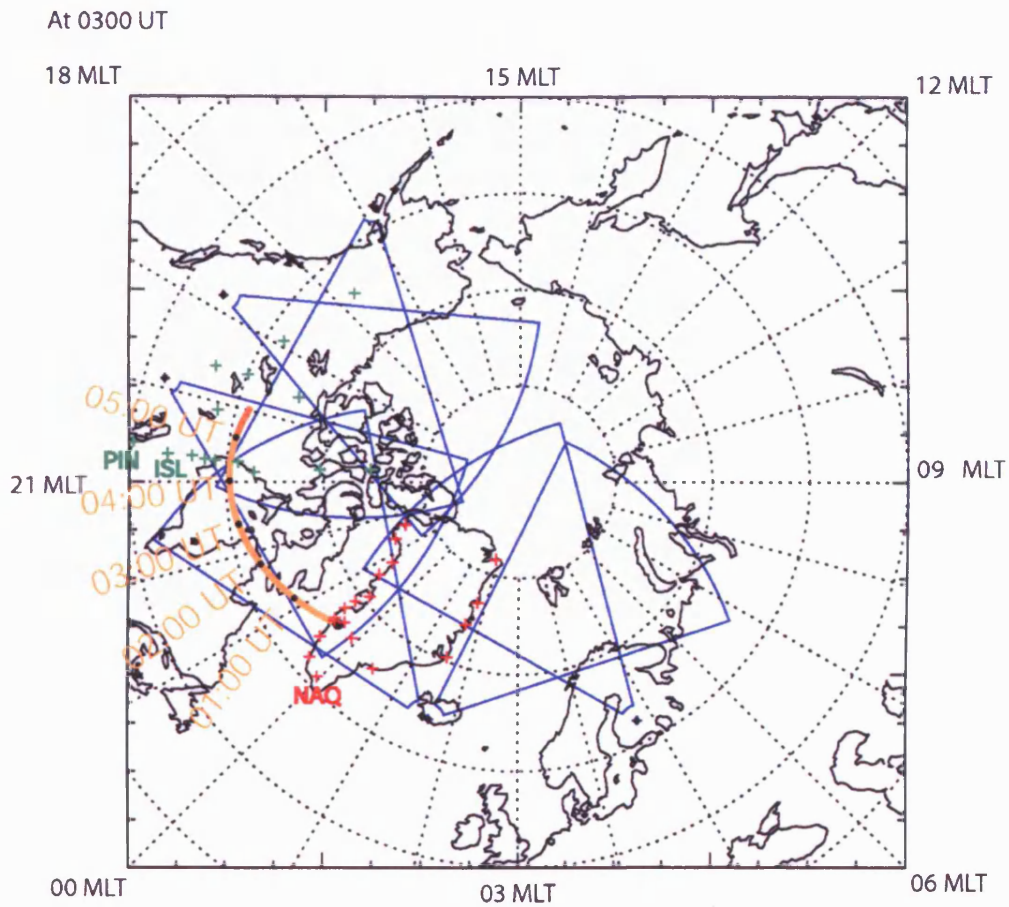
Figure 5.1: Northern hemisphere polar cap within 60 degrees at 0300 UT on 5 October 2002 in geographic coordinates. Magnetic local times (MLT) refer to 0300 UT locations. Shown in blue are six of the nine SuperDARN radar fields of view from which data are used in this study. In green are the locations of the CANOPUS magnetometer stations, in red those of the Greenland magnetometer stations. The Cluster footprint is shown in orange.

Supporting data were available from a number of other sources. The solar wind conditions for this event were measured using the MAG and SWEPAM instruments on the ACE spacecraft. The near-Earth (6.6 R_E) downtail conditions were investigated for this event using magnetic field data from the GOES-8 spacecraft and energetic proton and electron flux data from a the LANL-01A spacecraft. Data from the CANOPUS and Greenland ground-based magnetometer chains were also used in this study. CANOPUS magnetometers are located in west-central Canada (green crosses on Figure 5.1), while the Greenland magnetometers are located along the eastern and western coasts of Greenland (red crosses on Figure 5.1). Magnetometer stations of particular interest are labelled. Unfortunately, data from other magnetometer sites located between CANOPUS and Greenland were not available to provide more comprehensive coverage of this region of the ionosphere, as they were either located at too high a latitude to detect the substorm onset, or had no data available for this interval.

Ground-based data were also used from six of the northern hemisphere SuperDARN HF radars (Kodiak, Prince George, Þykkvibær, Hankasalmi, Saskatoon, Stokkseyri; depicted in blue in Figure 5.1). These line-of-sight velocity data were used to obtain ionospheric flows.

5.2 Data description

5.2.1 Ground magnetometer data, SuperDARN radar data, and IMF conditions

Figure 5.2 shows data from two selected CANOPUS magnetometer stations, Island Lake

CANOPUS & Greenland

X, Z and Pi2 filtered data

0250 UT

5 Oct 2002
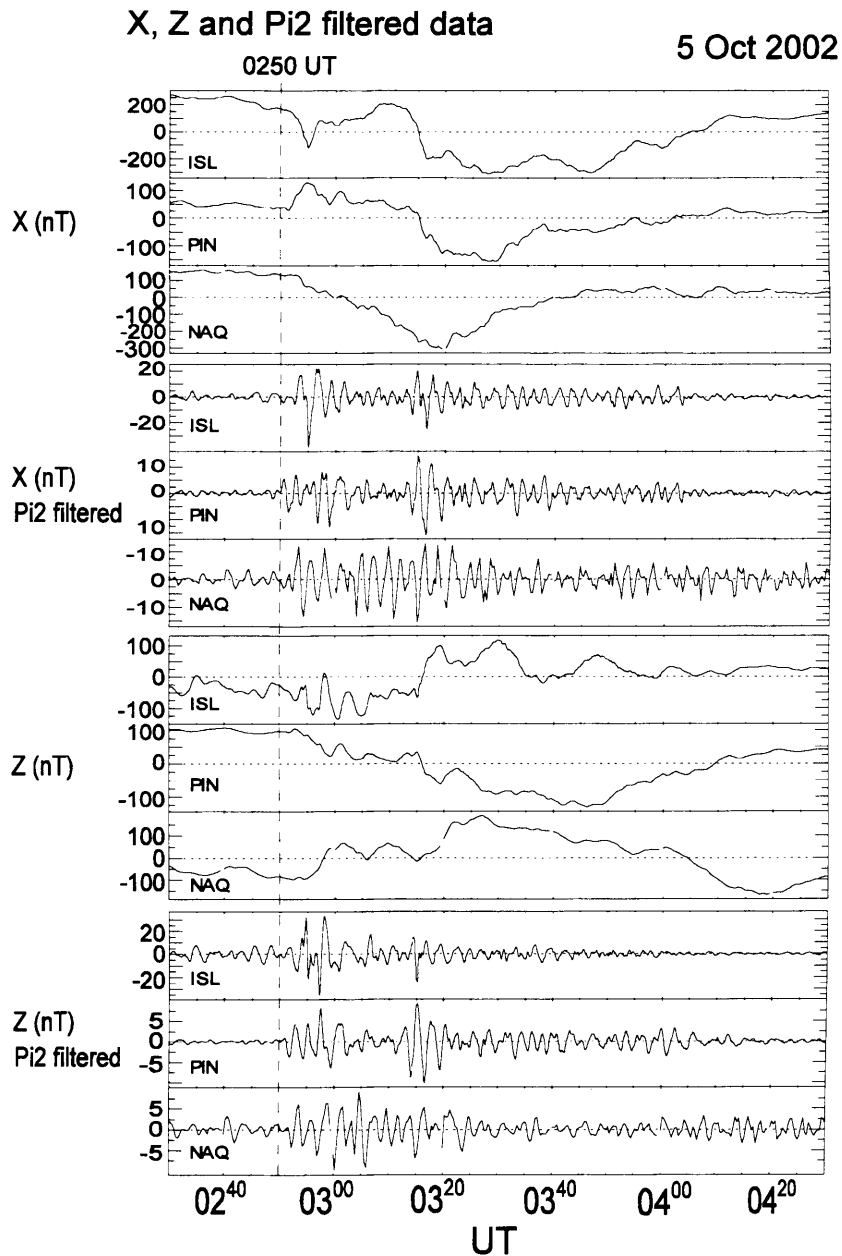
Figure 5.2: CANOPUS and Greenland magnetometer data for 5 October 2002, from 0230 to 0430 UT, for the Island Lake (ISL), Pinawa (PIN) and Narsarsuaq (NAQ) stations. Panels depict: X component of magnetic field; Pi2 filtered (period band 20 to 200 s) X component; Z component of magnetic field; Pi2 filtered Z component. Substorm onset at 0250 UT is indicated by the vertical dashed line.

(ISL, 64.74 ° invariant latitude; 21 MLT at 0330 UT) and Pinawa (PIN, 60.98 °; 21 MLT at 0330 UT), and from the Narsasuaq (NAQ, 66.31 °; 0130 MLT at 0330 UT) Greenland station for 5 October 2002, from 0230 to 0430 UT. Shown are the X and Z components of the magnetic field at each station, and the X and Z components which have been filtered between 20 and 200 s to provide information on the presence of Pi2 wave activity. The filtered X component of the magnetic field first detected Pi2 waves at 0250 UT, and this time is taken as that of substorm expansion phase onset in the absence of optical data for this event. At 0252 UT a decrease in the X component at the ISL station and a positive increase in the X component at PIN were detected. The PIN station also detected a decrease in the Z component of the magnetic field at this time, whilst ISL detected a gradually decreasing Z component. Given that both ISL and PIN were located at the same local time we conclude that ISL detected a westward electrojet, and was equatorward of the centre, whilst PIN detected the edge of the eastward electrojet. The NAQ station detected Pi2 pulsations from 0252 UT. The X component of the magnetic field decreased from 0253 UT, indicating detection of the westward electrojet. At onset, the Z component of the magnetic field was negative, increasing and turning positive around 8 min after onset. This indicates that the centre of the westward electrojet was located poleward of the NAQ station at onset, and equatorward of the NAQ station from 8 min after onset.

Line-of-sight velocity measurements from six of the SuperDARN radar array (Kodiak, Prince George, Þykkvibær, Hankasalmi, Saskatoon and Stokkseyri) were available for this interval. They were combined using the map potential analysis technique (Ruohoniemi and Baker, 1998) to produce large-scale global convection maps at two-minute intervals over the period of interest. At substorm onset, no strong flows were detected in the pre-midnight sector (see Figure 5.3a). However, intensification of ionospheric flow occurred in the

59
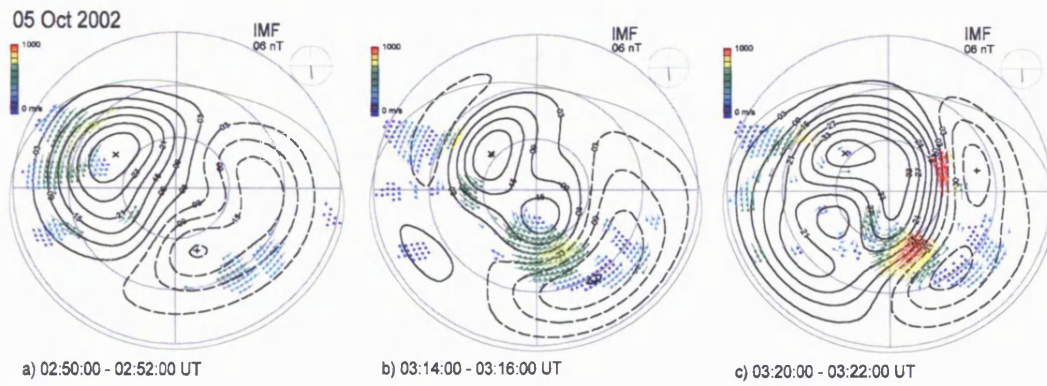
Figure 5.3: SuperDARN map potential plots for 5 October 2002 in the northern hemisphere polar cap within 60 degrees (geographic coordinates) with IMF value and direction indicated. Noon local time is at the top of the plot. a) 0250 to 0252 UT; b) 0314 to 0316 UT; c) 0320 to 0322 UT.

midnight sector to ~800 m s^{-1} from 0314 UT (24 min after onset; Figure 5.3b), and to ~1000 m s^{-1} from 0320 UT (30 min after onset; Figure 5.3c). This is different from the two events in Chapter 4, for which flows were detected before and at substorm expansion phase onset.

The IMF conditions for this event are shown in Figure 5.4. These are data from the MAG and SWEPAM instruments on the ACE spacecraft for 5 October 2002, from 0130 to 0330 UT. They are lagged by 66 min to take into account the time between the solar wind being detected at the spacecraft and it reaching the Earth's magnetopause. This lag is found using the technique of Khan and Cowley (1999). The IMF conditions around onset time were generally steady, with B_z negative for around 45 min prior to onset (apart from a small northward excursion around 15 min prior to onset). After onset the IMF conditions remained steady with B_z negative. The solar wind velocity was ~400 km s^{-1} for the interval, and the dynamic pressure underwent a graduated increase from ~0.9 nPa to ~1.1 nPa over ~40 min. It is worth noting that the data show no evidence for substorm triggering.

5.2.2 Near-Earth instruments

Figure 5.5 shows magnetometer data from the GOES 8 spacecraft for 5 October 2002, from 0230 to 0430 UT. In GSM, this spacecraft was located 5.5 R_E downtail, 3.4 R_E from midnight in the pre-midnight sector and within 0.5 R_E of the GSM equatorial plane in the 22 MLT sector. The satellite is located north of the magnetic equator. A slight increase in the latitude angle of the field, λ (where $\tan \lambda = B_z/\sqrt{(B_x^2+B_y^2)}$), is observed at 0250 UT and
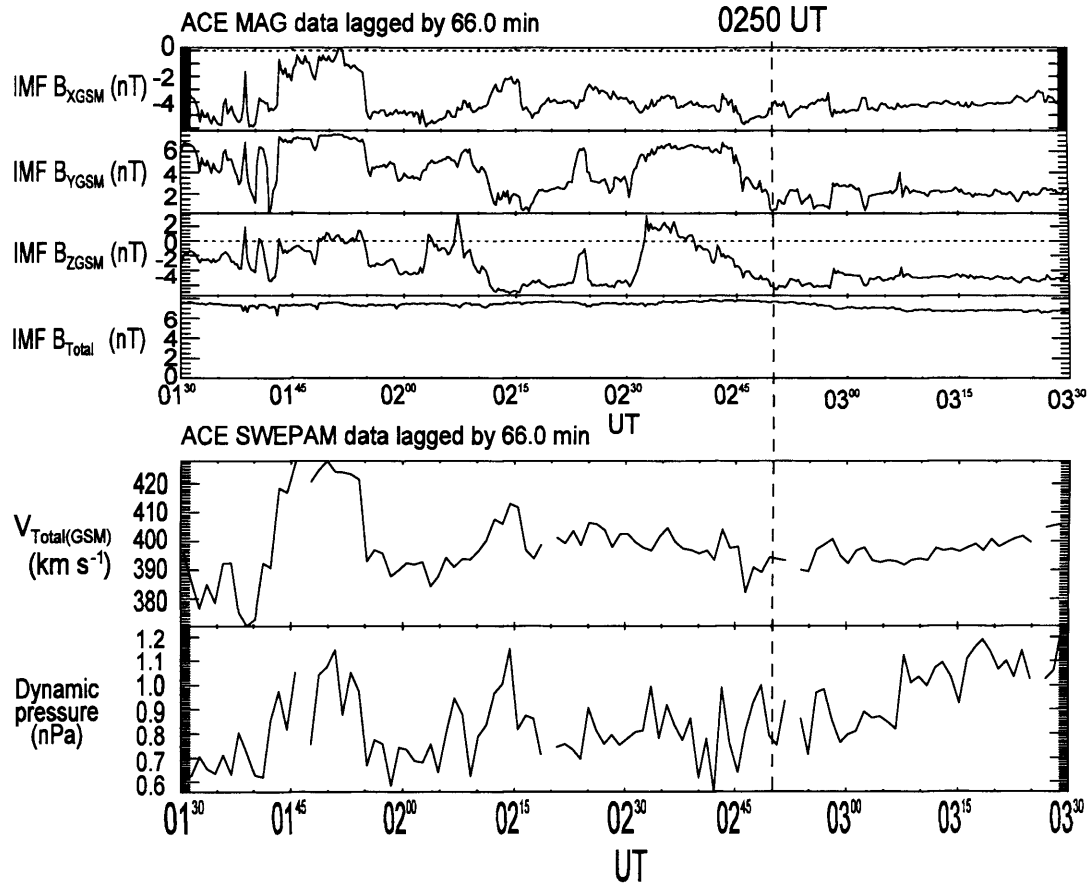
Figure 5.4: ACE MAG and SWEPAM data for 5 October 2002, from 0130 to 0330 UT, lagged by 66 min. Top panel depicts MAG data: B_x, B_y, B_z components of magnetic field and the total magnetic field, in GSM coordinates. Bottom panel depicts SWEPAM data: total velocity and dynamic pressure.

GOES 8 MFI   5 Oct 2002

0250UT 0256UT
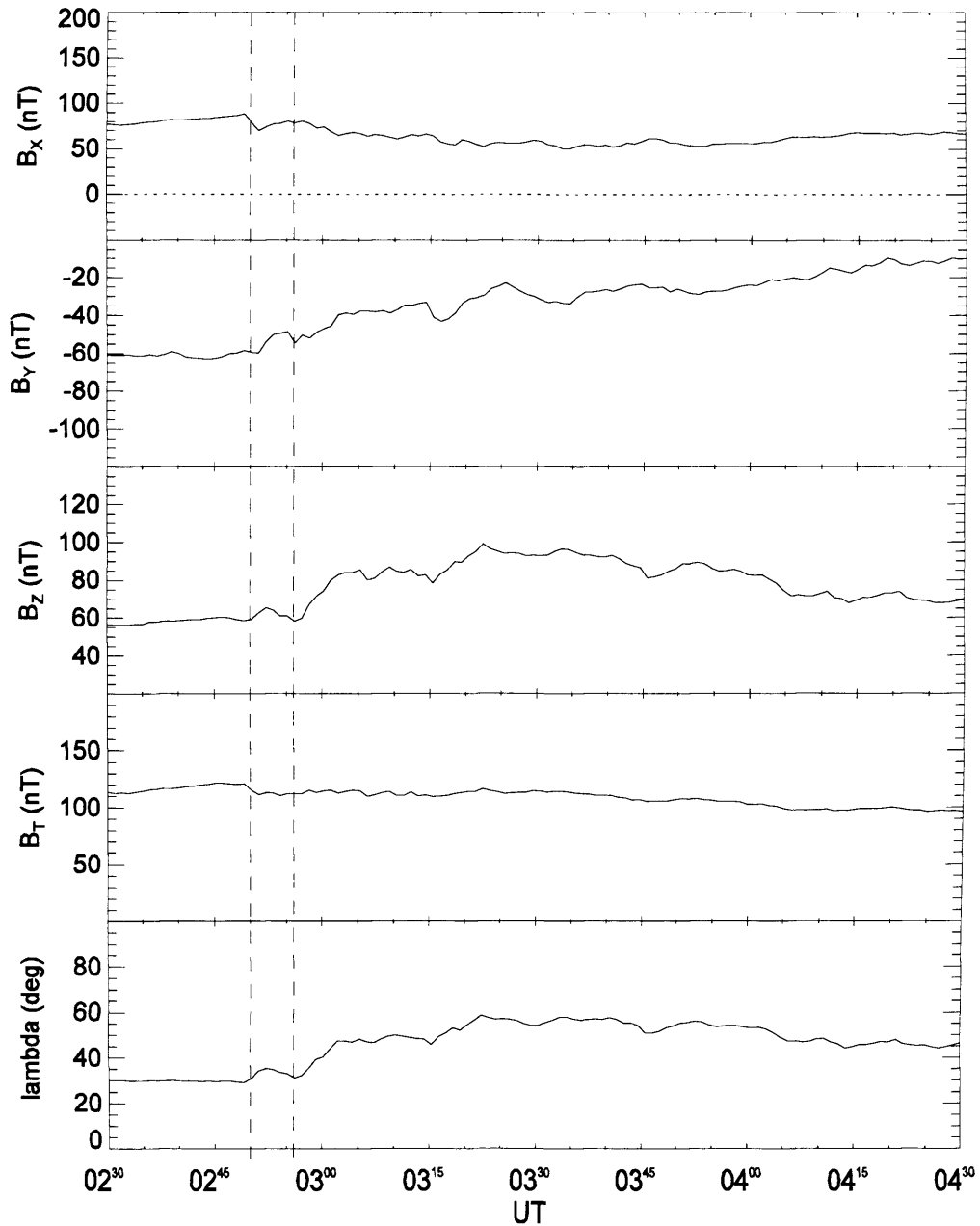
Figure 5.5: GOES 8 magnetometer data for 5 October 2002, from 0230 to 0430 UT. B_x,

B_y, B_z components of magnetic field, total magnetic field, and lambda, where $\tan \lambda =$

$B_z/\sqrt{(B_x^2+B_y^2)}$, are shown.

is followed by a stronger increase at 0256 UT, indicating dipolarization of the magnetic field at 6.6 R_E downtail. This is the signature of expansion phase onset at this location in the magnetosphere.

Particle data from the Synchronous Orbit Particle Analyzer instruments (SOPA; Belian et al., 1992) on the LANL-01A (located in 4 MLT sector at 0300 UT), -02A (8 MLT at 0300 UT), -97A (10 MLT at 0300 UT) and 1991-080 (16 MLT at 0300 UT) spacecraft are shown in Figures 5.6 (50-315 keV electrons) and 5.7 (50-400 keV protons) for 5 October 2002, from 0000 to 0600 UT. The spacecraft located closest to the magnetotail at substorm expansion phase onset is therefore LANL-01A. The electron data show a plasma injection at this spacecraft at 0251 UT, with dispersed injections resulting from this event detected at other spacecraft at later times, most notably at the spacecraft located at 16 MLT (1991-080). The proton data show an increase in the dispersed injection at all spacecraft, occurring earliest at 0255 UT at the spacecraft located at 16 MLT (1991-080).

5.2.3 Cluster data overview

5.2.3.1 Cluster Particle Data

The ion data from the CIS instrument on Cluster 1, 3 and 4 are shown in Figure 5.8 for 5 October 2002, from 0230 to 0430 UT. Note that the CIS instrument on Cluster 2 was not operational. The plots show the low energy (0.02 eV to 30 keV) ion density, V_x and V_y velocity components (GSM coordinates) and plasma beta ($2\mu_0 nkT_\perp/B^2$, calculated from CIS and FGM data). Figure 5.9 shows low energy electron (0.7 eV to 30 keV) flux data from
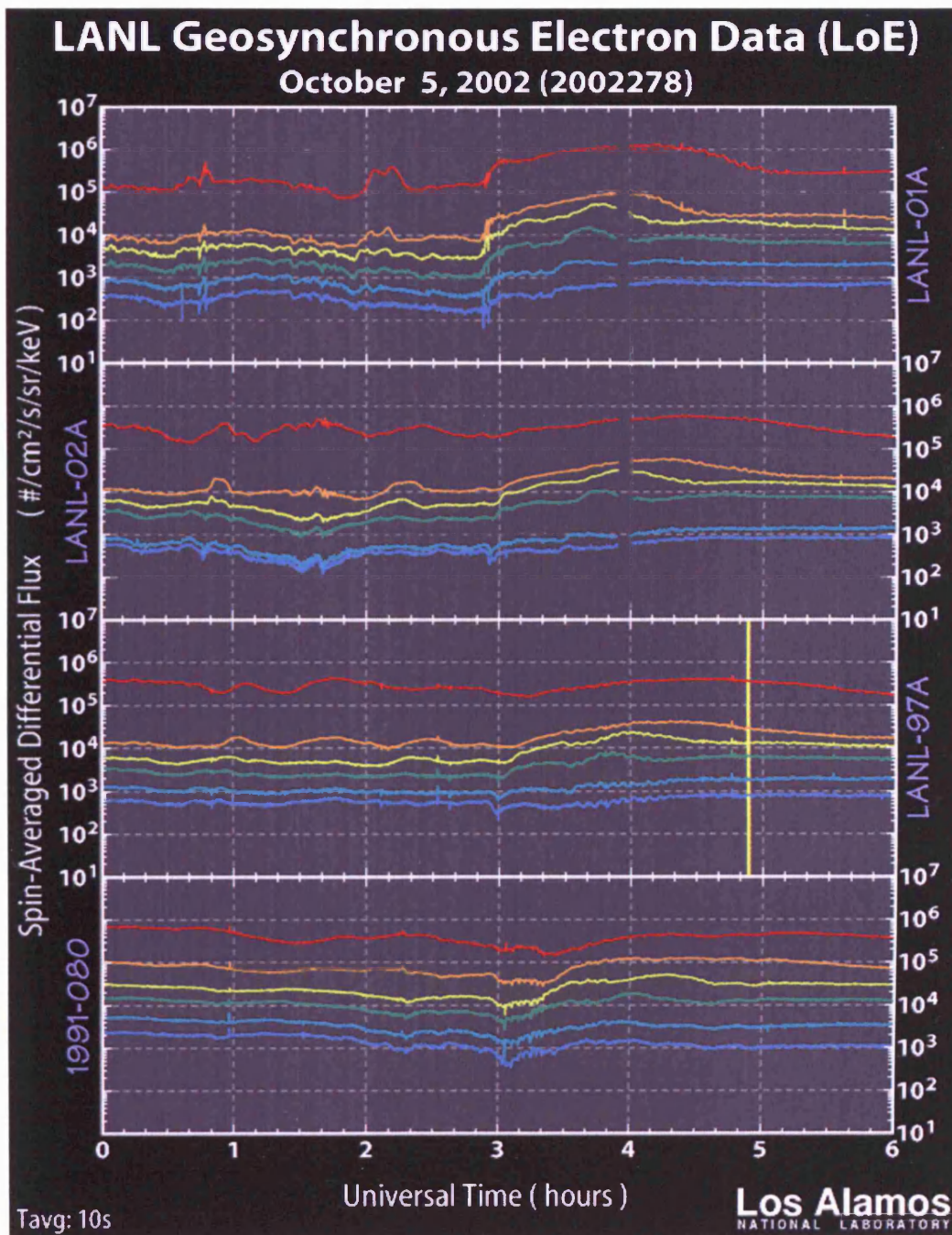
Figure 5.6: LANL low energy electron data for 5 October 2002, from 0000 to 0600 UT.
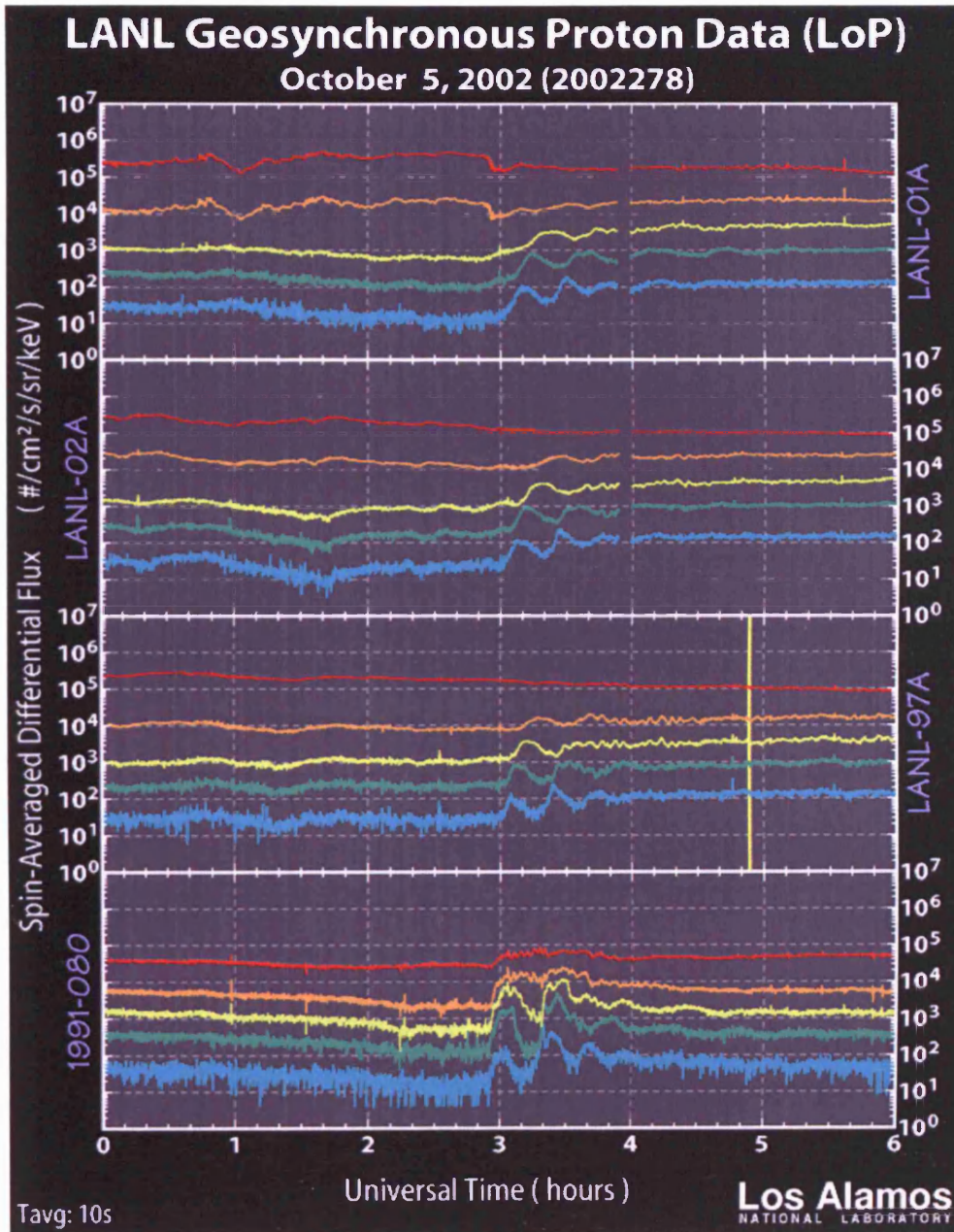
Figure 5.7: LANL low energy proton data for 5 October 2002, from 0000 to 0600 UT.
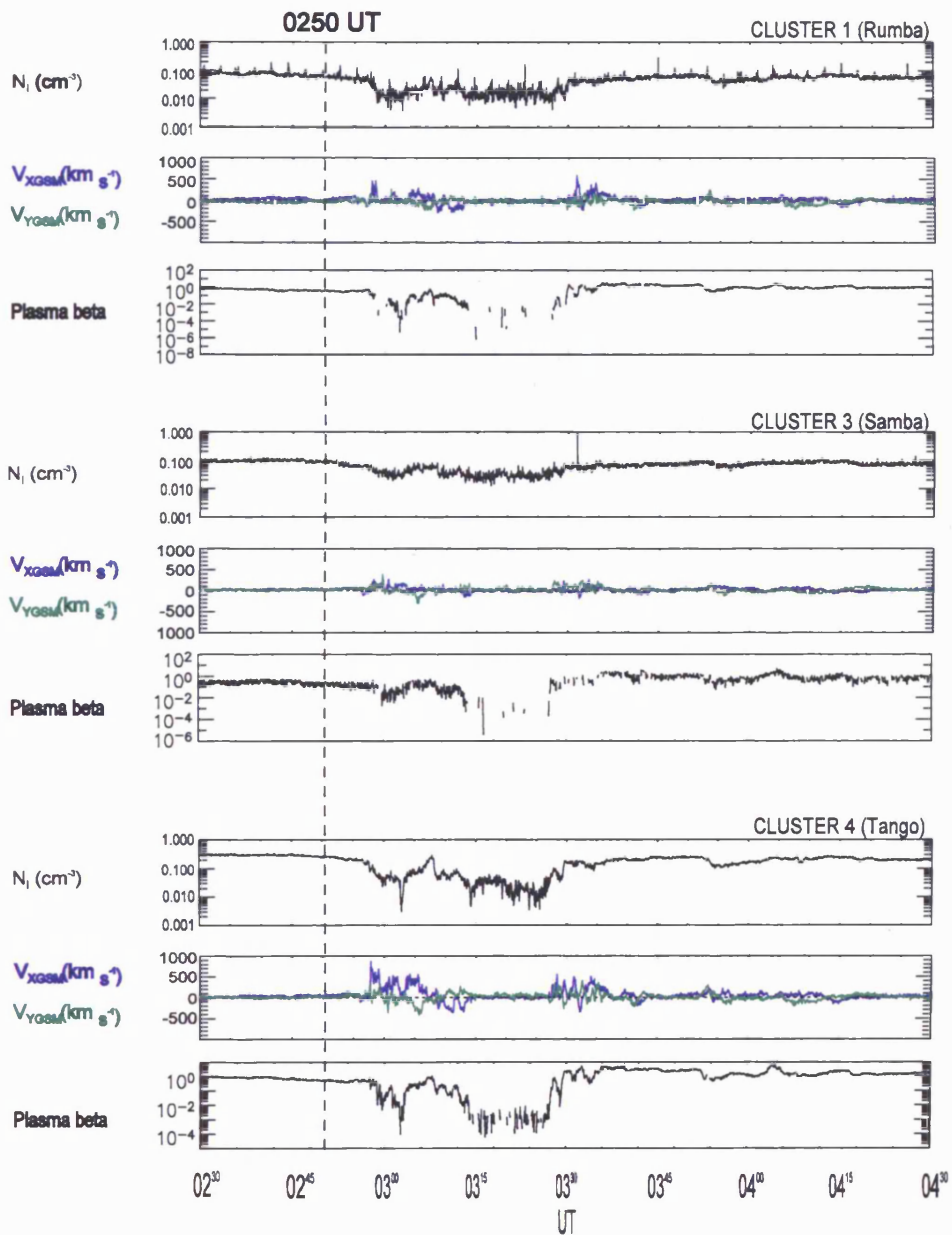
Figure 5.8: Cluster CIS ion data from spacecraft 1, 3 and 4 for 5 October 2002, from 0230 to 0430 UT; density, x and y velocity components (GSM coordinates) and plasma beta are shown for each spacecraft.
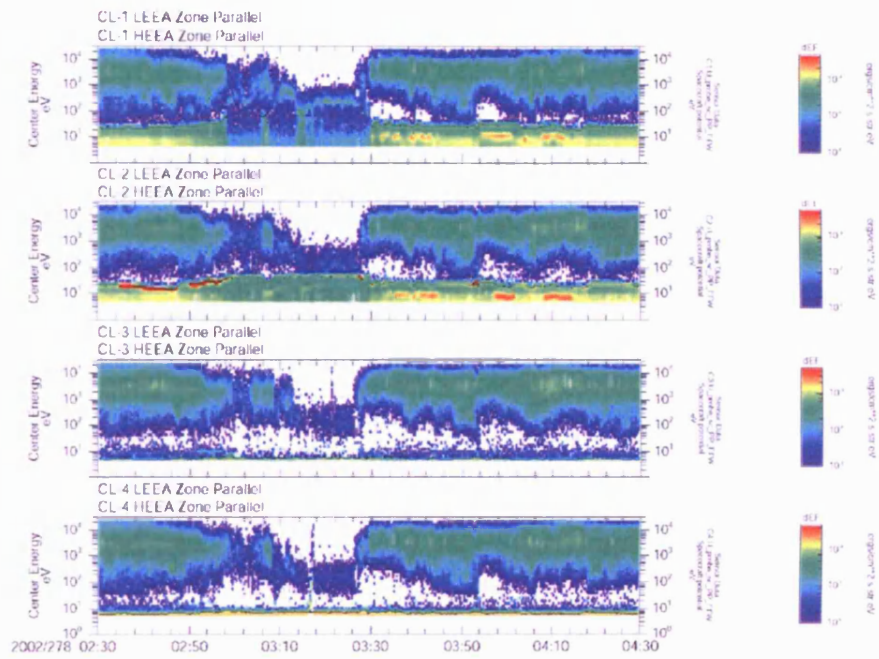
Figure 5.9: Cluster PEACE electron energy data from all spacecraft for 5 October 2002, from 0230 to 0430 UT.

the four PEACE instruments, and Figure 5.10 shows high energy electron flux data (20 to 400 keV) from the four RAPID-IES instruments.

The CIS instrument (Figure 5.8) detected an ion density of ~0.1 cm^{-3} before the substorm expansion phase onset at 0250 UT, indicating that the Cluster spacecraft were located in the plasma sheet. The PEACE and RAPID-IES data (Figures 5.9 and 5.10 respectively) corroborate this: the PEACE instrument detected a differential flux of ~0.5 s^{-1} cm^{-2} sr^{-1} keV^{-1} in the 1 to 10 keV energy range, while the RAPID-IES instrument detected a differential flux of ~2.7 s^{-1} cm^{-2} sr^{-1} keV^{-1} in the 40 to 400 keV range. At 0257 UT the Cluster spacecraft entered the plasma sheet boundary layer, as the density began to decrease and fast Earthward-directed beams (composed primarily of protons) in the V_x component of velocity were detected by the CIS instruments. Such beams are the signature of the plasma sheet boundary layer (PSBL, e.g. Baumjohann et al., 1988). These beams became tailward-directed from 0308 UT until 0314 UT, but had plasma characteristics similar to the Earthward-directed beams. The PEACE data show that the spacecraft did not exit swiftly from the PSBL, but remained in it for around 15 min before entering the lobe at 0314 UT. Cluster 3, which was located closest to the equatorial plane, detected the smallest decrease in density and the smallest plasma beams. This is consistent with Cluster 3 being further into the plasma sheet than the other spacecraft. At 0330 UT the plasma instruments on the Cluster spacecraft detected plasma densities close to those before onset, indicating that they re-entered the plasma sheet at that time. This was accompanied by further PSBL beam signatures detected by the CIS instrument, directed mainly Earthward.

The plasma beta plots for the three spacecraft clearly depict the spacecraft as initially in the plasma sheet, when plasma beta is close to 1. Plasma beta decreases at all spacecraft at
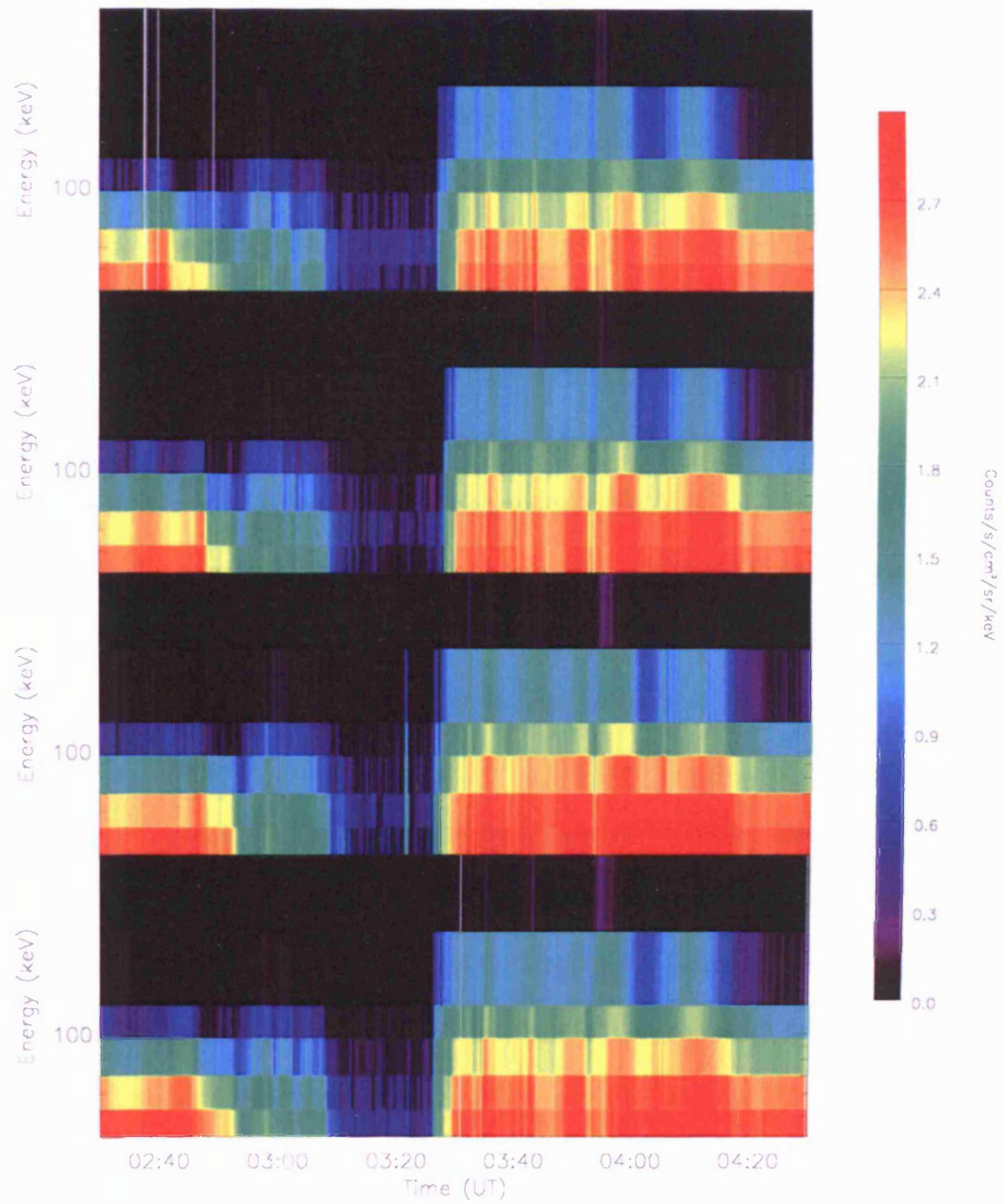
Figure 5.10: Cluster RAPID-IES electron energy data for 5 October 2002, from 0230 to 0430 UT.

0257 UT when the spacecraft enter the PSBL, fluctuating between $\sim 10^{-4}$ and 1 at spacecraft 1 and 4 and between $\sim 10^{-2}$ and 1 at spacecraft 2, then show a clear transition to the lobe at 0314 UT when plasma beta is less than 10^{-2} at all spacecraft. There is another clear transition at 0330 UT when the spacecraft re-enter the plasma sheet, with plasma beta recovering to ~ 1 at all spacecraft.

5.2.3.2 Cluster Magnetic Field Data

The Cluster FGM data are shown in panels 1 to 4 of Figure 5.11a, and in more detail for the 0240 to 0310 UT interval in the top four panels of Figure 5.11b. Starting 0251 UT (1 min after onset), there was a decrease in the x component of the magnetic field from ~ 33 nT to ~ 26 nT over a 4 min period. Over this same period, the z component of the magnetic field also decreased, from ~ 0 nT to ~ -6 nT, and then recovered to ~ 0 nT. All spacecraft detected the decrease at virtually the same time with detailed analysis revealing that Cluster 4, located farthest downtail, detected the negative turning of B_z last; the recovery was also detected slightly earlier by Cluster 1 than by Cluster 4. Usually, dipolarization of the magnetic field at substorm expansion phase onset is characterized by a decrease of the x component of magnetic field, accompanied by a positive increase in the z component of magnetic field (e.g. Baumjohann et al., 1999). Therefore the signature detected in this case was not associated with dipolarization.

The current densities calculated from the magnetic field are shown in panels 5 to 7 of Figure 5.11a. These are calculated from FGM data from all four spacecraft, with an indication of the accuracy of the calculation given by div B/curl B (panel 8). When div B is small, the values calculated for the current densities are reliable. Prior to onset a current
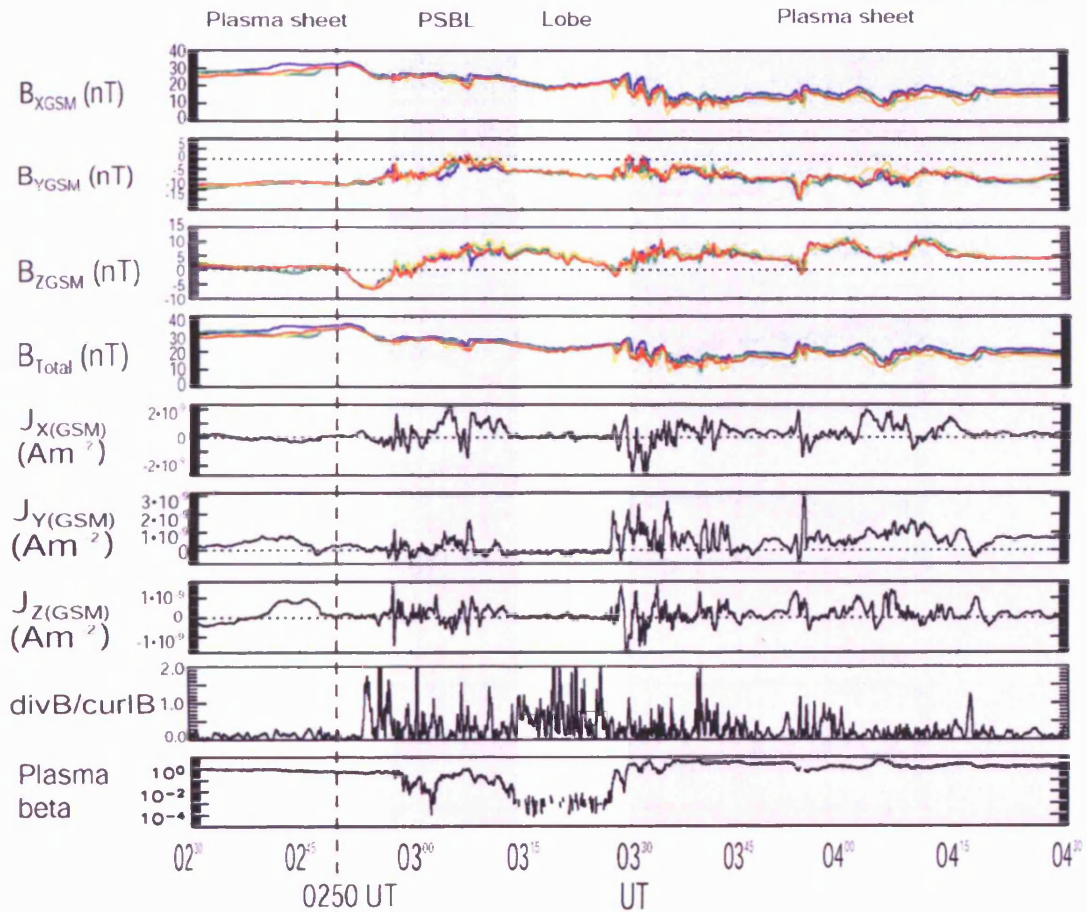
Figure 5.11a: Cluster FGM data for 5 October 2002, from 0230 to 0430 UT. B_x, B_y, B_z components of the magnetic field (GSM coordinates), the total magnetic field, J_x, J_y, J_z components of the current (also GSM coordinates), div B/curl B and plasma beta are shown, with shaded areas representing regions of magnetosphere.
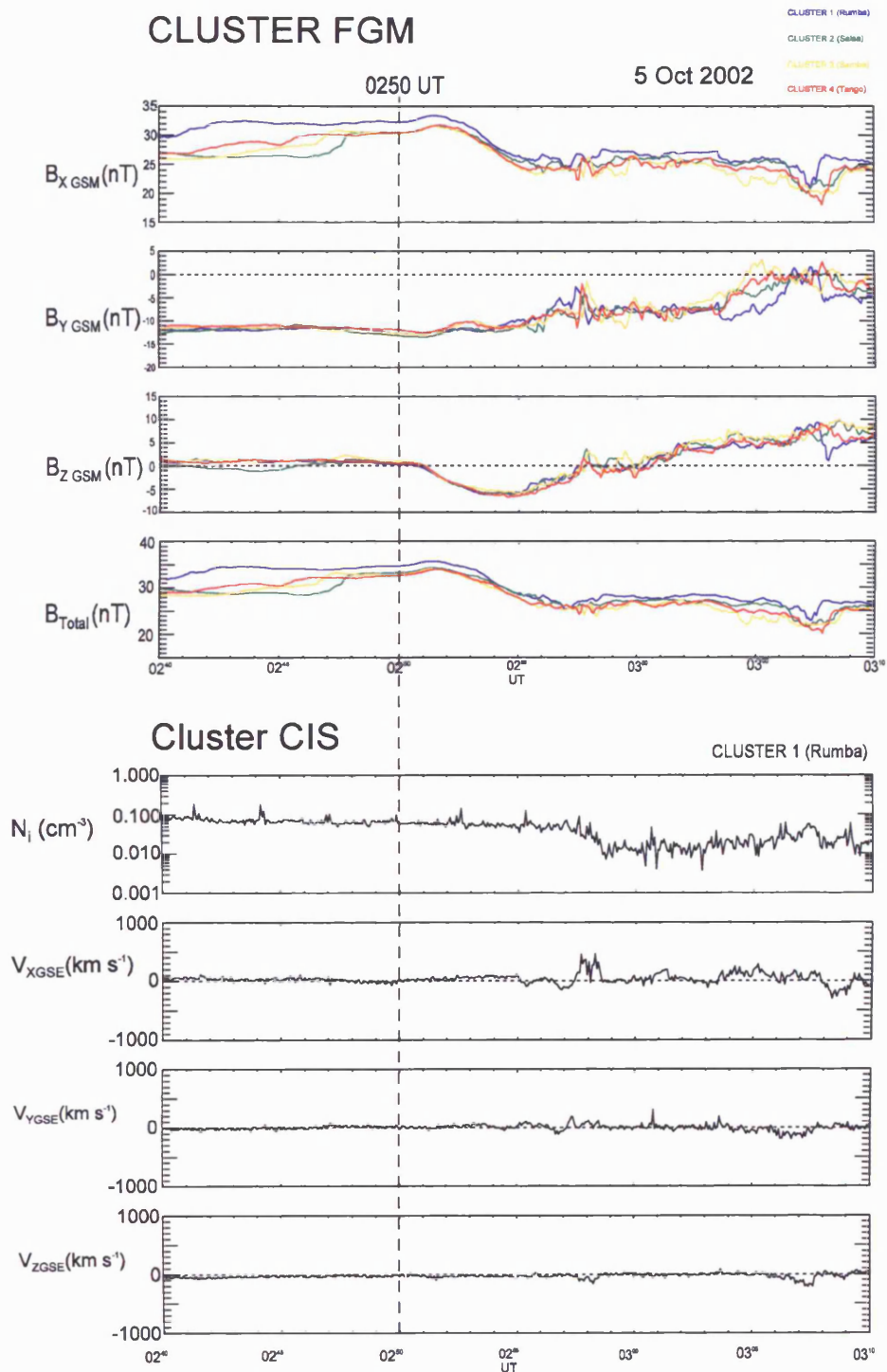
Figure 5.11b: Zoomed view for the 0240 to 0310 UT interval: B_x, B_y, B_z and B_{total} Cluster

FGM data from the four spacecraft and density, V_x, V_y and V_z CIS data from Cluster 1.

density of ~ 0.8×10^{-9} A m^{-2} was detected in the y direction, indicative of the cross-tail current at the location of the Cluster spacecraft. This current was mainly due to a difference of the x component of the magnetic field in the z direction. The spacecraft detected a total magnetic field of ~30 nT prior to onset, indicating a change in B_x of ~60 nT across the plasma sheet inside Cluster. Typically, the current sheet thickness would be around 5 R_E. This implies a total current density of ~ 60 nT / (μ_0 x 5 R_E), or ~ 2×10^{-9} A m^{-2}. This is of the order of twice the value deduced from the FGM data, and is consistent with a spacecraft location away from the centre of the plasma sheet (where the current density is reduced). A few minutes prior to onset this J_y current density is lost, but the total magnetic field remains the same, indicating that the total current within the plasma sheet has remained the same.

When the spacecraft crossed into the plasma sheet boundary layer from the plasma sheet at 0257 UT, predominantly Earthward-directed J_x current densities were detected by the spacecraft to a peak value of ~2.3×10^{-9} A m^{-2}. At 0330 UT, the spacecraft crossed the plasma sheet boundary layer from the lobe back into the plasma sheet, and this time mainly tailward-directed J_x current densities were detected, to a peak value of ~ -2.7×10^{-9} A m^{-2}. Examination of the magnetic field data shows that these currents were associated mainly with B_y varying in the z direction, rather than B_z varying in the y direction.

5.3 Discussion

The substorm expansion phase onset timing for this substorm is taken as 0250 UT. This is from the earliest Pi2 pulsation detection at the PIN and ISL magnetometer stations of the

CANOPUS network. It has been deduced that the westward electrojet was located poleward of the ISL station and located equatorward of the NAQ Greenland station after onset. Combining these observations constrains the substorm electrojet to the region shown by the shaded area in Figure 5.12. This region was in the pre-midnight sector during this interval of the substorm and extended over 4 hours of magnetic local time.

Prior to substorm expansion phase onset the current densities calculated from the magnetic field measurements at the Cluster spacecraft indicated a value of J_y current around half the probable average in that region. This small value of cross-tail current indicates that the spacecraft were located away from the centre of the plasma sheet. J_y then returned to ~zero a few minutes before onset while the total magnetic field remained constant. This is consistent with the rapid thinning of the current sheet within the plasma sheet during the growth phase of the substorm, leaving the spacecraft located above this thinned current sheet.

At 0251 UT, 1 min after substorm expansion phase onset, the Cluster spacecraft detected a signature not consistent with substorm expansion phase onset in the magnetic field data prior to exiting the plasma sheet to the plasma sheet boundary layer. At onset one would expect to see a classic dipolarization signature for a spacecraft located Earthward of a near-Earth neutral line, with a decrease in the x component of magnetic field and increase in the z component. Here B_x increased very slightly then strongly decreased, and B_z decreased, becoming strongly negative for 7 min. B_x remained reduced when the spacecraft entered the plasma sheet boundary layer, but B_z recovered to its original value of ~ 1 nT. This signature is consistent with the formation of a reconnection site Earthward of the spacecraft, creating a plasmoid whose centre was tailward of the spacecraft which then

At 0300 UT

18 MLT   15 MLT   12 MLT

21 MLT   09 MLT

00 MLT   03 MLT   06 MLT
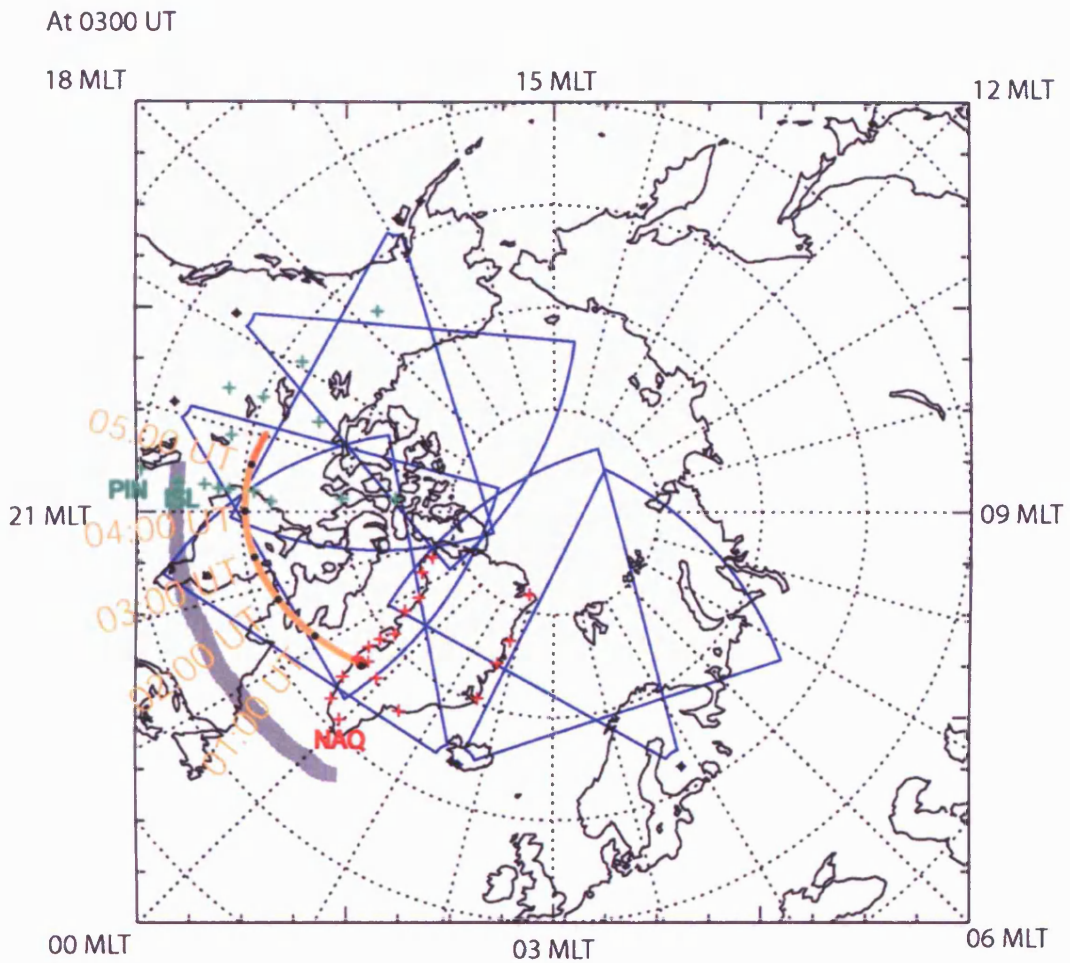
Figure 5.12: Northern hemisphere at 0300 UT on 5 October 2002 in geographic coordinates; shaded area indicates region of substorm electrojet during substorm, from 8 minutes after onset.

formed a TCR, as illustrated in Figure 5.13a. Thus only fields with a negative z component were observed as the TCR formed and then departed tailward. The tailward motion is corroborated by the order in which the spacecraft detected the TCR: the spacecraft farthest downtail, Cluster 4, detected the TCR last. The formation of this plasmoid resulting in a TCR under the spacecraft places the spacecraft tailward of a near-Earth neutral line, and positive B_x confirms that the spacecraft were above the plasma sheet centre, in the PSBL. Analysis of the timings for the peak in B_x, the negative turning of B_z and the peak in B_{total} revealed that the TCR was travelling at ~200 kms^{-1}. This is around one quarter the values described in Slavin et al. (2005), but may be accounted for by the fact that the TCR was still in its early stages of formation. Immediately after the plasmoid departed downtail and B_z returned to small positive values, the spacecraft all detected a decrease in plasma densities and a sustained increase in plasma velocities for up to 10 minutes at Cluster 4. The Cluster 3 spacecraft, located closest to the equatorial plane, detected the weakest beams and smallest decrease in plasma density. This began at 0257 UT, and indicates that the spacecraft entered the PSBL at that time; their location is illustrated in Figure 5.13b. There was therefore a significant time delay (6 min) between the measurement of a negative B_z and the subsequent detection of Earthward flows which is accounted for by this scenario. Figure 5.13c illustrates the departure of the plasmoid downtail. From 0308 UT the beams were tailward and detected mainly by Cluster 1 and 4, indicating that the beams were located only on the outer edge of the plasma sheet and not further into the plasma sheet where the Cluster 3 spacecraft was located. The tailward beams indicate that the spacecraft may have detected PSBL particles that were mirrored at the Earth and returned to the location of the spacecraft during time-dependent behaviour of the plasma sheet, but further study is required to determine whether this is the case. From here the spacecraft exited to the lobe. At 0330 UT, the spacecraft re-entered the plasma sheet from the lobe,

66

a) ~0255 UT

b) ~0300 UT

c) ~0305 UT

✳ = Cluster spacecraft
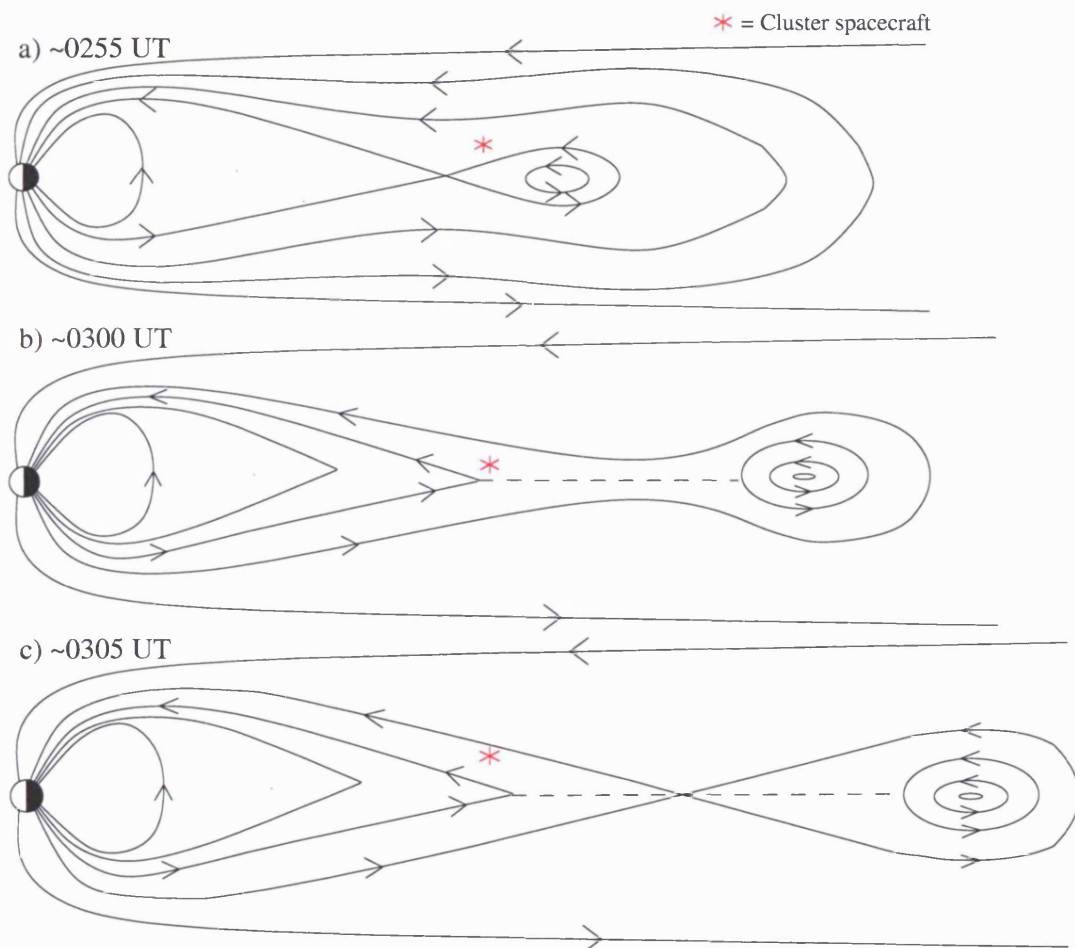
Figure 5.13: a) location of spacecraft within magnetopause around 0255 UT; b) location of spacecraft around 0300 UT; c) location of spacecraft around 0305 UT.

again crossing the PSBL, and detected increased densities and high-speed Earthward plasma beams. Taguchi et al. (1998) examined the midtail lobe TCRs relative to onset during substorm events and interpreted "the flat B_z phase preceding the south tilting interval" in the same way as for this event: "being due to the close proximity to the growing plasmoid bulge just prior to plasmoid ejection down the tail".

At around 0305 UT a large J_x current density, predominantly in the Earthward direction, was detected at the Cluster spacecraft as they left the plasma sheet. A predominantly tailward J_x current density was detected upon re-entry to the plasma sheet at 0330 UT. These currents are due to a difference of the y component of the magnetic field in the z direction, rather than being due to the difference of the z component in the y direction. This suggests that these Earthward- and tailward-directed currents are flowing in a sheet at the boundary of the plasma sheet, in the interface between open and closed field lines. Such sheets of current, having the sense of 'Region 1' field-aligned currents, have been observed in substorm simulations (e.g. Birn and Hesse, 1996), with an explanation which is illustrated in Figure 5.14.

Figure 5.14a shows the x-y plane of the magnetosphere, with open field lines above the plasma sheet depicted by dashed blue lines. The dashed red line in the y direction represents the reconnection line which occupies the central part of the tail, shown symmetric about midnight for the simplest case. The dashed red lines with arrows depict plasma streamlines away from the reconnection line, representing the paths followed by the ends of the newly-reconnected closed field lines. These imply that a V_y velocity component should be present in the downstream flow, carrying the newly-closed field lines away from the reconnection region in the midnight sector towards both dawn and dusk, as

a)

Magnetopause

Open field line

Plasma streamline

Reconnection line

Reconnected field line

x

y

b)

Magnetopause

Lobe

$\otimes$ B

$\odot$ B

PSBL

PS

z

y
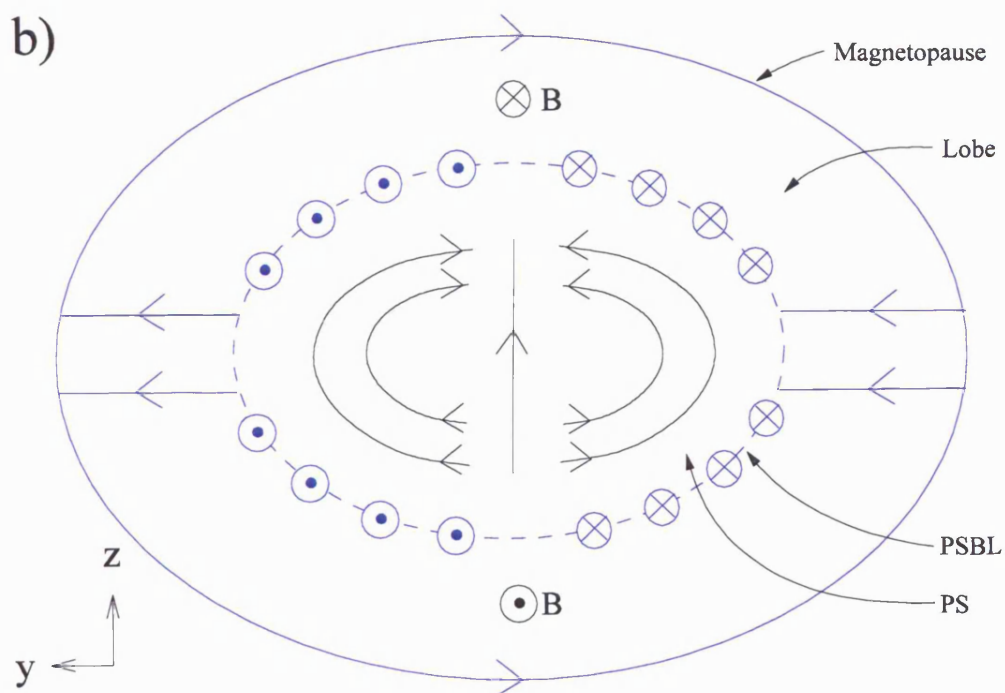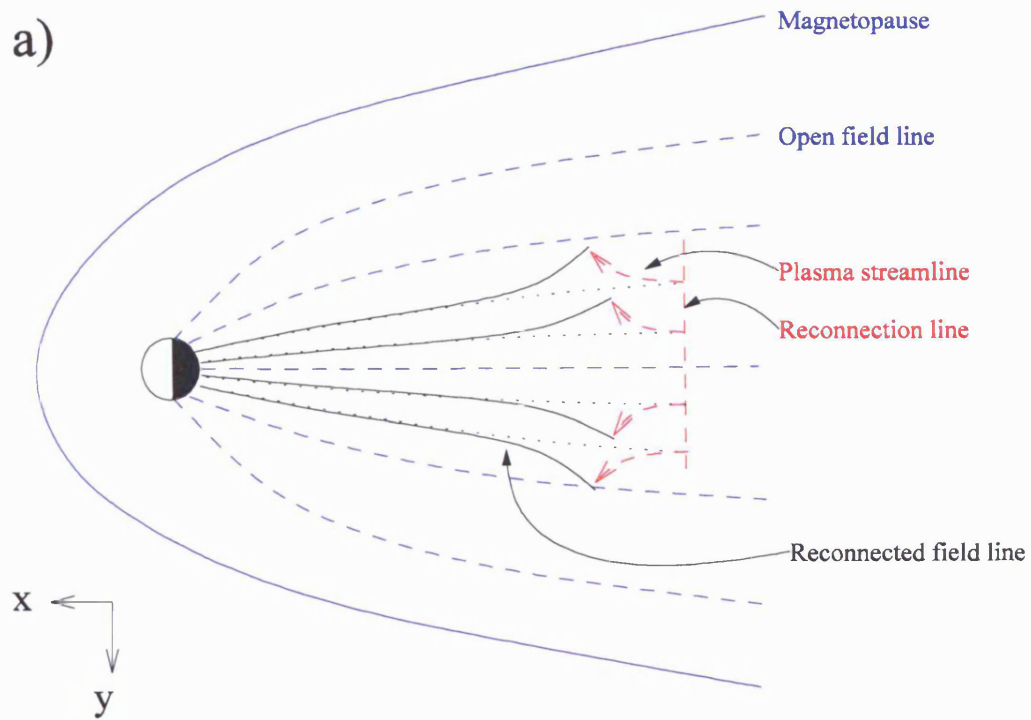
Figure 5.14: a) cut through x-y plane of magnetosphere; b) cut through y-z plane of magnetosphere.

required to distribute the newly-reconnected flux broadly through the closed field region. The dawnward and duskward motion causes the reconnected field lines to twist in direction in the plasma sheet as shown by the black solid lines, the twist in the northern hemisphere being towards dawn on the dusk side, and towards dusk on the dawn side, and vice versa in the southern hemisphere.

The consequent shear in B_y at the surface of the plasma sheet is associated with a field-aligned current directed towards and away from the Earth which has the sense of the 'Region 1' current, i.e. Earthward at dawn, and tailward at dusk. This is shown in Figure 5.14b, where we show a cut through the y-z plane in a region just Earthward of the reconnection line. The pre-existing plasma sheet is located on either side of the lozenge-shaped portion of the recently-reconnected plasma sheet, which is enhanced as a result of the increased flux of closed field lines within it. A projection of these newly-closed field lines onto this cross-section is depicted by the black lines; the shear in the B_y component between plasma sheet and lobe can clearly be seen. This results in the current flow along the surface of the plasma sheet, which is depicted by circled blue crosses (current into the page) and dots (current out of the page). The current system is closed in the ionosphere and on the magnetopause.

At 0305 UT, the Cluster spacecraft were located in the northern boundary of the plasma sheet (B_x is positive) and detected an Earthward current, which places them in the northern, dawnward portion of the scenario presented above. However, the spacecraft were actually located 8 R_E from midnight in the pre-midnight sector, from which we conclude that the reconnection site and consequent current system were skewed to the pre-midnight sector at this time. Previous observations show that substorm onsets are often located in the pre-

midnight sector (e.g. Nagai et al., 1998). The V_y velocities observed by the CIS instrument were indeed mainly negative (i.e. dawnward) during this interval, as then expected (see Figure 5.8). Following this, the spacecraft exit into the lobe. Upon re-entry at 0330 UT, they detect a tailward current in the lobe-plasma sheet boundary, again 8 R_E from midnight. This then places the spacecraft in the northern, duskward portion of the reconnection structure, from which we conclude that the reconnection region and current system had become more centrally-located in the tail by this time, as may be expected. The sense of the V_y flow measured by CIS had also changed to become small but mainly duskward directed.

The question of which substorm onset mechanism is responsible for this substorm event is one that is difficult to resolve. The substorm onset was taken as 0250 UT, the time at which Pi2 pulsations were detected at the PIN magnetometer station located at 21 MLT and the development of a westward electrojet. The westward electrojet subsequently developed at NAQ near midnight a few minutes later. The Pi2 pulsations were simultaneous with a small dipolarisation at the location of the GOES 8 spacecraft in the 22 MLT sector in geostationary orbit, which was followed 5 minutes later by a larger dipolarization. Just one minute after onset at 0251 UT, the Cluster spacecraft detected the formation of a TCR 15 R_E downtail, in the pre-midnight sector. At the same time there was an electron injection detected by the LANL-01A spacecraft, in the 4 MLT sector in geostationary orbit. These signatures were detected at very widely spaced locations in the magnetotail, and since they all occurred within just one minute of each other it is not possible to distinguish the location of initial onset for this substorm. Furthermore, the large local time extent of this event suggests that this was the onset of the full expansion phase rather than a spatially localized pseudobreakup.

It is worth noting that there was a further intensification of this substorm at ~0315 UT detected by the ISL and PIN magnetometer stations. There was also a dipolarization at geostationary orbit detected by the GOES spacecraft at this time, and this is also related to the intensifications of ionospheric flow out of the polar cap depicted in the map potential plot for 0314 to 0316 UT (Figure 5.3b). The Cluster spacecraft were located in the lobe at this time, and no dipolarization was detected at their location.

5.4 Summary and Conclusions

In this chapter we have brought together several data sets which give a good overview of the conditions in the ionosphere, near-magnetosphere and magnetosphere during a substorm event on 5 October 2002. Despite not resolving the question of which mechanism was responsible for the substorm onset in this case, many other interesting findings have been presented. The magnetometer data set determines the time of onset as 0250 UT; the time when Pi2 pulsations were first detected for this substorm. The location of the substorm electrojet is constrained using the magnetometer data, and LANL particle data infer the time at which plasma were injected at geosynchronous orbit. A small J_y current detected before onset is lost a few minutes prior to onset. This indicates that the spacecraft detected the rapid thinning of the plasma sheet under the spacecraft prior to onset, i.e. during the growth phase. The negative z component of the magnetic field at substorm onset coupled with a large time delay before detection of Earthward flows is most easily explained by the formation of a tailward-moving plasmoid, producing a TCR at onset. The near-Earth neutral line therefore formed somewhere Earthward of the Cluster spacecraft at

their location of ~15 R_E downtail. Importantly, the Cluster spacecraft detected Region 1 currents during this interval flowing at the surface of the plasma sheet. In contrast to the usual SCW picture, these Region 1 currents were associated mainly with B_y varying in the z direction, rather than B_z varying in the y direction. Initially these currents were predominantly Earthward-directed as the spacecraft left the plasma sheet, then later were tailward-directed as the spacecraft re-entered the plasma sheet. These findings indicate that the Region 1 currents were initially skewed towards the pre-midnight sector, and later became more centrally-located about the midnight sector. This is consistent with previous findings that place substorm onset in the pre-midnight sector of the magnetotail.

Chapter 6

Cluster observations of magnetic field cavities

Following the work presented in Chapter 4, the new magnetic cavity feature discovered in the interval on 1st September 2002 is investigated in more detail. Since this appears to be a new feature, a survey was undertaken to identify other potential magnetic cavity candidates to ascertain whether or not this was a singular event. Three of these candidates have been selected for further study. The findings for the four events are presented and potential explanations for these magnetic cavities are discussed.

6.1 Introduction

During the recovery phase of a substorm occurring on 1st September 2002 the four Cluster spacecraft crossed from the northern tail lobe into the plasma sheet (at 1903 UT; see Figure 6.1). While the spacecraft were located in the plasma sheet boundary layer, the magnetic field data from the four spacecraft detected a magnetic cavity, of close to zero magnetic field. During summer 2002 the orbits of the Cluster spacecraft were optimized for data collection in the Earth's magnetotail, passing at regular intervals from the northern lobe, through the plasma sheet, and into the southern lobe. Their separation while in the magnetotail was consistently around 4000 km. The tetrahedral formation of the spacecraft allows full temporal and spatial analysis of the data that are collected, revealing far more
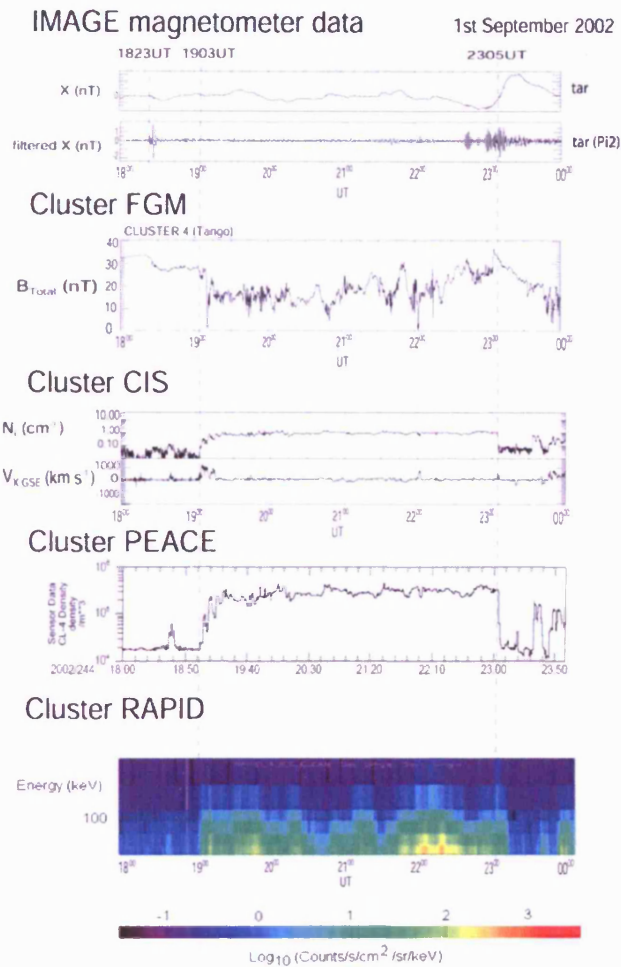
Figure 6.1: IMAGE magnetometer data and Cluster particle data for 1 September 2002 (1800 to 2400 UT). Top two panels show the X component of magnetic field at the Tartu (Tar) IMAGE magnetometer station, and the filtered X component at the same station (filter range is in the period band 20 - 200 s). The third panel shows the total magnetic field data from FGM instrument on the Cluster 4 spacecraft. The fourth and fifth panels show the density and x component of velocity of the low-energy ions (0.02 eV to 30 keV) from the CIS instrument on the Cluster 4 spacecraft. The sixth panel shows the density of the low-energy electrons (0.7 eV to 30 keV) from the PEACE instrument on the Cluster 4 spacecraft. The seventh panel shows the electron density of the high-energy electrons (20 to 400 keV) from the RAPID IES instrument on the Cluster 4 spacecraft.

information than from a single spacecraft describing a similar orbit. The analysis is based on data from the FGM, CIS, PEACE and RAPID instruments on board the Cluster spacecraft. Data from the Tartu (Tar) station of the IMAGE ground magnetometer network (Viljanen and Häkkinen, 1997) are also presented. This station is located at 58.26° geographic latitude and 26.46° geographic longitude

The discovery of the new magnetic cavity feature prompted a survey of Cluster FGM data to search for similar events. Cluster FGM data from 2002, 2003 and 2004 were searched for instances when the Cluster spacecraft were located in the region of the plasma sheet, and for which the total magnetic field was in the range $0 \text{ nT} < B_{total} < 5 \text{ nT}$. This inevitably selected events which were due to current sheet crossings, and so inspection by eye was used to eliminate those events. Cluster orbit plots were then produced to eliminate those events which were located in the flanks of the magnetotail, towards the magnetosheath, in order to ensure that the selected events were located in or around the region of the plasma sheet, as for the first event. Cluster CIS data were plotted and used to produce plasma beta plots in order to determine the plasma regime in which the Cluster spacecraft were located for each potential event; the plasma sheet, the plasma sheet boundary layer or one of the lobes. Unfortunately no CIS data were available for 2004. This brought the final number of potential candidates to 10, which included the original 1st September 2002 event. It is worth noting that ten events were identified, over a time of approximately 6 months. The orbital period of the spacecraft is 57 hours, hence they cross the magnetotail once every two and a half days or so. Over 6 months they therefore make ~75 magnetotail crossings, implying that magnetic cavities were detected for 13 % of the tail crossings.

Of the three events chosen for further study one occurred on 13th September 2002 (2252

73

UT), one on 25th September 2002 (2234 UT) and one on 12th September 2003 (2105 UT). These events provided a good selection of data similar to that of the first event from which to work from, with few data gaps. The events are from two different years, allowing comparison of cavity events detected by Cluster whilst the spacecraft were at different separations in their tetrahedral configuration (~ 4000 km in 2002 and ~ 500 km in 2003).

6.2 Data and Observations

6.2.1 Background to the first magnetic cavity event

Figure 6.1 shows IMAGE magnetometer data and Cluster particle data for the 1800 UT to 2400 UT interval on 1st September 2002. Top two panels show the X component of magnetic field at Tartu, and its filtered X component (filter range is in the period band 20 - 200 s). The third panel shows B_{total} from FGM instrument on the Cluster 4 spacecraft. The fourth and fifth panels show the density and x component of velocity of the low-energy ions (0.02 eV to 30 keV) from the CIS instrument on Cluster 4. The sixth panel shows the density of the low-energy electrons (0.7 eV to 30 keV) from the PEACE instrument on the same spacecraft. The seventh panel shows the electron density of the high-energy electrons (20 to 400 keV) from the RAPID IES instrument, also from the Cluster 4 spacecraft.

At ~1900 UT the magnetosphere was in the recovery phase of a substorm that occurred at 1823 UT, detected as a decrease in the X component at the Tartu station and evidence for Pi2 activity at onset, as described in Chapter 4. Particle data from the Cluster instruments indicate that the Cluster spacecraft were initially located in the lobe. They passed through

74

the plasma sheet boundary layer and entered into the plasma sheet at 1903 UT. The CIS instrument on Cluster 4 detected a sudden increase in ion density from ~0.01 cm^{-3} in the lobe to ~1 cm^{-3} in the plasma sheet, accompanied by velocity bursts to ~1000 km s^{-1} in the V_x component (parallel to the magnetic field), which is typical of plasma sheet boundary layer beams. The PEACE and RAPID instruments on Cluster 4 also detected corresponding increases in the low- and high-energy electron fluxes, respectively, as the spacecraft entered the plasma sheet. At the time of the second substorm, 2305 UT, the Cluster spacecraft re-entered the lobe due to the dipolarisation of the magnetotail at substorm expansion phase onset. A more detailed analysis of these two substorms was given in Chapter 4 (see also Draper et al., 2004).

6.2.2 Cluster location and FGM data

Figure 6.2 (1st September 2002), Figure 6.3 (13th September 2002), Figure 6.4 (25th September 2002) and Figure 6.5 (12th September 2003) show the location of the Cluster spacecraft in the X-Z and X-Y planes in geocentric solar magnetospheric (GSM) coordinates for each of the cavity events. Cluster 1 (Rumba) is blue, Cluster 2 (Salsa) is green, Cluster 3 (Samba) is yellow, and Cluster 4 (Tango) is red. The dotted lines depict model magnetic field lines using the Tsyganenko 1996 model (Tsyganenko and Stern, 1996). The FGM data for ten minutes around each of the four events are presented in Figures 6.6 to 6.9. The first four panels of each present the B_x, B_y and B_z components of magnetic field and the total magnetic field, the fifth panel presents the clock angle (the clockwise angle of the magnetic field from positive z in the y-z plane as viewed from the sun, in degrees), and the bottom panel presents a zoomed view of the magnetic field minimum. Figure 6.10 is a table summarizing the locations and findings from the FGM
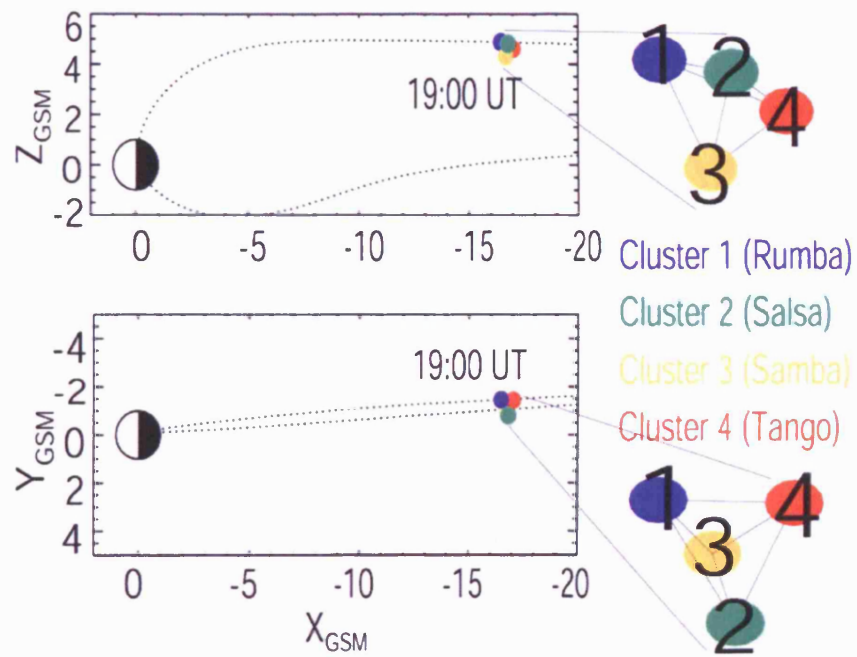
Figure 6.2: Cluster spacecraft positions at 1900 UT on 1 September 2002, shown projected into the X-Z and X-Y planes in geocentric solar magnetospheric (GSM) coordinates, with the relative orientation of the spacecraft in each plane to the right of each panel. Blue represents Cluster 1 (Rumba), green Cluster 2 (Salsa), yellow Cluster 3 (Samba) and red Cluster 4 (Tango). Dotted lines depict the model magnetic field.

Cluster tetrahedron

20020913

23:00 UT
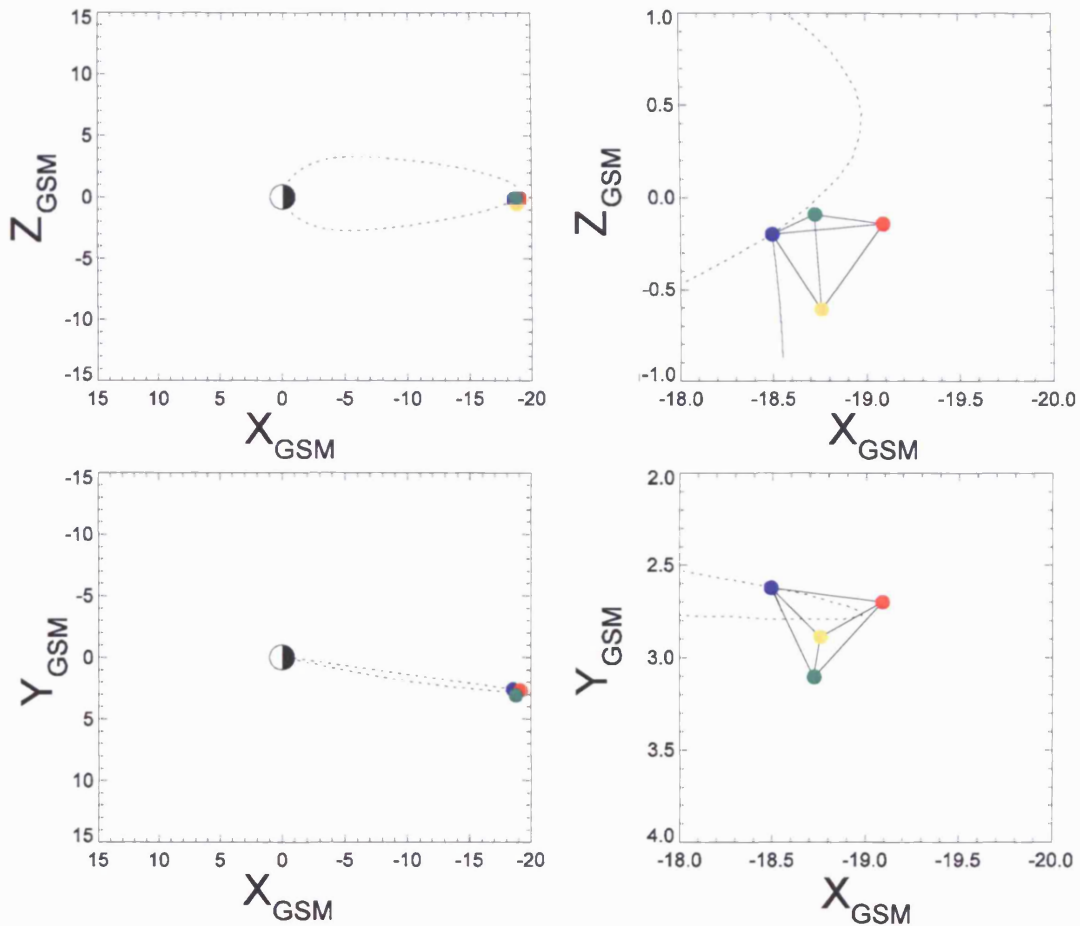
Figure 6.3: Cluster spacecraft positions at 2300 UT on 13 September 2002, shown projected into the X-Z and X-Y planes in geocentric solar magnetospheric (GSM) coordinates. Blue represents Cluster 1 (Rumba), green Cluster 2 (Salsa), yellow Cluster 3 (Samba) and red Cluster 4 (Tango). Dotted lines depict the model magnetic field. Solid lines depict tetrahedron and its orbit for the following hour.

Cluster tetrahedron   **20020925**
22:00 UT
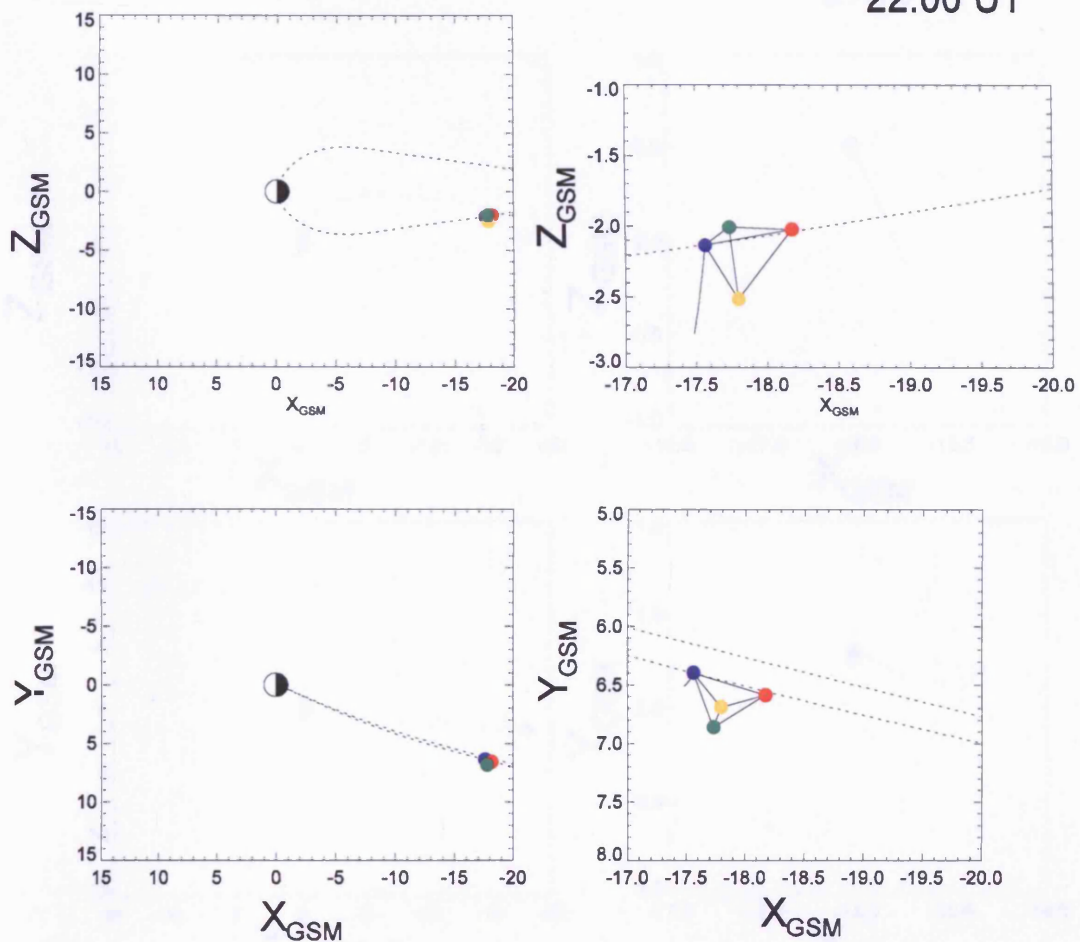
Figure 6.4: Cluster spacecraft positions at 2200 UT on 25 September 2002, shown projected into the X-Z and X-Y planes in geocentric solar magnetospheric (GSM) coordinates. Blue represents Cluster 1 (Rumba), green Cluster 2 (Salsa), yellow Cluster 3 (Samba) and red Cluster 4 (Tango). Dotted lines depict the model magnetic field. Solid lines depict tetrahedron and its orbit for the following hour.
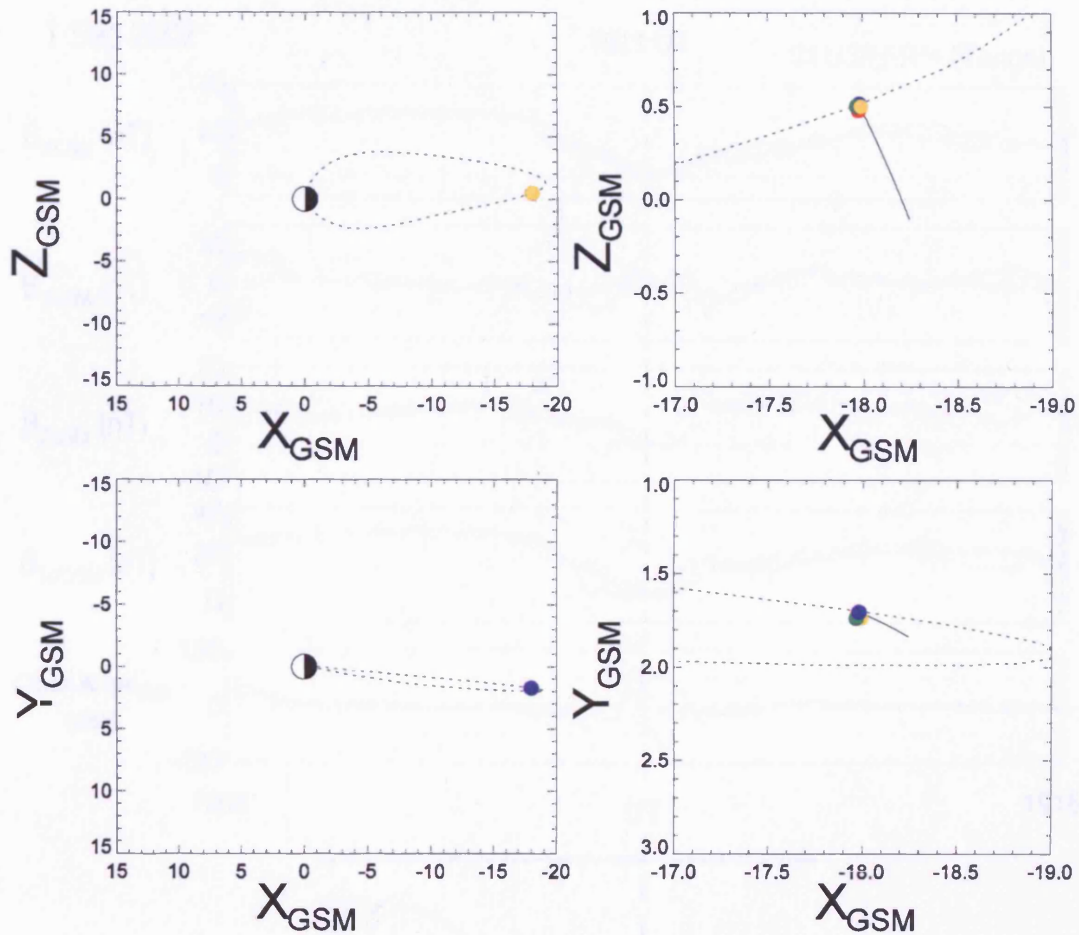
Figure 6.5: Cluster spacecraft positions at 2100 UT on 12 September 2003, shown projected into the X-Z and X-Y planes in geocentric solar magnetospheric (GSM) coordinates. Blue represents Cluster 1 (Rumba), green Cluster 2 (Salsa), yellow Cluster 3 (Samba) and red Cluster 4 (Tango). Dotted lines depict the model magnetic field. Solid lines depict tetrahedron and its orbit for the following hour.
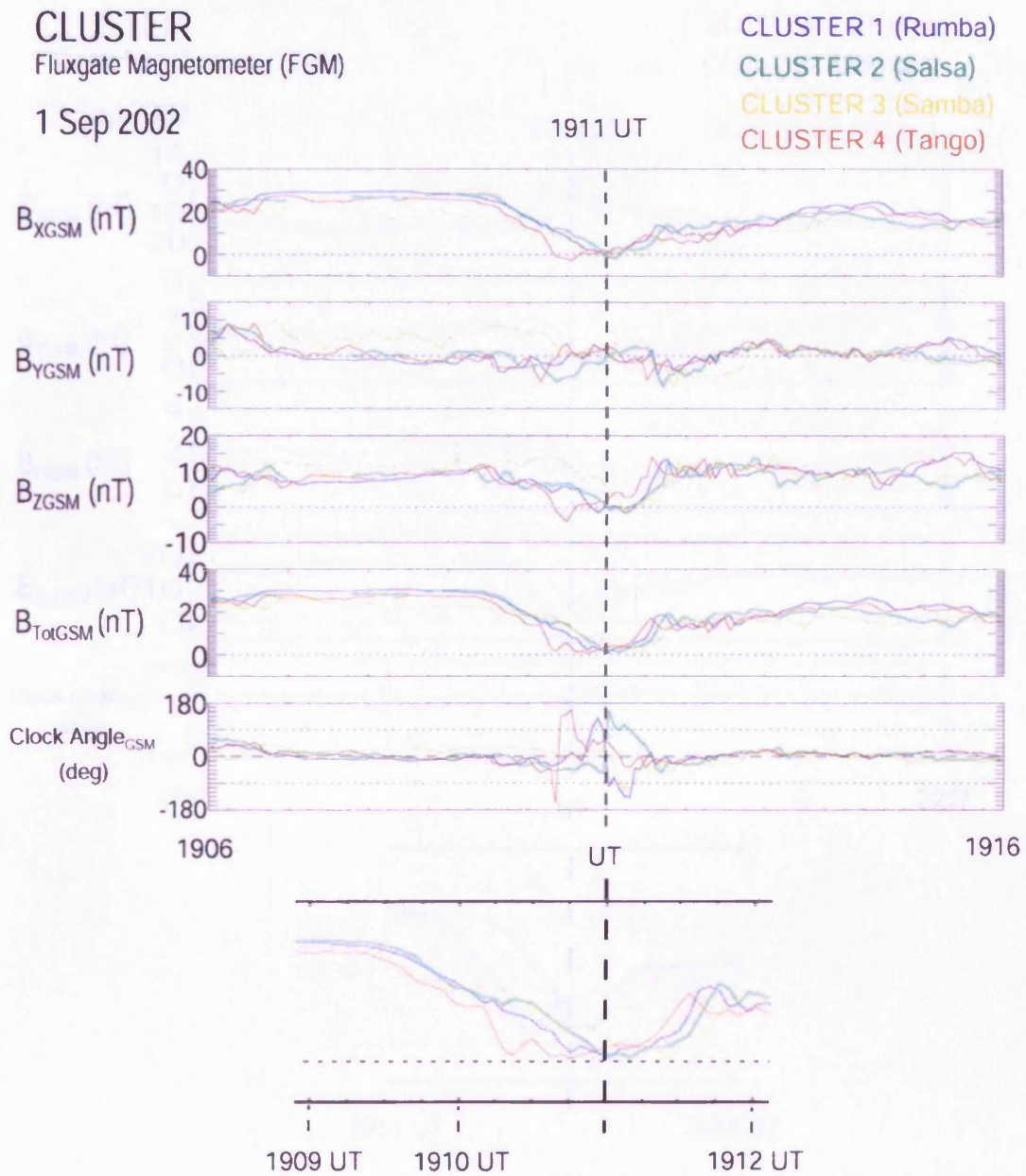
Figure 6.6: Cluster FGM data for 1 September 2002, from 1906 UT to 1916 UT. The B_x, B_y and B_z components, the total magnetic field and the clock angle (the clockwise angle of the magnetic field from positive z in the y-z plane as viewed from the sun) are shown in GSM coordinates. The total field strength is shown on an expanded scale at the bottom of the Figure centred on the field null at 1911 UT.
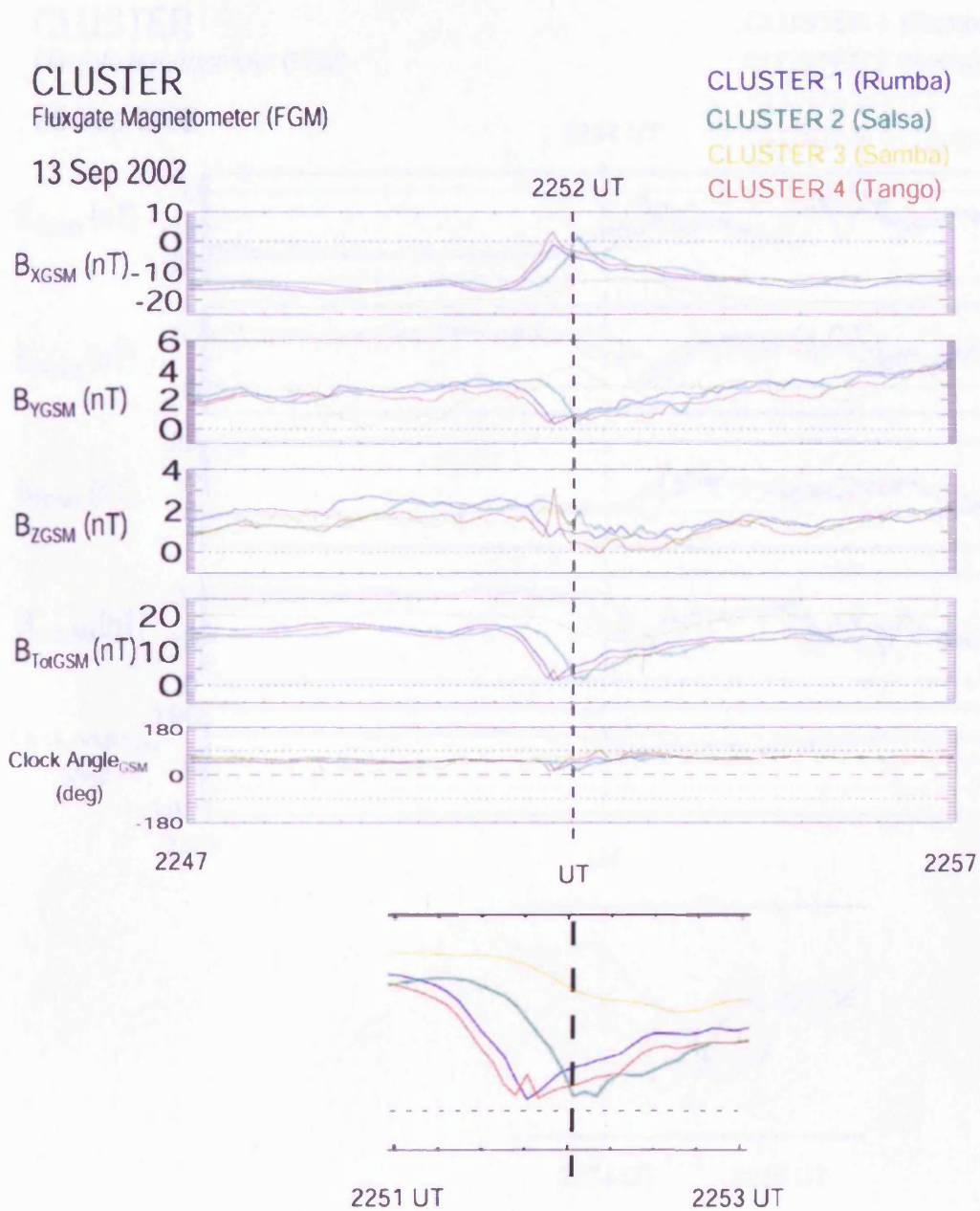
Figure 6.7: Cluster FGM data for 13 September 2002, from 2247 UT to 2257 UT. The B_x, B_y and B_z components, the total magnetic field and the clock angle (the clockwise angle of the magnetic field from positive z in the y-z plane as viewed from the sun) are shown in GSM coordinates. The total field strength is shown on an expanded scale at the bottom of the Figure centred on the field null at 2252 UT.

CLUSTER
Fluxgate Magnetometer (FGM)

25 Sep 2002

CLUSTER 1 (Rumba)
CLUSTER 2 (Salsa)
CLUSTER 3 (Samba)
CLUSTER 4 (Tango)
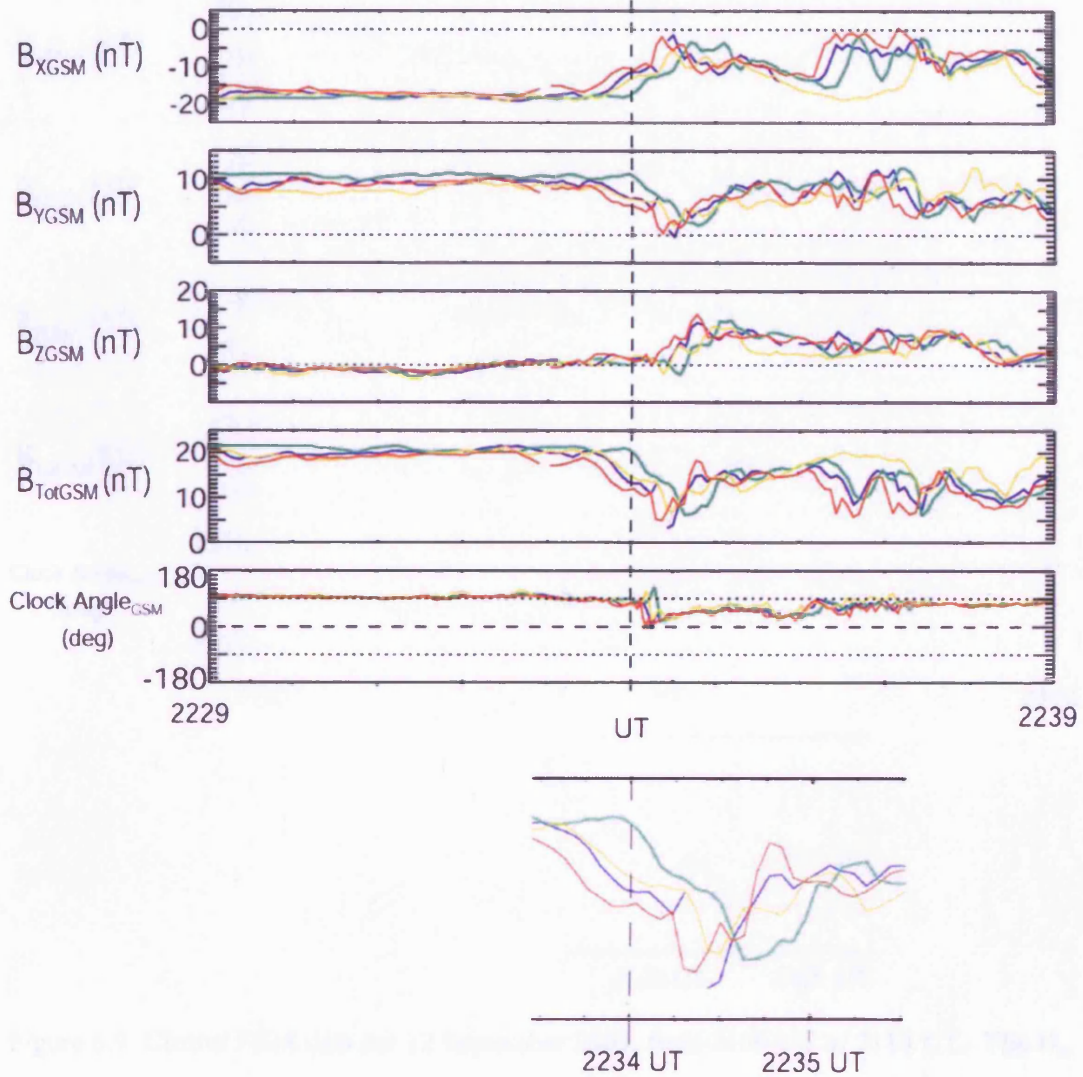
Figure 6.8: Cluster FGM data for 25th September 2002, from 2229 UT to 2239 UT. The B_x, B_y and B_z components, the total magnetic field and the clock angle (the clockwise angle of the magnetic field from positive z in the y-z plane as viewed from the sun) are shown in GSM coordinates. The total field strength is shown on an expanded scale at the bottom of the Figure centred on the field null at 2234 UT.
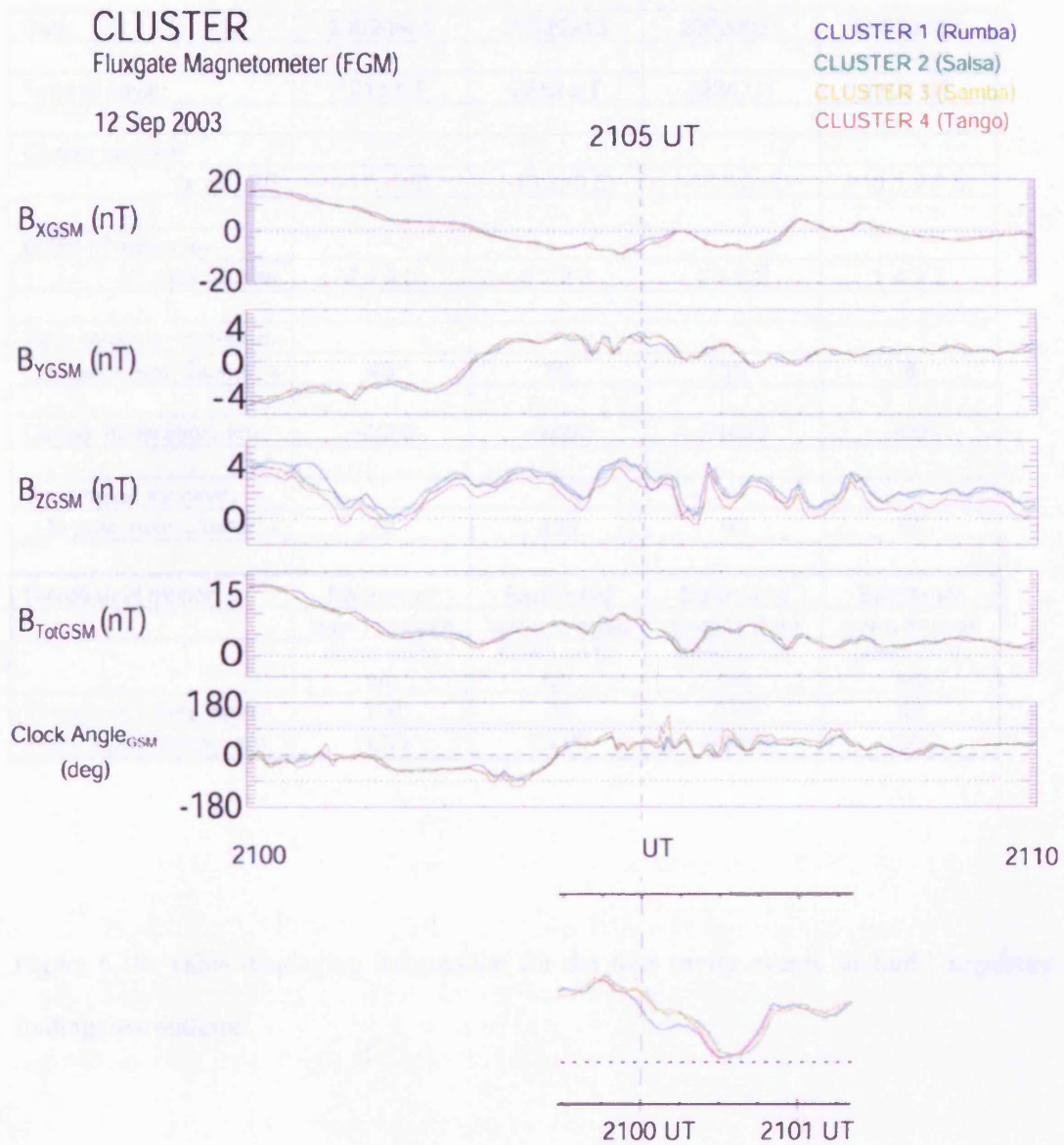
Figure 6.9: Cluster FGM data for 12 September 2003, from 2100 UT to 2110 UT. The B_x, B_y and B_z components, the total magnetic field and the clock angle (the clockwise angle of the magnetic field from positive z in the y-z plane as viewed from the sun) are shown in GSM coordinates. The total field strength is shown on an expanded scale at the bottom of the Figure centred on the field null at 2105 UT.

| Date	20020901	20020913	20020925	20030912
Time of cavity	1911 UT	2252 UT	2234 UT	2105 UT
Cluster location (x,y,z) RE	(-17,-1,5)	(-19,3,-0.5)	(-18,6.5,-2)	(-18,1.7,0.5)
Order of minimum over Cluster	4 1 2 3	4 1 2 3	4 1 3 2	1 4 3 2
Time taken for minimum to pass over Cluster, s	40	55	15	8
Cluster separation, km	~4000	~4000	~4000	~500
Time taken for cavity to pass over Cluster, s	70	180	90	65
Direction of motion	Earthward dawn to dusk down on to s/c	Earthward dawn to dusk down on to s/c	Earthward dawn to dusk down on to s/c	Earthward dawn to dusk down on to s/c
Velocity of cavity, km/s	100	70	270	60
Scale size of cavity, km	7000	13000	24000	4000

Figure 6.10: Table displaying information for the four cavity events studied. Important findings are outlined.

data, described below.

The spacecraft are located between 17 and 19 R_E downtail for the four cavity events, within 6.5 R_E of midnight (three in the pre-midnight sector and one post-midnight) and within 5 R_E of the equatorial plane (two above and two below).

The total magnetic field (fourth panel of Figures 6.6 to 6.9) displayed a clear decrease and recovery for each cavity event. In each case the minimum of B_z encountered the Cluster spacecraft in a clearly defined order. The signatures from the four spacecraft were not nested. Analysis of the order in which the minimum magnetic field encountered the spacecraft indicated that in every case the cavity was moving Earthwards, from dawn to dusk and down on to the spacecraft. The time between detection of the minimum by the first spacecraft encountered and the last spacecraft encountered, together with the spacecraft separation, were used to calculate the order-of-magnitude velocity for the cavities of 100 km s^{-1}, 70 km s^{-1}, 270 km s^{-1} and 60 km s^{-1} respectively. Combining this velocity with the time taken for the cavity to pass completely over the spacecraft, that is the time between the start of the decrease in magnetic field and its recovery, provided scale sizes in the direction of propagation for the cavities of 7000 km, 13000 km, 24000 km and 4000 km respectively (assuming that the spacecraft are detecting a good proportion of the cavities rather than a small section through them).

The clock angle (fifth panel of Figures 6.6 to 6.9) displays interesting features at the time of each of the cavity events. For the first event, Cluster 4 detected an anticlockwise then clockwise turning, followed by Cluster 1 which detected a clockwise then anticlockwise turning, followed by Cluster 2 which detected a clockwise turning and finally Cluster 3

which detected an anticlockwise turning. These turnings were large; $\sim 120\ ^\circ$ in each case. The second cavity displayed a small anticlockwise turning ($\sim 30\ ^\circ$) at Cluster 4 followed by Cluster 1 then Cluster 2. Cluster 3 did not detect this signature, but neither did it detect as pronounced a decrease in the total magnetic field. The third cavity event displayed clockwise then anticlockwise turnings simultaneously at Cluster 2, 3 and 4 of up to $\sim 90\ ^\circ$, and also an anticlockwise turning only by Cluster 1 at the same time. The fourth event displayed anticlockwise turnings at Cluster 3 and 4 of up to $90\ ^\circ$, although there were more fluctuations of the clock angle during this interval than for any of the other events. In each case the clock angle recovered to approximately its initial value after the cavity event had passed.

Data from the IMAGE magnetometer stations (not shown) were used as an indication for substorm activity around the cavity events. The first event occurred ~ 50 minutes after a substorm onset, whilst the magnetosphere was in the recovery phase of a substorm. For the second event there was evidence of substorm activity in the IMAGE magnetometer data at stations between ~ 67 - $70\ ^\circ$ geographic latitude ~ 5 hours before the event, and an intensification ~ 20 minutes before. However these magnetometers were located in the midnight sector at 2252 UT and hence were located at a slightly different local time from that of the Cluster footprint. There is possible evidence for a small substorm or pseudobreakup at ~ 90 minutes before the third event in the IMAGE magnetometer data at stations between ~ 70 - $75\ ^\circ$ geographic latitude, although these were located in the midnight sector at 2234 UT which, as for the previous event, was a slightly different local time from that of the Cluster footprint. There was evidence for a small substorm or pseudobreakup in the IMAGE magnetometer data ~ 65 minutes before the fourth event, at stations between ~ 69 - $70\ ^\circ$ geographic latitude.

6.2.3 Cluster CIS data

The CIS plasma data (number density and plasma velocity V_x, V_y and V_z) and plasma beta from Cluster 1, 3 and 4 for each interval are presented in Figure 6.11 (1st September 2002), Figure 6.13 (13th September 2002), Figure 6.14 (25th September 2002) and Figure 6.15 (12th September 2003). Figure 6.12 is intended to clarify the first event by presenting CODIF and HIA data from the CIS instrument on Cluster 1 for the 1900 to 1920 UT interval on 1st September 2002, with Cluster FGM data for comparison.

The first cavity event occurred when the Cluster spacecraft were located in the plasma sheet boundary layer. This is more clearly shown in Figure 6.12. The plasma sheet boundary layer beams are detected as increased velocities (panel 3, CODIF and panel 5, HIA), high energy densities (panel 4, CODIF and panel 7, HIA) and increased temperature (panel 6, HIA). However, at ~1911 UT corresponding to the field cavity the velocities decreased to close to zero. This coincided with a high isotropic temperature (~5 keV) and enhanced energy density in the 1 to 10 keV energy range, detected at both the CODIF and HIA instruments.

The ion number densities for the second cavity event are ~0.1 cm^{-3} indicating that the Cluster spacecraft are located in the plasma sheet. This is corroborated by the plasma beta value which is ~1 during this interval at Cluster 1 and 4 and ~0.3 at Cluster 3, and there are no significant flows in the plasma velocities around 2252 UT.

The third cavity event was also located in the plasma sheet, with ion number densities of
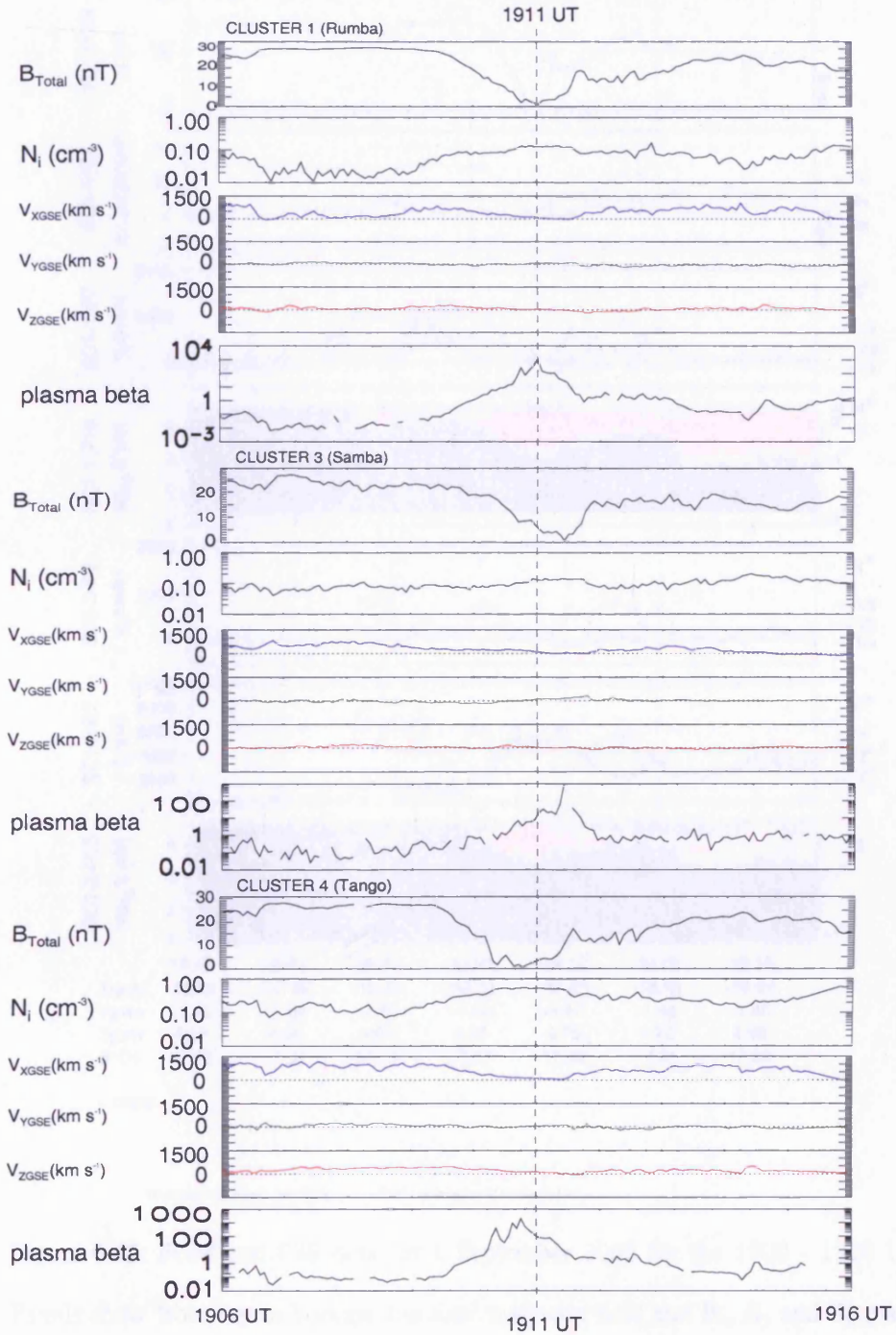
Figure 6.11: Cluster CIS data for 1 September 2002, from 1906 UT to 1916 UT. Number density, V_x, V_y and V_z and plasma beta are shown for Cluster 1, 3 and 4.
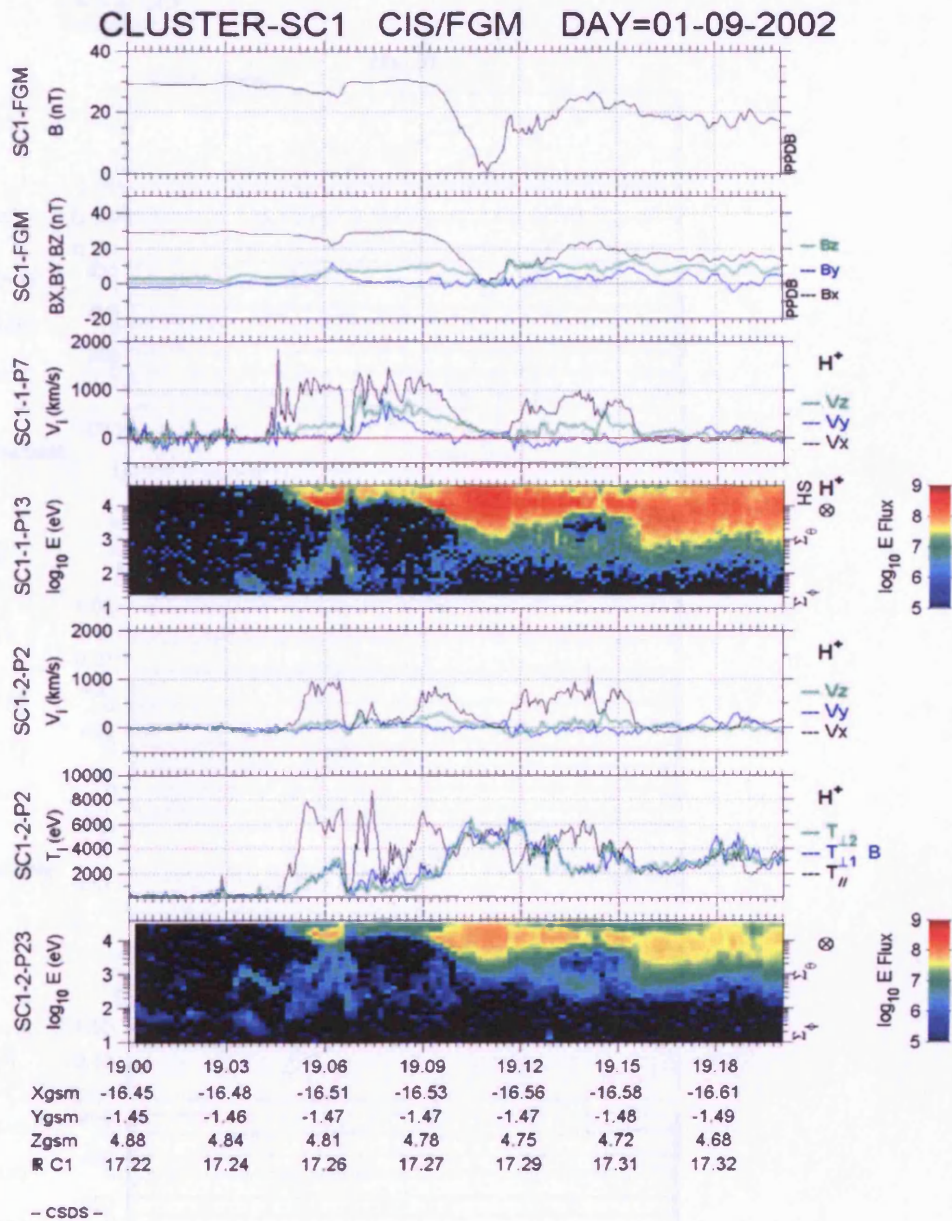
Figure 6.12: FGM and CIS data for 1 September 2002 for the 1900 - 1920 UT interval. Panels show from top to bottom, the total magnetic field and B_x, B_y and B_z magnetic field components, the velocity components and energy density for CIS1 (CODIF) and the velocity, temperature and energy density for CIS2 (HIA).
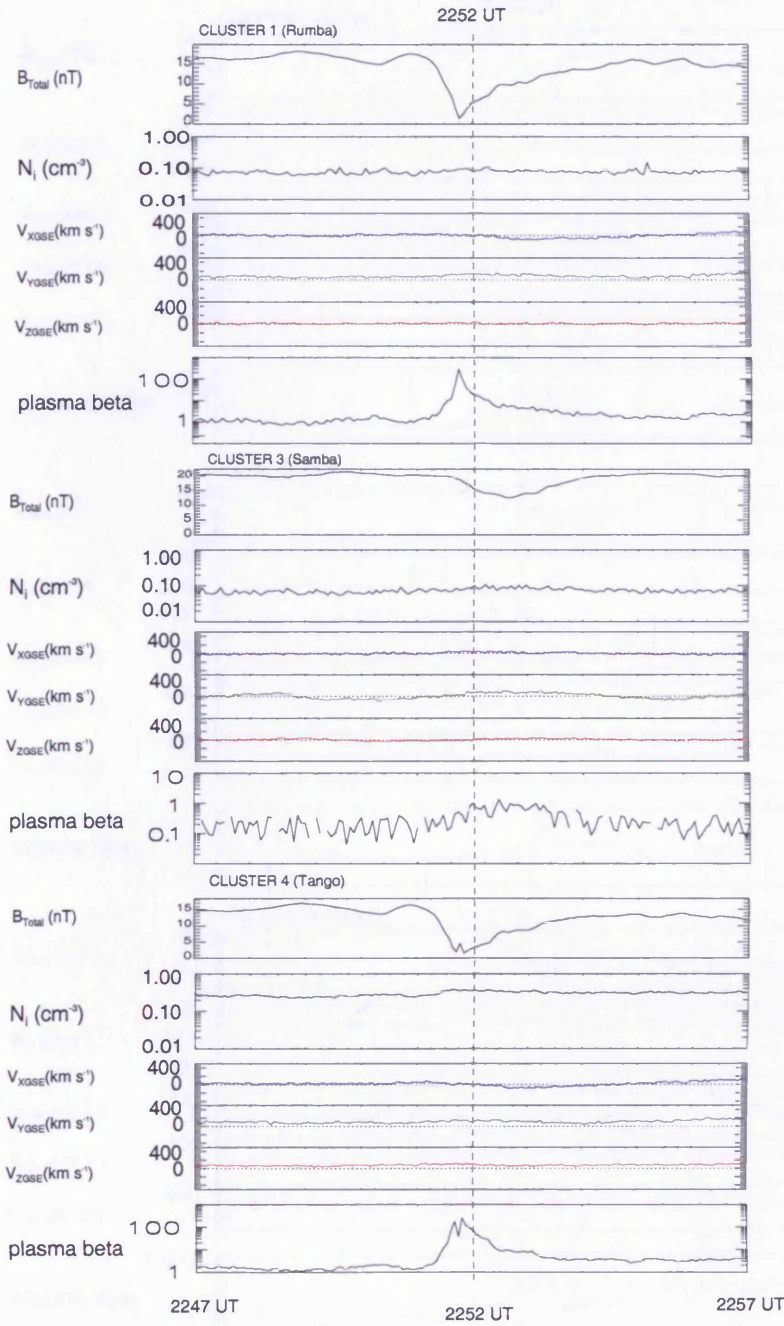
Figure 6.13: Cluster CIS data for 13 September 2002, from 2247 UT to 2257 UT. Number density, V_x, V_y and V_z and plasma beta are shown for Cluster 1, 3 and 4.
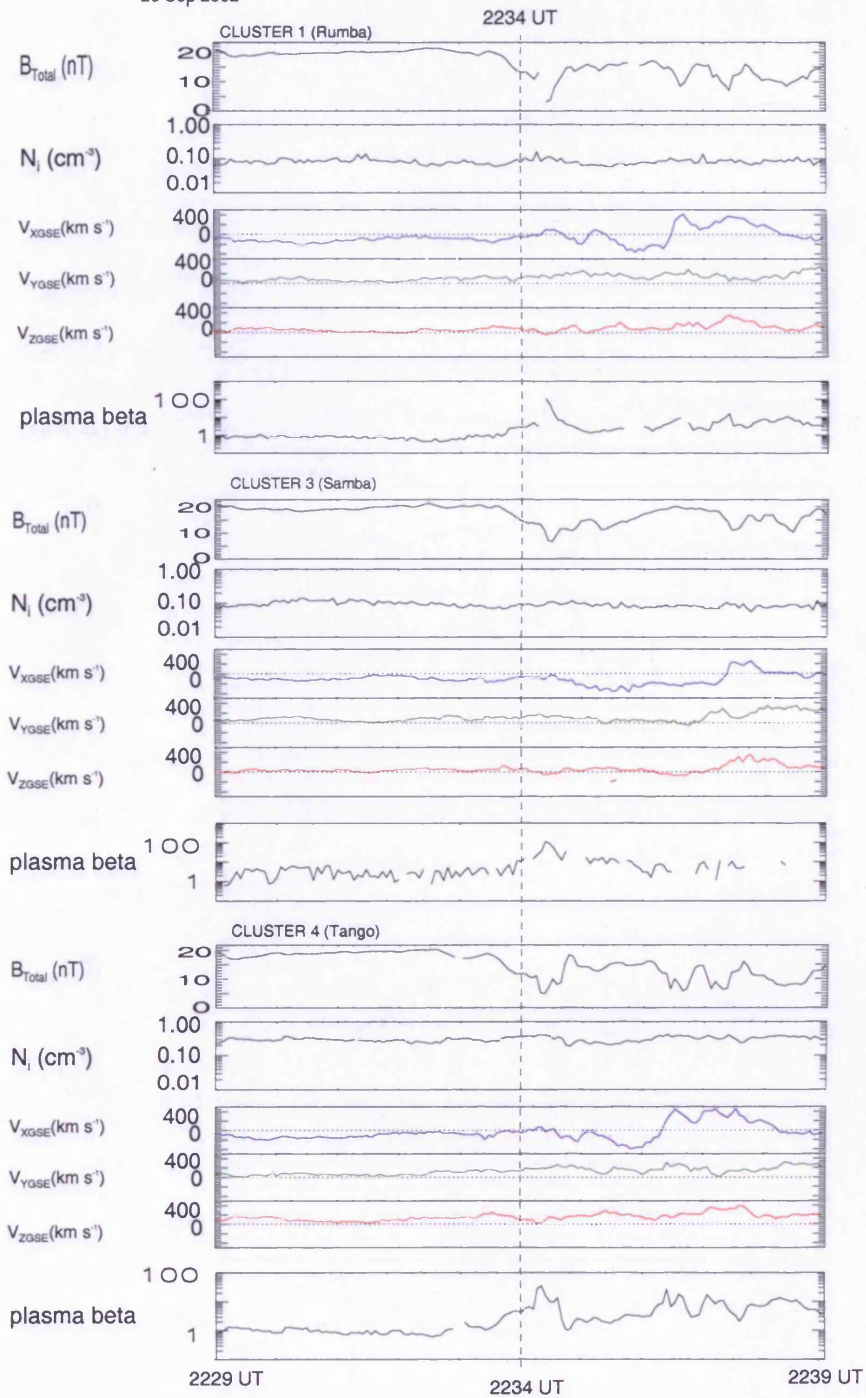
Figure 6.14: Cluster CIS data for 25th September 2002, from 2229 UT to 2239 UT.

Number density, V_x, V_y and V_z and plasma beta are shown for Cluster 1, 3 and 4.
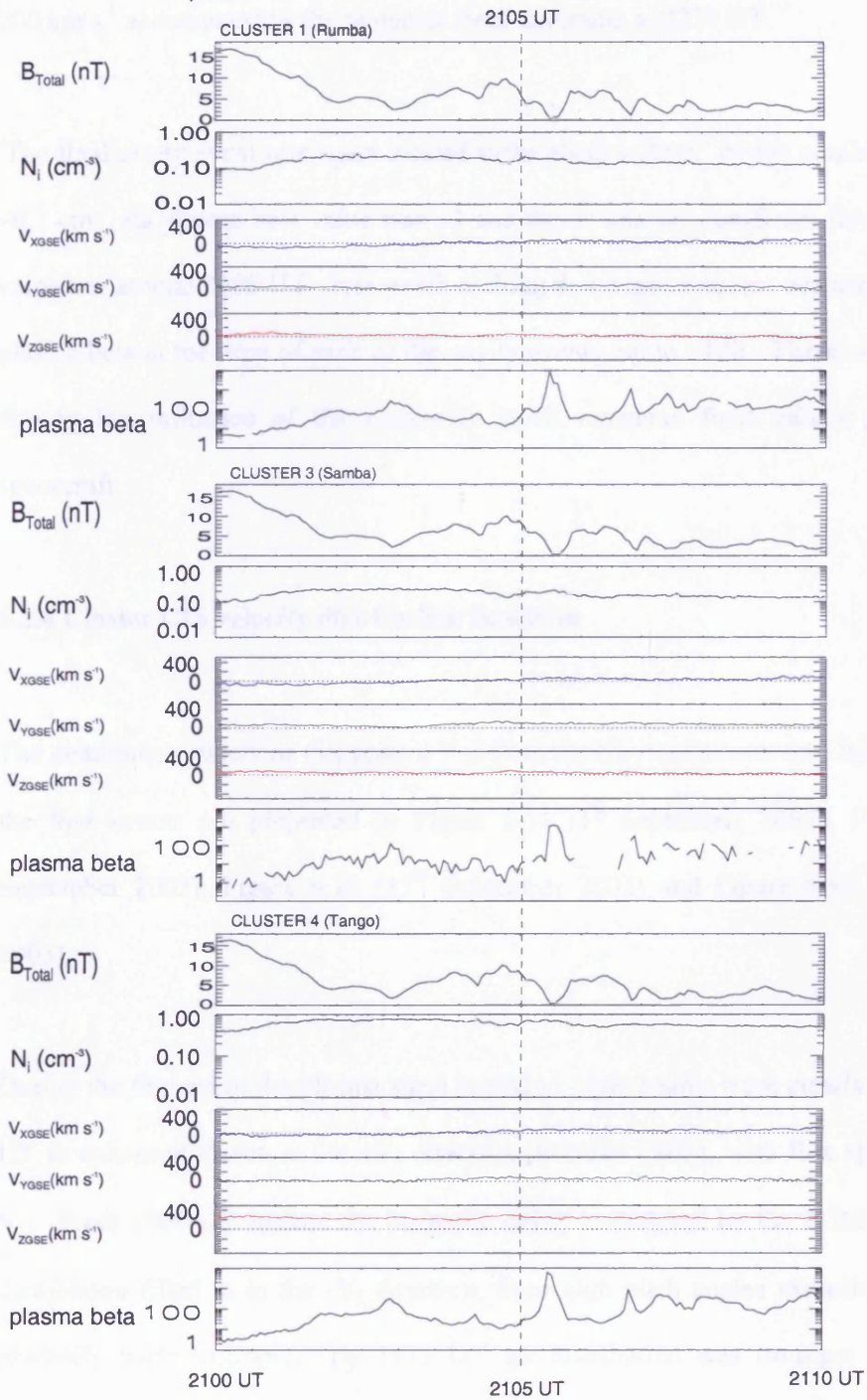
Figure 6.15: Cluster CIS data for 12 September 2003, from 2100 UT to 2110 UT. Number density, V_x, V_y and V_z and plasma beta are shown for Cluster 1, 3 and 4.

~0.1 cm^{-3} detected, a plasma beta value of ~1, and small enhancements in V_x of up to ~ -200 km s^{-1} accompanying the magnetic field minimum at 2234 UT.

The final cavity event was again located in the plasma sheet. Its ion number densities were ~0.1 cm^{-3}, its plasma beta value was ~1 and there were no significant flows in the plasma velocities around 2105 UT. It is worth nothing that huge increases occurred in the value of plasma beta at the time of each of the cavity events, up to ~100. These are predominantly due to the influence of the extremely small magnetic field values present at these spacecraft.

6.2.4 Cluster CIS velocity distribution functions

The distribution functions ($V_{\parallel}$ against $V_{\perp}$) from the HIA instrument on Cluster 1 for each of the four events are presented in Figure 6.16 (1st September 2002), Figure 6.17 (13th September 2002), Figure 6.18 (25th September 2002) and Figure 6.19 (12th September 2003).

During the first event the plasma sheet boundary layer beams were clearly seen from 1904 UT as enhanced fluxes in the +$V_{\parallel}$ direction (towards Earth), with flux spread about zero $V_{\perp}$. From 1909 UT (before the magnetic cavity is detected by the FGM instrument) the distribution filled in in the -$V_{\parallel}$ direction, from high pitch angles towards low, becoming gradually more isotropic. By 1911 UT the distribution was isotropic with very slow velocities, and looked like a typical central plasma sheet distribution. The distribution then returned to plasma sheet boundary layer beams, with evidence for mirrored particles, as
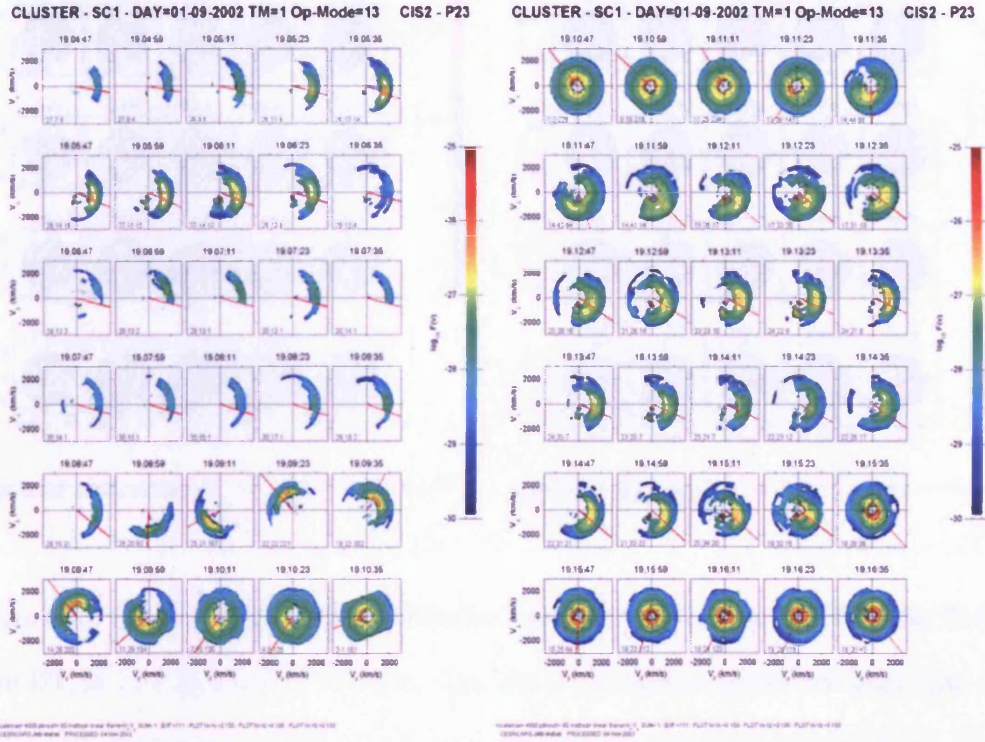
Figure 6.16: Cluster 1 CIS2 (HIA) distribution functions for 1 September 2002 for 1904 to 1916 UT, at 12 s intervals (read left to right and top to bottom across left page first, then right page). Each panel shows $V_{\parallel}$ on the x axis against $V_{\perp}$ on the y axis; the red line depicts the sun direction.
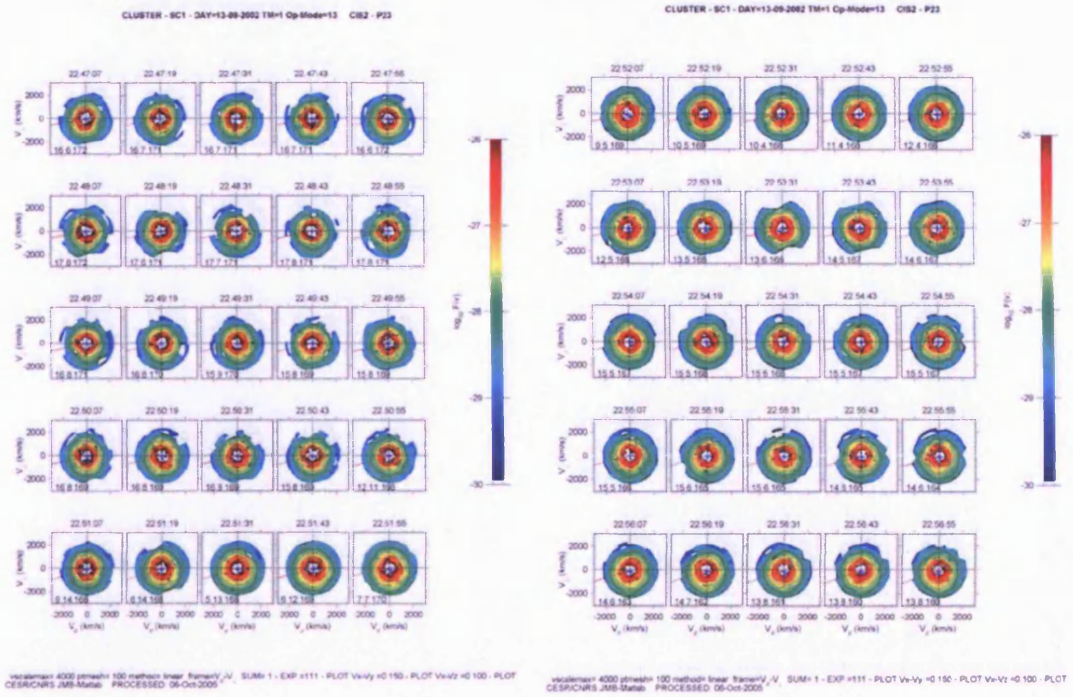
Figure 6.17: Cluster 1 CIS2 (HIA) distribution functions for 13 September 2002 for 2247 to 2256 UT, at 12 s intervals (read left to right and top to bottom across left page first, then right page). Each panel shows $V_\parallel$ against $V_\perp$; the red line depicts the sun direction.
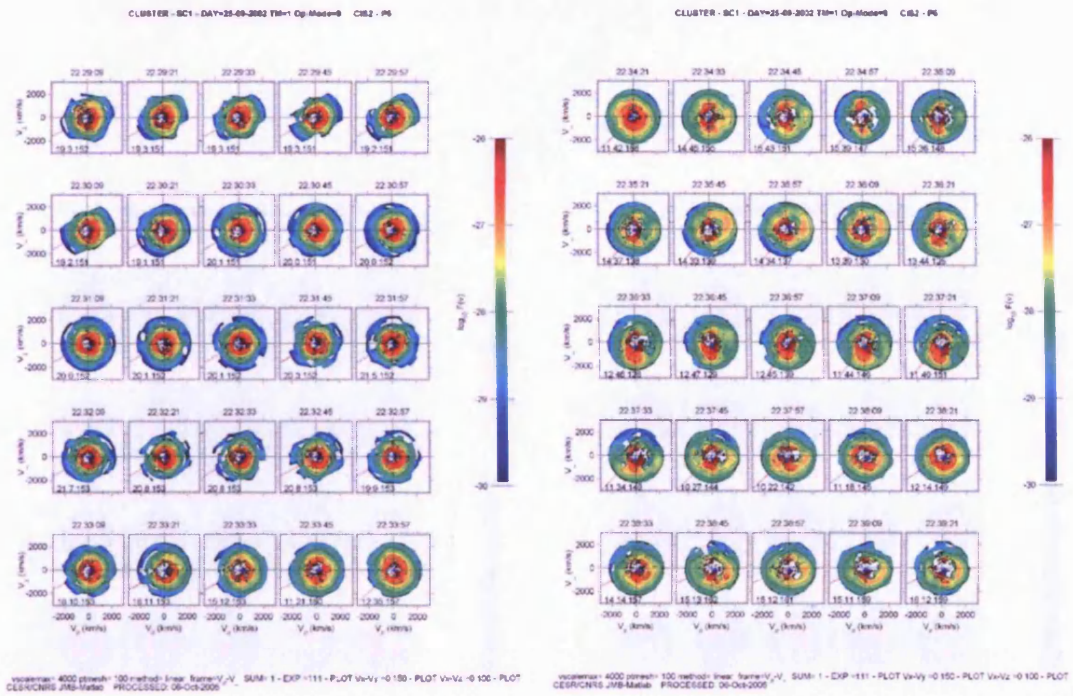
Figure 6.18: Cluster 1 CIS2 (HIA) distribution functions for 25 September 2002 for 2229 to 2239 UT, at 12 s intervals (read left to right and top to bottom across left page first, then right page). Each panel shows $V_\parallel$ against $V_\perp$; the red line depicts the sun direction.
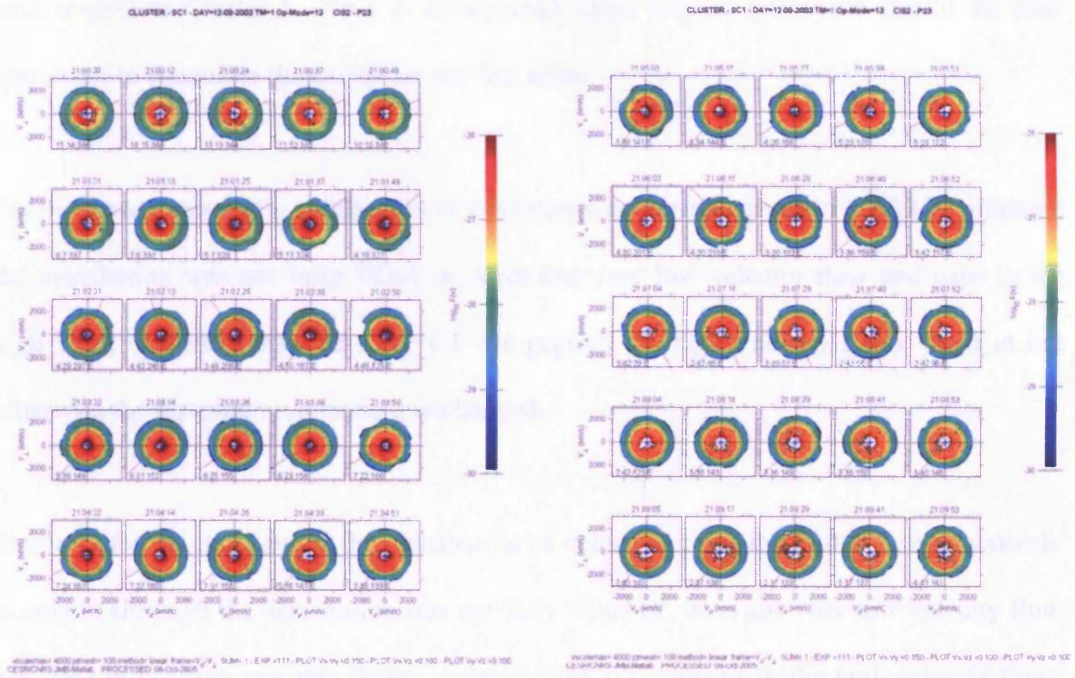
Figure 6.19: Cluster 1 CIS2 (HIA) distribution functions for 12 September 2003 for 2100 to 2109 UT, at 12 s intervals (read left to right and top to bottom across left page first, then right page). Each panel shows $V_\parallel$ against $V_\perp$; the red line depicts the sun direction.

flux was detected in the $-V_\parallel$ direction. From 1915 UT the spacecraft entered the central plasma sheet, detecting an isotropic distribution function. A similar series of distribution functions was detected by the Cluster 3 HIA instrument (data not shown), delayed by ~40 s with respect to Cluster 1. This is as expected, since Cluster 3 was the last of the four spacecraft to encounter the cavity for the first event.

For the second event, the distribution of velocities was isotropic prior to 2252 UT, although the distribution was not fully 'filled in', with few very low velocity flow and gaps in the high velocity flows. Around 2252 UT the gaps in the high velocity flows filled in but otherwise the distribution remained unchanged.

Similarly for the third event, the distribution of velocities prior to 2234 UT was relatively isotropic, although the distribution was not fully 'filled in', with few very low velocity flow and gaps in the high velocity flows. Around 2234 UT the gaps in the high velocity flows filled in and there was an increase in the lower velocity flow, resulting in a fully isotropic distribution function similar to that of the central plasma sheet. This quickly changed as first tailward then Earthward $V_\parallel$ was lost leaving plasma which had solely $V_\perp$ at ~ 2235 UT. The distribution then filled in at all pitch angles, with slightly enhanced flux in the positive $V_\parallel$ direction around 2236 UT.

For the fourth event, the distribution of velocities prior to 2105 UT was isotropic. This distribution was maintained around 2105 UT and still remained unchanged after 2105 UT.

6.3 Discussion of the magnetic cavity events

The four magnetic cavity events studied occurred at 1911 UT on 1st September 2002, 2252 UT on 13th September 2002, 2234 UT on 25th September 2002 and 2105 UT on 12th September 2003. The first cavity event occurred ~50 minutes after a substorm expansion phase onset. Prior to the second there was evidence of substorm activity in the ground magnetometer data ~5 hours before and an intensification ~20 minutes before the magnetic cavity. There was possible evidence for a small substorm or pseudobreakup ~ 1.5 hours before the third magnetic cavity, and ~1 hour before the fourth magnetic cavity. This suggests that the magnetic cavities may be associated with magnetospheric substorms and in particular the third phase, the recovery phase. However it is by no means conclusive evidence for this and the magnetic cavities may be a result of a process completely independent of substorms.

All four magnetic cavities were detected whilst the Cluster spacecraft were located in the region of ~18 R_E downtail. The first magnetic cavity was clearly embedded within the plasma sheet boundary layer, and associated with the plasma sheet boundary layer crossing. The other three cavity events were located in the plasma sheet. Despite the variation in y and z position of the spacecraft during these cavities (two in the northern lobe and two in the southern lobe), all of the cavities were travelling Earthwards, from dawn to dusk and down on to the spacecraft. This may simply be a co-incidence between the four events chosen; perhaps a result of slight changes in the magnetotail configuration resulting in the spacecraft being in the same effective location with respect to the plasma sheet; or perhaps it is a more fundamental feature of the magnetic cavities, in which case other events might be expected to follow the same pattern. However it does mean that the motion in the two

lobes is different.

The order-of-magnitude velocities of the cavities were calculated as 100 km s^{-1}, 70 km s^{-1}, 270 km s^{-1} and 60 km s^{-1}. These all agree to within a factor of ~4. Their scale sizes in the direction of propagation were calculated as 7000 km, 13000 km, 24000 km and 4000 km. These agree to within a factor of 6; here it is worth noting that the time taken for the cavity to pass over the spacecraft was rather more subjective than the time between magnetic minimum crossings, and so the cavity sizes are more prone to inaccuracy. For the second cavity event for example, the time taken for the cavity to pass over the spacecraft was taken as 180 s. However, inspection of the data shows that a precise 'recovery' was difficult to decide upon since it was so gradual, and so a time from ~150 s might have been chosen. This would have resulted in a cavity sale size of ~ 11000 km, a difference of ~15% of the stated value.

A large increase in the plasma beta was detected at the time of the magnetic cavities, probably due to the small value of magnetic field dominating the plasma beta calculation ($2\mu_0 nkT_\perp/B^2$) resulting in the large values of plasma beta. The velocity distribution functions ($V_\parallel$ against $V_\perp$) calculated from CIS data showed that for the first cavity event, the velocity distribution was mainly isotropic and filled in around the time of the magnetic cavity with hot, dense, isotropic, low velocity plasma; plasma characteristics similar to that of the central plasma sheet. The second cavity event also displayed an isotropic velocity distribution which filled in at the time of the magnetic cavity. One minute after the cavity the distribution became mainly $V_\perp$ then after another minute filled in at all pitch angles, with slightly enhanced flux in the positive $V_\parallel$ direction. The third cavity event showed an

isotropic velocity distribution function over the time of the magnetic cavity. The observations for the last three cavity events were quite different from those of the first cavity event in that their velocity distribution functions did not change as dramatically over the interval, and it is likely that this is because the first event was embedded in the plasma sheet boundary layer whereas these were all located in the plasma sheet.

One might try to explain the signatures detected during these cavity events as the central plasma sheet expanding and contracting over the spacecraft, particularly since the plasma characteristics of all four events were similar to that of the central plasma sheet. However, for all of the cavity events the FGM data from the four separate Cluster spacecraft indicate that the cavities could not have been a signature of the central plasma sheet since the signatures were not nested. Instead the signatures, which were detected in a very clear order for each event, imply a structure which encountered the spacecraft whilst travelling in one direction only (indeed, the same direction for each event). Also, the first cavity event was very clearly associated with the plasma sheet boundary layer and hence the spacecraft could not have been in the central plasma sheet.

These magnetic cavities are not the same phenomenon as the magnetic bubbles described by Sergeev et al. (1996), and Chen and Wolf, (1999). The magnetic bubbles, described in Section 2.5, are of reduced plasma pressure and density and have an increased magnetic field. This increase in B_z is the opposite signature to that of the magnetic cavities.

Current sheet flapping motion (e.g. Nakamura et al., 2002, Sergeev et al., 2003, Sitnov et al., 2004) may explain this phenomenon. This is when the current sheet exhibits vertically flapping oscillations which are generally rapid (~ 100 km s^{-1}), of large amplitude (~ 1 R_E)

and in the north-south direction. It is sometimes the case that the current sheet is tilted in the X-Y plane. Such motion may be configured in such a way as to produce the magnetic cavity signatures detected, and the variations in clock angle may indicate that this is a possibility. However, the fact that the cavity events studied were definitely not current sheet crossings would make this complicated.

6.4 Conclusions

Four magnetic cavities have been studied, three in 2002 and one in 2003. One was located in the plasma sheet boundary layer, the others in the plasma sheet. The signatures detected for each of the four events were similar, and the calculated velocities in the direction of propagation and scale size of the cavities were within reasonable agreement with each other. The direction in which the magnetic cavities were travelling were the same for each spacecraft and it would be interesting to see whether this is also the case for other potential magnetic cavity candidates, or simply a co-incidence. There is some evidence that the magnetic cavities may be associated with the recovery phase of magnetospheric substorms.

These magnetic cavities seem to be a different phenomenon from that of the magnetic bubbles described by Sergeev et al. (1996), and Chen and Wolf, (1999). It has also been determined that the magnetic cavities are not a result of the central plasma sheet flapping across the spacecraft, although the plasma in the cavities is similar to that of the central plasma sheet. Current sheet flapping motion (e.g. Nakamura et al., 2002, Sergeev et al., 2003, Sitnov et al., 2004) may be a possible explanation; although there would be difficulties with this given the lack of current sheet crossings detected during the magnetic

cavity encounters.

Further study of magnetic cavities is required to accurately determine their characteristics and origin. A more comprehensive search for magnetic cavity events would provide a larger number of events to study in order to undertake a more complete statistical survey of these events and provide strong candidates to investigate in greater detail. This would add to the work presented here in order to gain a fuller understanding of magnetic cavities.

Chapter 7

Conclusions

Two intervals were studied in an attempt to determine the substorm onset mechanism for the substorms which occurred during those intervals. These were presented in Chapter 4 and Chapter 5. The first substorm study found an interesting new feature which prompted further study and a search for further candidates. The work on these four events was presented in Chapter 6. In this chapter the conclusions from the work in this thesis are drawn together and there is also a discussion of the ways in which this work could be extended in the future.

7.1 Conclusions drawn from the work presented in this thesis

The first substorm study interval presented in Chapter 4 provided a wealth of information about the two substorms which occurred during the interval. It was not possible to determine which substorm model was the most appropriate for the first substorm event since spacecraft were not ideally placed for tail observations of the substorm signatures, and hence the timings required were not obtained. It was nevertheless possible to demonstrate that the Cluster spacecraft are capable of remotely observing a substorm even when located in a tail lobe, far from the plasma sheet.

For the second substorm which occurred during the first interval presented, the Cluster

spacecraft were in an ideal location to compare timings of signatures in the magnetosphere, at geosynchronous orbit and in the ionosphere. Since dipolarization was observed by Cluster at the same time as a plasma injection was detected by the Polar spacecraft it was concluded that the NENL model (Baker et al., 1996, and references therein) was the most appropriate for this substorm; information could not have propagated from the inner current sheet, to the NENL and back again, in this time.

This interval also included an interesting new feature: a signature in the Cluster magnetic field data which showed a region of zero magnetic field. This is termed a magnetic cavity. This cavity was detected in the recovery phase of a substorm, within ~ 50 minutes of substorm expansion phase onset. The cavity was detected within the plasma sheet boundary layer during a crossing of the spacecraft from the northern lobe into the plasma sheet, and is clearly associated with the plasma sheet boundary layer in this case. The cavity was detected travelling at ~100 km s^{-1}, moving Earthwards, from dawn to dusk and equatorward over the spacecraft. Its scale size was of the order of 7000 km and had characteristics similar to that of the central plasma sheet: it was filled with hot, dense, isotropic, low velocity plasma. However, since the cavity was clearly associated with the plasma sheet boundary layer, this phenomenon could not be explained by the expansion and contraction of the central plasma sheet over the spacecraft.

The second substorm study interval, presented in Chapter 5, brought together a great number of data sets which provided a good overview of the substorm event. It was not possible to ascertain the substorm onset mechanism responsible for this substorm since the signatures were detected at very widely spaced locations, and in particular they were not always from the same local time sector which made direct comparisons of, for example, the

near-Earth LANL signatures and the Cluster signatures impossible. The timings were all within just one minute of each other which was not sufficient to say whether one substorm mechanism was more likely than any other. Nevertheless many other findings were presented. It is worth noting that there is a similarity between the configuration of the Cluster, LANL, GOES and Polar spacecraft to that of the new THEMIS (Time History of Events and Macroscale Interactions during Substorms) mission, and hence some difficulties may be expected in deciding between substorm onset models from THEMIS data.

The rapid thinning of the plasma sheet under the spacecraft prior to onset was detected during the growth phase of the substorm. A current density in the y direction of $\sim$0.8x10^{-9} A m^{-2} was detected before onset, which is around half the typical total current density expected (which was calculated as $\sim$ 2x10^{-9} A m^{-2}). This current was lost a few minutes before substorm expansion phase onset, although the magnetic field magnitude did not show a corresponding decrease. This indicates that the current sheet thinned under the spacecraft a few minutes before onset, since the total current remained the same.

It was determined that the Cluster spacecraft detected the development of a TCR (e.g. Slavin et al., 2005), formed by the formation of a plasmoid under the spacecraft. The spacecraft were located tailward of the near-Earth neutral line initially, indicating that it formed within 15 R_E of Earth, closer than the 20 to 30 R_E downtail suggested by Nagai et al. (1998). The TCR then moved downtail, taking the NENL with it across the spacecraft. The TCR's velocity was calculated to be $\sim$ 200 km s^{-1}, around one quarter of the values quoted in Slavin et al. (2005). However the TCR was in the first stages of formation when the Cluster spacecraft detected it, similar to midtail TCRs described in Taguchi et al. (1998), and this may account for its low velocity.

The Cluster spacecraft also detected currents during this substorm interval that were predominantly Earthward-directed as the spacecraft exited the plasma sheet and predominantly tailward directed later, as the spacecraft re-entered the plasma sheet. These currents were associated mainly with B_y varying in the z direction, rather than B_z varying in the y direction, and were therefore attributed to the Region 1 current system (Iijima and Potemra, 1978) rather than the substorm current wedge (McPherron et al., 1973). The Region 1 current system was initially skewed to the pre-midnight sector for this substorm, consistent with the substorm onset being located in the pre-midnight sector of the magnetotail (see e.g. Nagai et al., 1998); later the Region 1 current system returned to a more central location around the midnight sector.

Following on from the work in Chapter 4 a search for other potential magnetic cavity candidates was undertaken and three of these were chosen for further study, two in 2002 and one in 2003, together with the original cavity event. This study was presented in Chapter 6. Studying the magnetic cavities with data from two different years was useful since the separation of the Cluster spacecraft was ~4000 km in 2002 but only ~500 km in 2003, allowing comparison between the different scale sizes. The cavity events were all located at ~ 18 R_E downtail. The first was clearly embedded in the plasma sheet boundary layer, detecting plasma sheet boundary layer beams before and after the cavity passed and hot, dense, isotropic, low velocity plasma within the magnetic cavity. The other three were located in the plasma sheet and hence the CIS distribution functions did not provide as clear a picture of the changes in plasma as the magnetic cavities passed over the spacecraft as for the first event. However there was still some evidence for the 'filling in' of the velocity distributions around the time of the magnetic cavities, resulting in more fully isotropic

velocity distribution functions. One candidate also showed evidence for the distribution becoming mainly $V_\perp$ one minute after the magnetic cavity then returning once again to its isotropic distribution.

All four magnetic cavity events occurred up to ~ 1.5 hour after some form of substorm activity which prompts the question of whether these magnetic field cavities are in some way related to the magnetospheric substorm, whether an (as yet undetected) integral part of the substorm phenomenon, or arising as a consequence of it. The cavities were travelling at velocities ranging from ~ 60 km s^{-1} to ~ 270 km s^{-1}, and their scale size ranged from ~ 4000 km to ~ 24000km. It is not yet known whether the magnetic cavities change their shape over time, and hence whether these scale sizes are representative of these features. It is worth noting that 24000 km is approximately 3.75 R_E, which is of the same order as the thickness of the plasma sheet in the region where the magnetic cavity candidates were located.

It was determined that the magnetic cavities could not have been a result of the expansion and contraction of the central plasma sheet over the spacecraft, nor are they the same as the magnetic plasma bubbles described by Sergeev et al. (1996), and Chen and Wolf, (1999). It may be that current sheet flapping motion (e.g. Nakamura et al., 2002, Sergeev et al., 2003, Sitnov et al., 2004) will be used to interpret the magnetic cavities, although such an explanation would be complicated.

In conclusion, it has been demonstrated that it is not straightforward to determine the onset mechanism for a magnetospheric substorm despite having a widely distributed network of spacecraft and ground stations. Of the three substorms investigated it was possible to

determine the onset mechanism for only one, for which the near-Earth neutral line model was the most likely. The magnetic cavity feature investigated was not a singular event; three potential candidates have also been investigated which appear to show similar signatures to the first event. There is some variation between the four events, which is not unexpected; however, the variation is not so great as to cause concern regarding the validity of the potential candidates, and there is a strong case for further work to be undertaken to increase the understanding of these magnetic cavities.

7.2 Future work

The interesting new magnetic cavity is a feature which has not been noticed before, and which clearly needs further work. An extension to the brief statistical survey of other possible events described here is certainly required and a closer study of strong candidates would be extremely useful for determining the characteristics of these events. A theory explaining the observations has not yet been forthcoming, and the development of such a theory may be useful in identifying more of these events. It may also help in determining how they fit in with the currently accepted model of the magnetosphere and its phenomena, and whether they are associated with magnetospheric substorms. If they are not then other magnetospheric phenomena such as current sheet flapping motion need to be considered, as well as the possibility that the magnetic cavities are a result of something entirely separate from the magnetosphere.

It is hoped that the controversy concerning substorm onset models can be resolved in the future by further investigation of individual events and by performing statistical surveys of

signature timings. New instruments are being developed which may help in the determination of timings and location of signatures, including the development of new HF radars for the SuperDARN array, the new Space Plasma Exploration with Active Radar (SPEAR) instrument which has been deployed within the last few years, the Double Star spacecraft which have been launched recently and, most interestingly for substorm research, the Time History of Events and Macroscale Interactions during Substorms (THEMIS) mission which is scheduled for launch soon.

New HF radars for the SuperDARN array will provide greater coverage of the polar caps and hence increase the likelihood of line-of-sight data being available, allowing ionospheric conditions to be studied for a greater number of substorm events. An increased data set will also help to constrain the global map potential model, increasing the accuracy of the ionospheric flow pattern which can be calculated. The new SPEAR instrument is intended to have several functions, and two of these in particular may be useful in substorm research: field line tagging and all-sky radar mode. The field line tagging mode uses artificial waves to tag magnetic field lines, which can be identified by spacecraft to provide a more accurate link between the spacecraft data and ground-based data. The all-sky radar mode would provide ionospheric data similar to that of the SuperDARN radars, but over a 360 ° field of view, again increasing data coverage in this region.

The Double Star spacecraft were launched in December 2003 and July 2004. One is a polar orbiting satellite and the other an equatorial satellite; their orbits are designed to complement that of the Cluster spacecraft in order to perform multi-satellite studies of the various regions of interest within the Earth's magnetosphere. THEMIS consists of five spacecraft which are to be located in the magnetotail at different distances from Earth.

Three spacecraft will be located at ~10 R_E, one at 20 R_E and another at 30 R_E. Each will monitor the magnetic field, electric field and plasma properties at its location with time resolution of up to 10 s. This is intended to sample the magnetosphere in the current disruption region and in the Earthward and tailward regions around the near-Earth reconnection x-line. It is hoped that this will allow accurate timing of the substorm signatures, particularly when studied alongside the Cluster, Double Star and other data sets.

Bibliography

Akasofu, S.-I.: The development of the auroral substorm, *Planet. Space Sci.*, 12, 273 - 282, 1964

Baker, D.N., T.I. Pulkkinen, V. Angelopoulos, W. Baumjohann and R.L. McPherron, Neutral line model of substorms: Past results and present view *J. Geophys. Res.*, 101, 12975 - 13010, 1996

Baker, D. N., W.K. Peterson, S. Eriksson, X. Li, J.B. Blake, J.L. Burch, P.W. Daly, M.W. Dunlop, A. Korth, E. Donovan, R. Friedel, T.A. Fritz, H.U. Frey, S.B. Mende, J. Roeder, H.J. Singer, Timing of magnetic reconnection initiation during a global magnetospheric substorm onset, *Geophys. Res. Lett.*, 29, 2190 - 2193, 2002

Balogh, A., Dunlop, M.W., Cowley, S.W.H., Southwood, D.J., Thomlinson, J.G., Glassmeier, K.-H., Musmann, G., Lühr, H., Buchert, S., Acuña, M.H., Fairfield, D.H., Slavin, J.A., Riedler, W., Shwingenschuh, K., Kivelson, M.G., The Cluster magnetic fields investigation *Space Sci. Rev.*, 79, 65 - 91, 1997

Baumjohann, W., M. Hesse, S. Kokubun, T. Mukai, T. Nagai, A. A. Petrukovich, Substorm dipolarization and recovery, *J. Geophys. Res.*, 104, 24995 - 25000, 1999

Baumjohann, W., G. Paschmann, and H. Lühr, Characteristics of high-speed ion flows

in the plasma sheet, *J. Geophys. Res.*, 95, 3801 – 3809, 1990

Baumjohann, W., Paschmann, G., Sckopke, N., Cattell, C.A., Carlson, C.W., Average ion moments in the plasma sheet boundary layer, *J. Geophys. Res.*, 93, 11507 - 11520, 1988

Belian R.D., Baker, D.N., Higbie, P.R., and Hones, E.W., High-resolution energetic particle measurements at 6.6 R_E: 2 high-energy proton drift echoes, *J. Geophys. Res.*, 83, 4857 - 4862, 1978

Belian, R.D., Gisler, G.R., Cayton, T., and Christensen, R., High-Z Energetic Particles at Geostationary Orbit During the Great Solar Proton Event Series of October 1989, *J. Geophys. Res.*, 97, 16897 - 16906, 1992

Birn, J. and Hesse, M., Details of current disruption and diversion in simulations of magnetotail dynamics, *J. Geophys. Res.*, 101, 15345 - 15358, 1996

Birn, J., F. Thomsen, J. E. Borovsky, G. D. Reeves, D. J. McComas, and R. D. Belian, Characteristic plasma properties during dispersionless substorm injections at geosynchronous orbit, *J. Geophys. Res.*, 102, 2309 - 2324, 1997

Blake, J.B., J. F. Fennell, L. M. Friesen, B. M. Johnson, W. A. Kolasinski, D. J. Mabry, J. V. Osborn, S. H. Penzin, E. R. Schnauss, H. E. Spence, D. N. Baker, R. Belian, T. A. Fritz, W. Ford, B. Laubscher, R. Stiglich, R. A. Baraze, M. F. Hilsenrath, W. L. Imhof, J. R. Kilner, J. Mobilia, H. D. Voss, A. Korth, M. Gull, K. Fischer, M. Grande, and D. Hall, CEPPAD: Comprehensive Energetic Particle and Pitch Angle Distribution Experiment on POLAR *Space Sci. Rev.*, 71, 531 - 562, 1995

Chen, C.X. and Wolf, R.A., Interpretation of high-speed flows in the plasma sheet, *J. Geophys. Res.*, 98, 21409 - 21419, 1993

Chen, C.X. and Wolf, R.A., Theory of thin-filament motion in Earth's magnetotail and its application to bursty bulk flows, *J. Geophys. Res.*, 104, 14613 - 14626, 1999

Cowley, S.W.H., A Beginner's Guide to the Earth's Magnetosphere, *Earth in Space*, Vol. 8, No. 7, March 1996

Cowley, S.W.H., Magnetosphere-ionosphere interactions – a tutorial review, *in Magnetospheric Current Systems, edited by S. Ohtani, R. Fujii, M. Hesse, and R.L. Lysak, Geophys. Monograph 118, AGU Publ., Washington, USA*, pp. 91 - 106, 2000

Cowley, S.W.H. and Lockwood, M. Excitation and decay of solar wind-driven flows in the magnetosphere-ionosphere system, *Ann. Geophys.*, 10, 103 - 115, 1992

Dewhurst, J.P., Owen, C.J., Fazakerley, A.N., Balogh, A. Thinning and Expansion of the Substorm Plasma Sheet: Cluster PEACE Timing Analysis, *Ann. Geophys.*, 22, 4165 - 4184, 2004

Draper, N.C., Lester, M., Wild, J.A., Milan, S.E., Provan, G., Grocott, A., Cowley, S.W.H., Bogdanova, Y., Dewhurst, J.P., Fazakerley, A.N., Davies, J.A., Bosqued, J.M., A joint Cluster and ground-based instruments study of two magnetospheric substorm events on 1st September 2002 *Ann. Geophys.*, 22, 4217 - 4228, 2004

Dungey, J. W., Interplanetary magnetic field and the auroral zones, *Phys. Rev. Lett.*, 6, 47 - 48, 1961

Eastman, T.E., L. A. Frank, W. K. Peterson, and W. Lennartsson, The plasma sheet boundary layer, *J. Geophys. Res.*, 89, 1553 - 1572, 1984

Escoubet, C.P., Russel, C.T., and Schmidt, R. The Cluster and Phoenix Missions. *Space Sci. Rev.*, 79, 1997

Fairfield, D. H., and N. F. Ness, Configuration of the geomagnetic tail during substorms, *J. Geophys. Res.*, 75, 7032 - 7047, 1970

Frank, L. A., J. B. Sigwarth and W. R. Paterson, High-Resolution Global Images of Earth's Auroras During Substorms, in *Substorms-4, International Conference on Substorms-4, Lake Hamana, Japan, March 9-13, 1998, eds. S. Kokubun and Y. Kamide*, pp. 3-8, Terra Scientific Publishing Company, Tokyo, Japan, 1998

Friis-Christensen, E., Kamide, Y., Richmond, A.D. and Matsushita, S., Interplanetary magnetic field control of high-latitude electric fields and currents determined from Greenland magnetometer data, *J. Geophys. Res.*, 90, 1325 - 1338, 1985

Greenwald, R.A., K.B. Baker, J.R. Dudeny, M. Pinnock, T.B. Jones, E.C. Thomas, J.-P. Villain, J.-C. Cerisier, C. Senior, C. Hanuise, R.D. Hunsucker, G. Sofko, J. Koehler, E. Nielsen, R. Pellinen, A.D.M. Walker, N. Sato, H. Yamagishi Darn/SuperDARN: a global view of the dynamics of high-latitude convection *Space Sci. Rev.*, 71, 761 - 796, 1995

Grocott, A., T.K. Yeoman, R. Nakamura, S.W.H. Cowley, H. Rème, and B. Klecker, Multi-instrument observations of the ionospheric counterpart to a bursty bulk flow in the near-Earth plasma sheet, *Ann. Geophys*, 22, 1061 - 1075, 2004

Hones, E.W., Jr., Plasma flow in the magnetotail and its implications for substorm theories, *in Dynamics of the Magnetosphere, S.I. Akasofu, ed.,* p. 545, D. Reidel Publ. Co., 1979

Hones, E. W., Jr., Baker, D.N., Bame, S.J., Feldman, W.C., Gosling, J.T., McComas, D.J., Zwickl, R.D. Slavin, J.A., Smith, E.J. and Tsurutani, B.T., Structure of the magnetotail at 220 Re, *Geophys. Res. Lett.,* 11, 5 - 7, 1984

Ieda, A., S. Machida, T. Mukai, Y. Saito, T. Yamamoto, A. Nishida, T. Terasawa, S. Kokubun, Statistical analysis of the plasmoid evolution with Geotail observations, *J. Geophys. Res.,* 103, 4453 - 4465, 1998

Iijima, T., and T.A. Potemra, Large-scale characteristics of field-aligned currents associated with substorms, *J. Geophys. Res.,* 83, 599 - 615, 1978

Johnstone, A.D., C. Alsop, S. Burge, P.J. Carter, A.J. Coates, A.J. Coker, A.N. Fazakerley, M. Grande, R.A. Gowen, C. Gurgiolo, B.K. Hancock, B. Narheim, A. Preece, P.H. Sheather, J.D. Winningham, R.D. Woodliffe Peace: A Plasma Electron and Current Experiment *Space Sci. Rev.* 79, 351 - 398, 1997

Kan, J.R., A global magnetosphere-ionosphere coupling model of substorms, *J. Geophys. Res.,* 98, 17263 - 17275, 1993

Khan, H., and Cowley, S.W.H. Observations of the response time of high-latitude ionospheric convection to variations in the interplanetary magnetic field using EISCAT and IMP-8 data *Ann. Geophys.*, 17, 1306 - 1335, 1999

Kivelson, M.G. and Russell, C.T. (Editors) *Introduction to Space Physics*, Cambridge University Press, 1995

Lester, M., W. J. Hughes, and H. J. Singer Polarization patterns of Pi 2 magnetic pulsations and the substorm current wedge *J. Geophys. Res.*, 88, 7958 - 7966, 1983

Lui, A.T.Y.: Current disruption in the Earth's magnetosphere: Observations and models *J. Geophys. Res.*, 101, 13067 - 13088, 1996

Lyons, L.R. A new theory for magnetospheric substorms, *J. Geophys. Res.*, 100, 19069 - 19081, 1995

Lyons, L.R., T. Nagai, G. T. Blanchard, J. C. Samson, T. Yamamoto, T. Mukai, A. Nishida, S. Kokubun, Association between geotail plasma flows and auroral poleward boundary intensifications observed by CANOPUS photometers, *J. Geophys. Res.*, 104, 4485 - 4500, 1999

McComas, D.J., S.J. Bame, P. Barker, W.C. Feldman, J.L. Phillips, P. Riley and J.W. Griffee Solar wind electron proton alpha monitor (SWEPAM) for the Advanced Composition Explorer *Space Sci. Rev.*, 86, 563 - 612, 1998

McPherron, R.L.: Growth phase of magnetospheric substorms, *J. Geophys. Res.*, 75, 5592 - 5599, 1970

McPherron, R.L., C.T. Russell, M.P. Aubry Satellite studies of magnetospheric substorms on August 15, 1968, 9, Phenomenological model for substorms *J. Geophys. Res.*, 78, 3131-3149, 1973

Miyashita, Y., S. Machida, S.T. Mukai, Y. Saito, K. Tsuruda, H. Hayakawa and P.R. Sutcliffe, A statistical study of variations in the near and middistant magnetotail associated with substorm onsets: GEOTAIL observations, *J. Geophys. Res.*, 106, 6259-6274, 2001

Nagai, T., Observed magnetic substorm signatures at synchronous altitude, *J. Geophys. Res.*, 87, 4405 - 4417, 1982

Nagai, T., T. Mukai, T. Yamamoto, A. Nishida, S. Kokubun, and R. P. Lepping, Plasma sheet pressure changes during the substorm growth phase, *Geophys. Res. Lett.*, 24, 963 - 966, 1997

Nagai, T., Fujimoto, M., Saito, Y., Machida, S., Terasawa, T., Nakamura, R., Yamamoto, T., Mukai, T., Nishida, A., Kokubun, S., Structure and dynamics of magnetic reconnection for substorm onsets with Geotail observations, *J. Geophys. Res.*, 103, 4419 - 4440, 1998

Nakamura, R., W. Baumjohann, A. Runov, M. Volwerk, T.L. Zhang, B. Klecker, Y. Bogdanova, A. Roux, A. Balogh, H. Rème, J.A. Sauvaud, H.U. Frey: Fast Flow during current sheet thinning. *Geophys. Res. Lett.*, 29, 2140, 2002

Nakamura, R., Amm, O., Laakso, H., Draper, N., Lester, M., Grocott, A., Klecker, B., Balogh, A., Rème, H., and André, M., Localized fast flow disturbance observed in the plasma sheet and in the ionosphere, *Ann. Geophys*, 23, 553 - 566, 2005

Pontius, D.H., Jr. and Wolf, R.A., Transient flux tubes in the terrestrial magnetosphere, *Geophys. Res. Lett.*, 17, 49 - 52, 1990

Rème, H., J.M. Bosqued, J.A. Sauvaud, A. Cros, J. Dandouras, C. Aoustin, J. Bouyssou, Th. Camus, J. Cuvilo, C. Martz, J.L. Médale, H. Perrier, D. Romefort, J. Rouzaud, D. d'Uston, E. Möbius, K. Crocker, M. Granoff, L.M. Kistler, M. Popecki, D. Hovestadt, B. Klecker, G. Paschmann, M. Scholer, C.W. Carlson, D.W. Curtis, R.P. Lin, J.P. McFadden, V. Formisano, E. Amata, M.B. Bavassano- Cattaneo, P. Baldetti, G. Belluci, R. Bruno, G. Chionchio, A. di Lellis, E.G. Shelley, A.G. Ghielmetti, W. Lennartsson, A. Korth, U. Rosenbauer, R. Lundin, S. Olsen, G.K. Parks, M. McCarthy and H. Balsiger The Cluster Ion Spectrometry (CIS) Experiment *Space Sci. Rev.* 79, 303 - 350, 1997

Riedler, W., Torkar, K., Rudenauer, F., Fehringer, M., Pedersen, A., Schmidt, R., Grard, R. J. L., Arends, H., Narheim, B. T., Troim, J., Torbert, R., Olsen, R. C., Whipple, E., Goldstein, R., Vala-vanoglou, N., and Zhao, H., Active Spacecraft Potential Control. *In Escoubet et al., 1997*, pp. 271 - 302, 1997

Rostoker, G., Akasofu, S.-I., Foster, J., Greenwald, R.A., Lui, A.T.Y., Kamide, Y., Kawasaki, K., McPherron, R.L., Russell, C.T., Magnetospheric substorms - Definition

and signatures, *J. Geophys. Res.*, 85, 1663 - 1668, 1980

Rostoker, G., Samson, J., Creutzberg, F., Hughes, T., McDiarmid, D., McNamara, A., Jones, A.V., Wallis, D., and Cogger, L., CANOPUS-A ground based instrument array for remote sensing the high latitude ionosphere during the ISTP/CGS program, *Space Sci. Rev.*, 71, 734 - 760, 1995

Ruohoniemi, J.M., and K. B. Baker, Large-scale imaging of high-latitude convection with Super Dual Auroral Radar Network HF radar observations, *J. Geophys. Res.*, 103, 20797 - 20811, 1998

Saito, T., Geomagnetic pulsations, *Space Sci. Rev.*, 10, 319 - 412, 1969

Sandholt, P.E., C.J. Farrugia, M. Lester, S. Cowley, S. Milan, W.F. Denig, B. Lybekk, E. Trondsen and V. Vorobjev, Multistage substorm expansion: Auroral dynamics in relation to plasma sheet particle injection, precipitation, and plasma convection, *J. Geophys. Res.*,107, 1342, 2002

Sergeev, V.A., Angelopoulos, V., Gosling, J.T., Cattell, C.A., Russell, C.T., Detection of localized, plasma-depleted flux tubes or bubbles in the midtail plasma sheet, *J. Geophys. Res.*, 101, 10817 - 10826, 1996

Sergeev, V., Runov, A., Baumjohann, W., Nakamura, R., Zhang, T.L., Volwerk, M., Balogh, A., Rème, H, Sauvaud, J.A., André, M., Klecker, B., Current sheet flapping motion and structure observed by Cluster, *Geophys. Res. Lett.*, 30, 1327, 2003

Shiokawa, K., W. Baumjohann, G. Haerendel, G Paschmann, J.F. Fennel, E. Friis-Christensen, H. Luhr, G.D. Reeves, C.T. Russell, P.R. Sutcliffe and K Takahashi, High-speed ion flow, substorm current wedge, and multiple Pi 2 pulsations, *J. Geophys. Res.*, 103 (A3), 4491 - 4507, 1998

Sitnov, M. I., M. Swisdak, J. F. Drake, and P.N. Guzdar, A model of the bifurcated current sheet: 2. Flapping motions, *Geophys. Res. Lett.*, 31, L09805, 2004

Slavin, J.A., D.H. Fairfield, R.P. Lepping, A. Szabo, M.J. Reiner, M. Kaiser, C.J. Owen, T. Phan, R. Lin, S. Kokubun, T. Mukai, T. Yamamoto, H. Singer, S. Romanov, J. Buechner, T. Iyemori, and G. Rostoker., WIND, GEOTAIL, and GOES 9 observations of magnetic field dipolarization and bursty bulk flows in the near-tail, *Geophys. Res. Lett.*, 24, 971 - 974, 1997

Slavin J. A., R. P. Lepping, J. Gjerloev, D. H. Fairfield, M. Hesse, C. J. Owen, M. B. Moldwin, T. Nagai, A. Ieda, and T. Mukai, Geotail observations of magnetic flux ropes in the plasma sheet, *J. Geophys. Res.*, 108, 1015 - 1032, 2003

Slavin J. A., E. I. Tanskanen, M. Hesse, C. J. Owen, M. W. Dunlop, S. Imber, E. A. Lucek, A. Balogh, K.-H. Glassmeier, Cluster observations of traveling compression regions in the near-tail, *J. Geophys. Res.*, 110, A06207, 2005

Smith, C.W., M.H. Acuña, M.F. Burlaga, J. L'Heureux, N.F. Ness, J. Scheifele The ACE Magnetic Fields Experiment *Space Sci. Rev.*, 86, 613 - 632, 1998

Stone, E.C., A.M. Frandsen, R.A. Mewaldt, E.R. Christian, D. Margolies, J.F. Ormes,

F. Snow The Advanced Composition Explorer *Space Sci. Rev.*, 86, 1 - 22, 1998

Taguchi, S., J. A. Slavin, M. Kiyohara, M. Nose, G. D. Reeves, and R. P. Lepping, Temporal relationship between midtail traveling compression regions and substorm onset: Evidence for near-Earth neutral line formation in the late growth phase, *J. Geophys. Res.*, *103*, 26607 - 26612, 1998

Tsyganenko, N. A., and D. P. Stern, Modeling the global magnetic field of the large-scale Birkeland current systems, *J. Geophys. Res.*, 101, 27187 - 27198, 1996

Viljanen, A., and Häkkinen, L.: IMAGE magnetometer network. *In: Satellite-Ground Based Coordination Sourcebook (eds. M. Lockwood, M.N. Wild and H.J. Opgenoorth)* ESA publications SP-1198, 111 - 117, 1997

Wilken, B., W.I. Axford, 1. Daglis, P. Daly, W. Güttler, W.H. Ip, A. Korth, G. Kremser, S. Livi, V.M. Vasyliunas, J. Woch, D. Baker, R.D. Belian, J.B. Blake, J.F. Fennell, L.R. Lyons, H. Borg, T.A. Fritz, F. Gliem, R. Rathje, M. Grande, D. Hall, K. Kecsueméty, S. McKenna-Lawlor, K. Mursula, P. Tanskanen, Z. Pu, I. Sandahl, E.T. Sarris, M. Scholer, M. Schulz, F. Sørass and S. Ullaland RAPID. The Imaging Energetic Particle Spectrometer on Cluster *Space Sci. Rev.* 79, 399 - 473, 1997

Yeoman, T.K. and H. Lühr, CUTLASS/IMAGE observations of high-latitude convection features during substorms, *Ann. Geophys.*, 15, 692 - 702, 1997

Yumoto, K., and the 210° MM Magnetic Observation Group: The STEP 210° magnetic meridian network project, *J. Geomag. Geoelectr.*, 48, 1297 - 1309, 1996

104